

University of Calabria

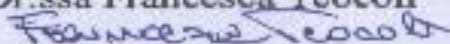
Faculty of Science

Chemistry Department - Physics Department

PhD Thesis

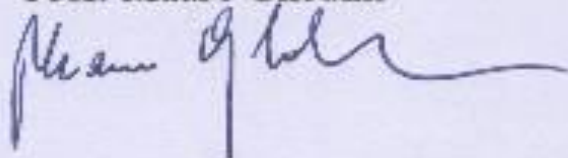
Synthesis and characterization of new hybrid organic/inorganic materials for electro-optic applications

Dr.ssa Francesca Teocoli



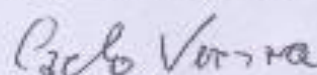
Supervisor

Prof. Mauro Ghedini



PhD Coordinator

Prof. Carlo Versace



Doctorate in

Science and Technologies of Mesophases and Molecular Materials

(XXIII PhD course)

FIS/01, CHIM/03



PhD Thesis

**Synthesis and characterization of new
hybrid organic/inorganic materials for
electro-optic applications**

Dr.ssa Francesca Teocoli

Supervisor

Prof. Mauro Ghedini

PhD Coordinator

Prof. Carlo Versace

Doctorate in

Science and Technologies of Mesophases and Molecular Materials



(XXIII PhD course)

FIS/01, CHIM/03

*Courage is the price that life exacts for granting peace.
The soul that knows it not,
know no release from little things;
knows not the livid loneliness of fear,
nor mountain heights where bitter joy can hear the sound of wings*

Amelia Earhart, *Courage* (1927)

**Synthesis and characterization of new hybrid
organic/inorganic materials for electro-optic applications**

A Thesis

Submitted to the Faculty of Science

of

University of Calabria

by

Dr.ssa Francesca Teocoli

in partial fulfillment of the

requirements for the degree

of

Doctor of Philosophy

December 2010

Contents

<i>Preface</i>	7
Chapter 1.	8
1.1 Hybrid Materials	8
1.2 Optoelectronic devices	12
1.2.1 Dye-sensitized solar cells	14
1.2.2 Light-emitting devices	18
Chapter 2. Luminescent mesostructured materials	21
2.1 Materials	24
2.1.1 Mesoporous powder and film	24
2.1.2 Ionic transition-metal complexes	26
2.2 Materials preparation	31
2.2.1 Co-condensation	33
2.2.2 EISA (Evaporation Induced Self-Assembling)	35
2.2.2.1 Dip-coating	38
2.3 Mesoporous characterization	40
2.3.1 Photoluminescence properties	43
2.3.1.1 Emission spectra, phosphorescence quantum yield and time-resolved luminescence	44
2.3.2 Powder X-ray diffraction (XRD)	48
2.3.3 N ₂ sorption	50
2.3.4 Scanning electron microscopy (SEM)	52
2.3.5 Transmission electron microscopy (TEM)	54

2.3.6 Thermogravimetric analysis (TGA)	55
Chapter 3. Solid state dye-sensitized solar cells	56
3.1 Materials	58
3.1.1 The substrate	58
3.1.2 The dye	59
3.1.2.1 Z907	63
3.1.2.2 New organic dyes	63
3.1.3 The hole-transport materials	64
3.1.4 The counter electrode	67
3.2 Device preparation	68
3.2.1 TiO ₂ layer	68
3.2.2 Sensitizer soaking	71
3.2.3 Hole-transport material deposition	71
3.2.4 Counter electrode deposition and the device sealing	72
3.3 Photovoltaic characterization	74
3.3.1 Definitions	74
3.3.2 Experimental Data	78
Chapter 4. Lighting devices – (LEEC)	82
4.1 Device Architecture	83
4.2 OLEDs vs. LEECs	85
4.3 Materials	90
4.3.1 Active layer	91
Chapter 5.	94
5.1 Luminescent mesostructured material: results	94

5.1.1 Paper	94
5.1.2 Communications	102
5.2 Solid state dye-sensitized solar cells: results	104
5.2.1 Paper	104
5.2.2 Communications	113
Chapter 6. Conclusion and Perspectives	114
Acknowledgments	118
References	119

Preface

The miscellaneous nature of materials science is becoming increasingly prominent, particularly in rapidly growing areas such as nanotechnology. Some of the key words characteristics of this study are Electro- and Photo- chemistry, which play an important role in a vast number of fundamental research and applied sphere of nanotechnology.

Electrochemistry includes, but is not limited to, the exploration of new inorganic and organic compounds, biochemical and biological systems, corrosion, energy applications involving fuel cells and solar cells, and nanoscale investigations.¹

Photochemistry pertains to electronically excited molecules which induce reactions.

Therefore photochemistry finds a significant place in varied applications of science and technology. The photophysical phenomena of fluorescence and phosphorescence have found varied functions, for example in light-emitting electrochemical cells (LEEC), photofunctional compounds², laser technology, and so on.

A further impetus to the study of photochemical reaction has been provided by the energy crisis. This has initiated researches into the conversion and storage of solar energy, processes which plants carry out so efficiently. The fundamental study of excited states of has led to the proper understanding of chemical reactions, modes of energy transfer and the intricate structure of matter.³

At the end, photo-electrochemistry combines photochemical and electrochemical methods for the study of the oxidation-reduction chemistry of the ground or excited states of molecules or ions. In general, it is the chemistry resulting from the interaction of light with electrochemical systems.

Chapter 1

1.1 Hybrid Materials

Since many years, the concept that a mixture of materials can show superior properties compared to their pure counterparts is under scientists and engineers investigation.

Composite materials which are formed by the incorporation of a basic structural material into a second substance, the matrix, are one of the most successful examples of this investigation.

On the other hand, decreasing the size of the structural building blocks which are incorporated into the matrix to the same level as the matrix building blocks could lead to more homogeneous materials that allow a further fine tuning of materials' properties on the molecular and nanoscale level, generating novel materials that either show characteristics in between the two original phases or even new properties.

Therefore the term hybrid material is used, in materials science, to identify something that is obtained by mixing components and that the interphase between these components is increased compared to a composite material; in particular, the high homogeneity of the hybrid materials suggests that the two moieties are blended at the nanometer level.^{4,5}

Otherwise, the hybrid material indicates a class of covalent bonding organic/inorganic components, named *class II*. In contrast with the *class I* of composite materials where interactions between organic and inorganic components are provided by hydrogen bonds, Van der Waals forces and ionic bonds, or are electrostatic in nature.

Considering the industrial era, successful commercial hybrid organic–inorganic polymers have been part of manufacturing technology since the 1950s⁶.

Some of the oldest and most famous organic–inorganic industrial representatives are certainly coming from the paint industries, where inorganic nano-pigments are suspended in organic mixtures (solvents, surfactants, etc.). While the name of “hybrid” materials was not evoked at that time, the wide increase of work on organic–inorganic structures was pursued with the development of the polymer industry.

The concept of “hybrid organic–inorganic” nanocomposites exploded in the eighties with the expansion of soft inorganic chemistry processes⁷, and consisted of inorganic and organic building blocks distributed on the molecular or nanoscale.

The modern concept of “organic-inorganic hybrid materials” emerged recently, when the research turned to more sophisticated materials with a higher added value, associated to the development of composites and molecular materials where the organic and inorganic component interact at a molecular level.

As mentioned the first interest in the development of hybrid materials was mainly based on the design of hybrid polymers with special emphasis on structural hybrid materials.

The choice of the polymers is usually guided mainly by their mechanical and thermal behavior. But, other properties such as hydrophobic/hydrophilic balance, chemical stability, bio-compatibility, optical and/or electronic properties and chemical functionalities (i.e. solvation, wettability, templating effect, etc.) have to be considered in the choice of the organic component.

The organic in many cases allows also easy shaping and better processing of the materials. The inorganic components provide mechanical and thermal stability, but also new functionalities that depend on the chemical nature, the structure, the size, and crystallinity of the inorganic phase (silica, transition metal oxides, metallic phosphates, nanoclays, nanometals, and metal chalcogenides). Indeed, the inorganic component can implement or improve electronic, magnetic and redox properties, density, refraction index, etc.⁷

A variety of silicates or polysiloxanes modified with organic group or networks for the improvement of mechanical properties were the first type of hybrid materials investigated. The expectations for hybrid materials go further than mechanical strength, thermal and chemical stability.

So, in addition to those structural materials and applications, many recent efforts have centered on the design of other types of hybrid materials which explore other fields as electronic hybrids, used in electronics (transistors, diodes), and functional hybrids. Chemical activity is the main characteristic of functional hybrid materials.

The optical and electrical properties, luminescence, ionic conductivity, and selectivity, as well as chemical or biochemical activity, giving way to materials that can be applied for: sensors, selective membranes, all sorts of electrochemical

devices, from actuators to batteries or electrochemical supercapacitors, supported catalysts or photo-electrochemical energy conversion cells, etc.

In these functional materials mechanical properties are secondary (still also important) and the emphasis is on reactivity, reaction rates, reversibility or specificity. The hybrid approach can also be useful in this context by combining organic and inorganic species with complementary properties and reactivities.^{8,9}

Therefore, independently of the types or applications, as well as the nature of the interface between organic and inorganic components, a second important feature in the tailoring of hybrid networks concerns the chemical pathways that are used to design a given hybrid material.

In recent years, the concept of functional nanostructures as hybrid materials has received little attention.

For example, hybrid materials based on block copolymer templating inorganic nanoparticles. The block copolymers are acting not only as nano-reactors to control the size and size distribution of the nanoparticles but also direct the assembly of the nanoparticles into well-defined structures.

Hence, is possible to fabricate a large diversity of functional nanostructures including spheres, rods, and ring-like nano-objects as well as vesicles, whose core can be loaded with different inorganic materials.

The possibility to graft organic functional groups on the walls pore of a porous material allows to product a new class at high performances organic-inorganic hybrid materials^{10,11}.

Three pathways are available for the synthesis of porous hybrid materials based on organosilica units:

- i*) the subsequent modification of the pore surface of a purely inorganic silica material (“grafting”),
- ii*) the simultaneous condensation of corresponding silica and organosilicas precursors (“co-condensation”) and
- iii*) the incorporation of organic groups as bridging components directly and specifically into the pore walls by the use of bis-silylated single-source organosilica precursors (Periodic Mesoporous Organosilicas (PMO))¹².

In this thesis work we will focus on both hybrid systems, the ionic transition metal complexes incorporated into silica porous matrix, and classical organic/inorganic hybrid materials for efficient dye-sensitized solar cells.¹³

In fact active optical applications of hybrid materials might present a very attractive field. Indeed, the exploitation of active optical properties of photoactive coatings and systems is strongly emerging.

In particular, hybrid materials having excellent laser efficiency and good photostability,^{14,15} very fast photochromic response,¹⁶ very high and stable second order non-linear optical response¹⁷, or being original pH sensors,¹⁸ electroluminescent diodes¹⁹ or hybrid liquid crystals²⁰ have been reported in the past years.

1.2 Optoelectronic devices

Nowadays, the optoelectronic system research has been motivated by the potential application of this class of devices in many areas of society. Optical excitation of device leads to useful processes such as light-energy conversion in the form of electricity in solar cells, optical sensors for detection of trace quantities of chemicals, smart windows that on one hand can control the amount of light passing through, or better this class of devices is useful from simple household appliances and multimedia systems to communications, computing, and medical instruments. Design of these devices requires ability to organize molecules on a nanometric scale, with fine control on their arrangement: distribution, mobility, spectral and redox properties.^{21,22,23,24,25,26,27} Structural organization of these components by controlled molecular engineering allowing synergistic effects is a major feature of these systems.

Optoelectronic devices — from light-emitting diodes (LEDs), solar cells to light-emitting electrochemical cells (LEECs) — are specifically designed to optimize the light absorption and emission, resulting in high conversion efficiency.

Central to realizing a high-performance and more useful optoelectronic device is the development at the nanoscale that satisfies the trend of a more compact and powerful systems. In the last two decades there have been intense efforts in fabricating organized molecules on a nanometric scale, with a particular attention to the control of their arrangement.

In the photosynthesis of a natural system, **figure 1.1**, we can find a perfect

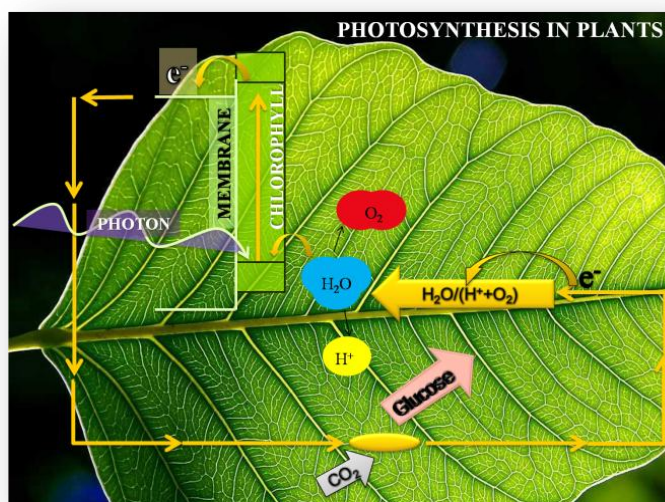


Figure 1.1 Photosynthesis schematic process.

example of a device for light-energy conversion.

In the last two decades there have been intense efforts in the fabrication of a similar efficient system because of lacks of knowledge on how to organize molecules on a nanometric scale and to control their reaction efficiencies or improve their structure. The main component, the chromophore, like electron donor and acceptor, is assembled in a high organized structure, and assures a high efficiency photon-to-electron conversion. In artificial systems, we aim for reaching green plant light-energy conversion efficiency, using different sensitizers that absorb light and engage in electron-transfer reaction with suitable electron donors or acceptors. One of the most problematic limitations is the random distribution of these components into the device structure, to achieve the control over the way the components distribute themselves and diffuse towards one another, it is fundamental to confine them in some host supports or matrices.

The term supramolecular is often used to represent such an assembly of several molecules and molecular units.^{28,29,30,31}

In natural systems, the efficiency of light energy conversion is achieved thanks to a highly organized assembly of a chromophore, electron donor and electron acceptor.

Therefore the optoelectronic devices, that involve a photo-sensitizer that absorbs the light and engages in electron-transfer reaction with suitable electron donors or acceptors, have to achieve a controlled spatial distribution, orientation and mutual diffusion of all their components³².

In this thesis work we investigated mesoporous semiconductor surface as the host matrix support.

Major advances in the fields of Sol–Gel chemistry in the last two decades^{33,34,35,36,37,38,39} now allow controlled fabrication of micro-, meso- and nano-sized structures.⁴⁰

Mesoporous materials offer pores that can be filled with a sensitizer and satisfy optoelectronic device paradigm with a high contact between the chromophore and the charged contact of the electric cell.

1.2.1 Dye-sensitized solar cells.

Global environmental concerns and the finite nature of fossil fuels have led to increased interest in the development of renewable energy, and solar energy has emerged as one of the best candidates in this respect. Though conventional photovoltaic devices such as silicon-based solar cells, are promising for the direct conversion of photons into electrons, the prohibitive cost of these cells is uncompetitive with conventional power-generating methods.⁴¹ Providing a cost effective and affordable solar energy conversion technology is still a challenge nowadays.⁴²

In a classical p-n junction solar cell a narrow bandgap semiconductor takes over the function of the light absorber and the charge transport material. **Figure 1.2** Interband excitation by absorption of a photon of $h\nu > E_{\text{bandgap}}$ promotes permits to an electron to pass from the valence band to the conduction band, leaving a hole in the valence band.

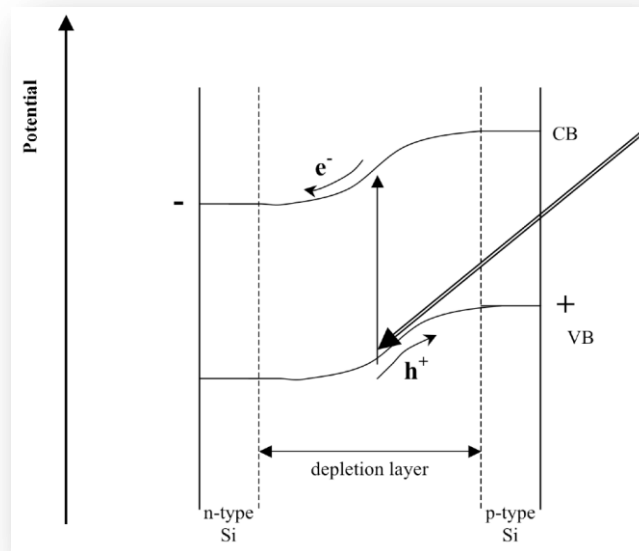


Figure 1.2. Energy band scheme of a p-n junction for Silicon.

A migration occurs inside or close to the depletion layer of the p-n junction because of the presence of the internal built-in field that split the electron-hole pair and the two charges migrate in opposing direction towards the collecting electrode. Also impurities and microscopic defects can act as recombination centres, decreasing the device efficiency; thereby silicon solar cells are expensive due to

their high-energy consuming production methods that require extremely pure starting materials in addition to sophisticated technical procedures.⁴³

Because of these physical limitations a lot of effort has been invested into the search for new materials. Consequently interest in the prospect of producing cheap alternatives to silicon types is still on the rise. In 1839 Becquerell⁴⁴ observed for the first time a photovoltaic effect on an illuminated silver electrode, immersed in an iodine/iodide electrolyte. In the 1873 the first sensitized semiconductor was studied by Vogel for application in photography. About 15 years later Moser⁴⁵ applied this study to a silver plate sensitized with an erythrosine dye, observing an enhancement of photoelectric effect. But a systematic study of dye-sensitization mechanism was developed by Tributsch and Gerischer in 1968.

Gerischer early studies were fundamental to understand electron-transfer processes for a semiconductor in a redox electrolyte; the step forward was in combining the performance of a porous matrix with the dye properties, increasing the amount of absorbed dye in the semiconductor bulk. The concept of dye-sensitized solar cells, introduced by O'Regan and Grätzel in 1991, was the first promising candidate as an alternative to conventional solar cells.⁴⁶

The real achievement of Grätzel and his group was to create a 3 orders of magnitude larger TiO₂ layer than a normal semiconductor device, consequently a more efficient device.

The molecular engineering of organic sensitizer leads to a drastic improvement in charge injection efficiency by the synthetization of new class of organic dye with an anchoring group. Recently, thanks to these innovations, the performance of dye-sensitized solar cells based on organic dyes has been remarkably improved and achieved impressive efficiencies in the range of 8 ~ 9.7%.^{47, 48, 49, 50, 51, 52, 53,54}

Dye-sensitized solar cells (DSSCs) are a non-conventional photovoltaic technology that has attracted significant attention because of their high conversion efficiencies and low cost.⁵⁵ A typical DSSC contains five components: 1) a conductive mechanical support, 2) a semiconductor film, 3) a sensitizer, 4) an electrolyte, and 5) a counter electrode. The total efficiency of the dye-sensitized solar cell depends on the optimization and compatibility of each of these constituents.

Therefore nowadays the new materials like organic molecules and polymers offer several advantages compared to inorganic ones. The properties of a tailored system and the inherent features of organic materials lead to an amazing potential in tuning physical properties such as band gap, valance and conduction energies, charge transport, solubility, morphological properties.

Furthermore organic materials present an easy large scale production and as a consequence economic advantages compared to inorganic materials. Ease of production, due to the small quantities needed for device preparation and the purification, organic materials have furthermore an economic advantage compared to inorganic material.

Basic difference between the conventional solar cells and the dye-sensitized ones, are:

- Dye-sensitized solar cells separate the two functions provided by silicon in a traditional cell design. Normally the silicon acts as both the source of photoelectrons, as well as providing the electric field to separate the charges and create a current. In the dye-sensitized solar cell, the bulk of the semiconductor is used exclusively for charge transport, the photoelectrons are provided from a separate photosensitive dye. Charge separation occurs at the surfaces between the dye, semiconductor and electrolyte.
- Light adsorption and charge carrier transport are separated in dye-sensitized solar cell, whereas both processes are established by the semiconductor in the conventional cell.

The basic functional principle of a dye-sensitized solid-state heterojunction is shown in **Figure 1.3**.

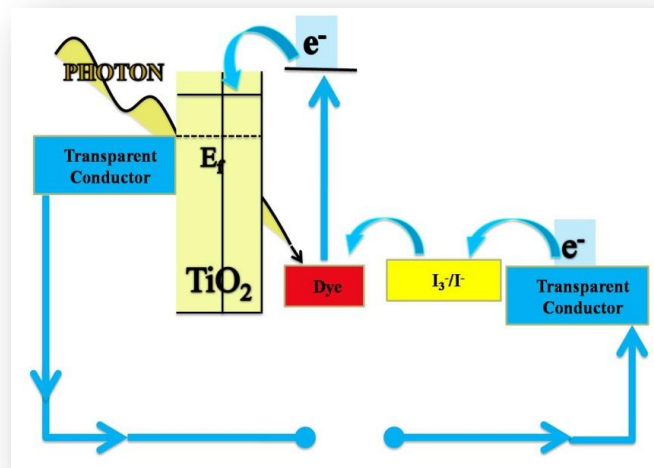


Figure 1.3. Simplified energy band schemes for dye-sensitized solar cells.

After the absorption of a photon the excited dye molecule inject an electron in the conduction band of TiO₂. The electron, by a percolation process, is diffused through the porous TiO₂ matrix into the current collector like the conducting glass. During this process the oxidized dye is regenerated by an organic solvent containing a redox system that acts as an electron donor. The cycle is closed when the counter electrode then regenerates the electron donor.

The choice of the electron donor is kinetically crucial in order to avoid a recombination of the oxidized dye with the just injected electron.

The characteristics of the electrolyte must also accommodate the wide range of temperatures to which the cell is exposed in normal outdoor service.

Under long storage or exposure to open air, solvent exudation is unavoidable, leading to low conversion efficiency.⁵⁶

Thereby the study of the photoinduced charges dynamics is fundamental. The following energetic scheme is a time frames of the reaction for the interfacial electron transfer processes after charge injection from the electronic excited state S* of a dye-sensitizer to the conduction band (cb) of a semiconductor (SC).⁵⁷

Eqn. (1) Photoexcitation: $S SC \xrightleftharpoons{h\nu} S^* SC$
Eqn. (2) Charge injection: $S^* SC \rightarrow e^-(SC) + S^+ SC < [20\text{fs} - 15\text{ps}]$
Eqn. (3) Dye regeneration: $S^+ SC + D \rightarrow S SC + D^+ [0.1 - 30]\mu\text{s}$
Eqn. (4-5) Charge recombination: $S^* SC + e^- \rightarrow S SC [0.2 - 0.8]\text{ms}$ $D^+ + e^- \rightarrow D > [10\text{ms}]$

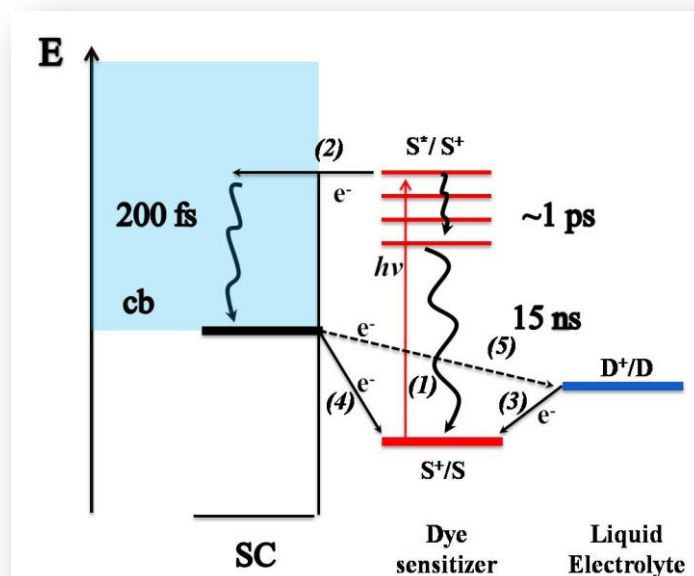


Figura 1.4. Energetic scheme.

1.2.2 Light-emitting devices

Over the past two decades impressive advances have been achieved in the field of light-emitting devices, which are being developed for display and lighting applications.

Light emitting diodes, commonly named LED, are the reverse of photovoltaic cells⁵⁸. **Figure 1.5**.

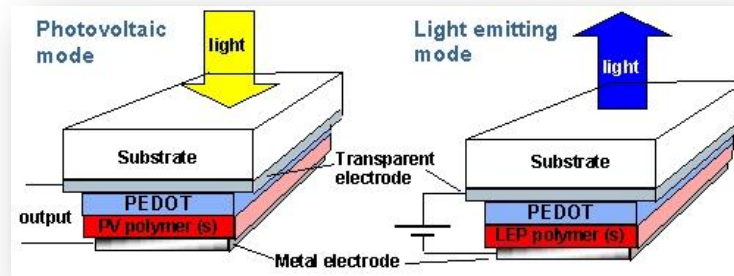


Figure 1.5. Example of two different optoelectronic device operating modes.

While in this last the light is used to produce an electrical voltage, in a LED a voltage is applied to produce light⁵⁹. Basically, the electroluminescence occurs when a sufficiently large forward-bias voltage is applied across a $p-n$ junction, where minority carrier injection takes place and radiative recombination produces a photon⁶⁰.

When a p -type semiconductor is kept in contact with an n -type, electrons move from the n - to the p -doped layer. At the thermodynamical equilibrium the energy levels of the semiconductors are bent and two regions depleted of majority carriers are formed in both sides of the interface.

In this situation, the p -semiconductor is depleted of holes, the n -semiconductor is depleted of electrons and a potential barrier is formed, which hinders the current flow though the interface. If this junction is forward biased, the potential barrier is lowered and the injected electrons in p -type side recombine with the holes and the injected holes in the n -type side recombine with the electrons⁶¹. This current flow usually gives rise to an excitation, which results in a radiative recombination process⁶².

All theoretical considerations about LED involve inorganic semiconductors because of the pioneering works on light emission from GaAs $p-n$ junctions.^{63,64,65}

Polymer-based light emitting diodes¹³⁵, commonly called “polymer, PLED” or “organic LED, OLED”, were studied in 1963, but the first work, was only published in 1990.

The light emission process in such devices depends on several parameters, such as charge injection, charge carriers mobility, electron-hole recombination with radiative decay and emission. Charge injection is assigned to the efficiency that the metallic electrodes inject carriers into the polymer film and depends on the Fermi level of the metals. Thus, a hole-injector metal must have high work function, such as: Au or ITO electrodes, and an electron injector metal must possess low work function, such as alkaline or alkaline earth metals.

Polymer based LED present a series of interesting applications, when compared to inorganic materials. The aim of using organic materials as electroluminescent component in a LED, despite their poor light emission properties, results from the difficulty of assembling large areas devices with inorganic semiconductors. Additionally, the mechanical properties of conducting polymers open the possibility of constructing flat panel displays.

Devices fabricated with these materials generally require a multilayer structure and cathodes made of low work function metals in order to achieve high efficiencies and low operating voltages. Recently, the efficiency of small molecule devices has been further increased by employing phosphorescent dyes in the electroluminescent layer since phosphorescent molecules emit from their triplet state.^{66,67}

That notwithstanding, the limited operating life of organic light-emitting devices (OLEDs) is an important factor preventing their wide-scale commercial use in various display applications.

In the mid-1990s Pei and co-workers showed that the properties of organic light-emitting diodes (OLEDs) could be completely transformed by including high concentration of mobile ions in the emissive layer.^{68,69,70}

The light-emitting electrochemical cell (LEEC) is an exciting device concept with potential for various light-emitting applications, such as in thin-film displays,⁷¹ solid-state lighting,⁷² and injection lasers,⁷³ since its successful operation has been demonstrated to be remarkably insensitive to electrode material selection and

active-material thickness, and since impressive power efficiencies have been reported.⁷⁴

LECs generally require only a single emissive layer, which consists both electronic and ionic conductors sandwiched between two electrodes; mobile ions contained in the solution drift toward electrodes under a sufficient applied bias, cations and anions induce doping (oxidation and reduction) of the emissive material close to the electrodes, that is, *p*-type near the anode and *n*-type near the cathode, respectively.

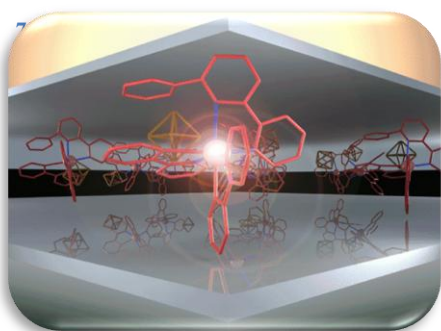


Figure 1.6. Light-emitting electrochemical cells (LECs) based on ionic transition-metal complexes are among the simplest electroluminescent devices as they use only one active component in a mono-or bi-layer architecture, operate with air-stable electrodes and are prepared using solution-based technologies.

The doped regions induce ohmic contacts with the electrodes and consequently facilitate the injection of both holes and electrons, which recombine at the junction between *p*- and *n*-type regions. As a result, a single-layered LEC device have low electrical resistance and form ohmic contacts with the metal electrodes, consequently can be operated at very low voltages with balanced carrier injection, giving high power efficiencies. Furthermore, air-stable metals, for example, Au and Ag, can be used since carrier injection in LECs is relatively insensitive to work functions of electrodes.⁷⁶

One limitation in LEC performance comes from the low ionic conductivity of polymeric electrolytes and the phase segregation occurring during LEC operation between the electroluminescent polymer and the solid electrolyte. To improve the ionic conductivity of the blend, Heeger and co-workers included a bifunctional liquid additive to the electroluminescent layer⁷⁷.

Chapter 2

Luminescent mesostructured materials

Early-1990s was particularly rich period for nanotechnologies, with particular relevance to the new materials synthesis, in addition to the preliminary LEEC investigations, by Pei and co-workers, and the first studies on dye-sensitized solar cell, by O'Regan and Graetzel, the discovery of surfactant-organized silicas and silicates assured attractive applications as catalyst supports, optical materials, sensors, membranes, and selective adsorbents.

As mentioned previously, hybrid materials are a mix of organic and inorganic components at the molecular scale.

Mesoporous materials result from the combination of an organic template acting as a structure-directing agent with an inorganic precursor. They are obtained from hybrid materials by removing the surfactant template. **Figure 2.1**

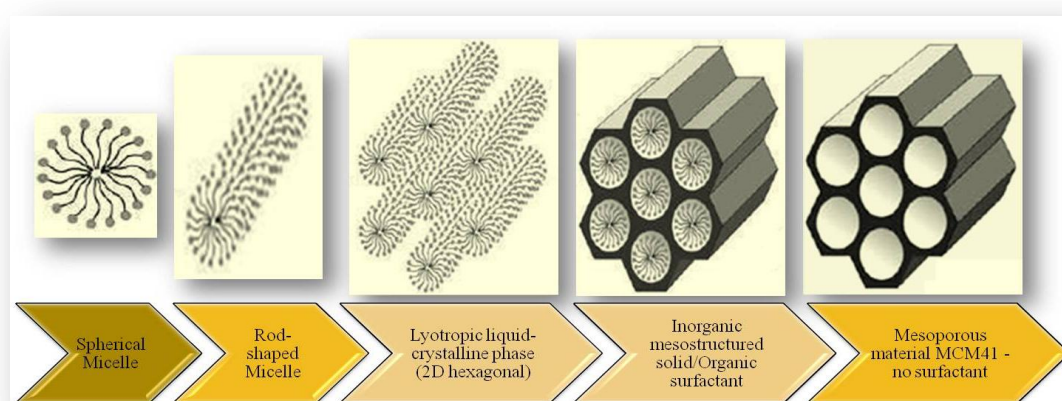


Figure 2.1. Pathways for the formation of a mesoporous hybrid material. [Hoffmann et al., 2006]

The *liquid-crystal templating* mechanism was used during this thesis work, to fabricate mesostructured materials, in which the condensation of the silica precursor is not the dominant factor for the formation of the mesoporous structure⁷⁸. The amphiphilic molecules organize themselves in liquid crystal phases independently of the inorganic crystallization, and the polymerization of the silica precursor takes place around the self-assembled aggregate acting as a template⁷⁹.

The LCT is the dominant mechanism when the surfactant concentration is so high that the liquid crystals are already formed when the inorganic precursor starts organizing itself around them⁸⁰.

Ordered mesostructured powders are generally functionalized with a dye through two different methods: co-condensation (*one-pot method*) of an appropriate inorganic source and the surfactant self-assembling species doped with an optically active compound, or grafting post-synthesis, due to the presence of a high density of silanol groups on the pore surface of mesoporous material to which guest species may be attached⁸¹.

Among the wide variety of films synthesis, thin mesoporous films were produced by evaporation-induced self-assembly (EISA)⁸² method.⁸³ The coating solution was prepared by the sol-gel method, this process allows the preparation of highly organized and porous layers.

The removal of the organic template is usually performed by calcination or solvent extraction. The first way is cheaper, but can lead to structural problems depending on the inorganic precursor used and on the eventual presence of functional groups, if functional organic groups are present, then the calcination becomes very risky to perform because the organic group could be destroyed by the high temperatures. Silica is a very good precursor, being resistant and stable enough to maintain its amorphous structure at the temperatures of calcination (500 – 600°C). Many other precursors could crystallize at these temperatures, and this would create several defects in the material because of the strong curvature of the pores, being best compatible with amorphous wall structures⁸⁴.

In the solvent extraction, the material is functionalized after the removal of the template, that is, by grafting the organic groups into the channels walls during a post-synthesis process.

There are different possible ways to classify porous materials. One is related to the definition of pore size furnished by the International Union of Pure and Applied Chemistry (IUPAC)⁸⁵. According to the IUPAC, porous materials can be divided into:

- microporous materials, if their pore size is below 2 nm,
- mesoporous materials, if their pore size is between 2 and 50 nm,

- macroporous materials, if their pore size is bigger than 50 nm.

Porous materials can also be classified according to their degree of order: fully crystalline (zeolites); ordered on a mesoscopic length scale, but amorphous on the atomic length scale (surfactant-templated materials); or fully disordered (silica gels)⁷.

Some mesoporous materials are also mesostructured, because a monosized pore is coupled with long range ordered voids. Mesostructures depend by chemical and processing parameters, therefore a great number of characteristics can be tuned, as well large active surface area, pore dimension, and pore shape⁸⁶. In general mesostructured materials are defined as mesoporous materials before calcination or chemical extraction.

Mesostructured materials are highly versatile substrates for the formation of functional materials, in particular silica at first and then titania mesoporous materials have led to many promising applications in areas ranging from photovoltaics and photocatalysis to photo-electrochromics and sensors. Many of these applications depend not only on the properties of the TiO₂ or SiO₂ material itself but also on the modifications of the object host, e.g., with inorganic and organic dyes.

Photo-electronically functional molecules can form specific arrangements in mesopore nanospace, possibly leading to novel functions, which cannot be obtained in open space.



Figure 2.2 Mesostructured hybrid materials, containing inside the cavities a luminescent neutral cyclometallated Iridium(III) complex, using a one-pot method.

2.1 Materials

2.1.1 Mesoporous powder and film

Ordered mesoporous silicates have attracted a great deal of interest in the past decade because of their use in catalysis, separations, sensors, drug delivery, and optical devices. Mesoporous silica nanoparticles were first synthesized in 1992, through a hydrothermal sol-gel synthesis⁸⁷, by researchers working for the Mobil Corporation. They had a uniform hexagonal array of pores which had sizes between 20 and 100 Angstrom.⁸⁸ This material was named Mobil Crystalline of Materials, or MCM-41.⁸⁹ Discovery of the M41S family of materials ended the long-standing pore-size constraint of zeolites.^{10,90}

Six years later, researchers at the University of California in Santa Barbara announced that they had produced silica nanoparticles with much larger 20 - 300 Angstrom pores⁹¹. The material was named Santa Barbara Amorphous type material, or SBA-15. These particles also have a hexagonal array of pores. At the first these types of particles was used as molecular sieves.

Like zeolites, mesoporous materials are characterized by very large specific surface areas, ordered pore systems, and well-defined pore radius distributions.

To enable practical applications of mesoporous materials, synthesis strategies have been developed to form thin films.⁹²

The sol-gel synthesis is a versatile solution process initially used for the preparation of inorganic materials such as glasses and ceramics of high purity and homogeneity.⁹³ It involves the transition of a system from a liquid “sol” into a solid “gel” phase and has been the subject of several books and reviews.^{10,94} The sol-gel process can ordinarily be divided into the following steps: forming a solution, gelation, aging, drying, and densification. In the preparation of a silica film, one starts with an appropriate alkoxide, tetraethyl orthosilicate (TEOS), which is mixed with water and a mutual solvent, such as ethanol, to form a solution, hydrolysis leads to the formation of silanol groups Si-OH. These species are only intermediates as they react further, i.e. condense, to form siloxane Si-O-Si groups. As the hydrolysis and condensation reactions continue, viscosity increases until the “sol” ceases to flow and form the “gel”. There are several parameters which influence the hydrolysis and condensation reactions (sol-gel process), including the activity of metal alkoxide, water/alkoxide ratio, solution pH, temperature, and nature of the solvent and additive.

In this study, mesoporous silica powders are synthesized by reacting Tetraethyl orthosilicate using two different surfactants. **Figure 2.3.** The selected surfactants are the cationic Cetyltrimethyl ammonium bromide (CTAB, 99.8 wt%), purchased from Alfa Aesar, formed by amphiphilic molecules with a polar head group and an hydrophobic chain.



Figure 2.3 Chemical formula and shape of Pluronic 123 (left) and CTABr (right) micelles.

The non-ionic triblock copolymer poly(ethylene glycol)-block-poly(propylene glycol)-block-poly(ethylene glycol) (P123), purchased from Sigma-Aldrich.

In one molecule ethylene oxide (EO)_n monomer blocks are separated by a block of propylene oxide (PO)_n. The hydrophobic core of the micelles formed from such polymers is composed of hydrophobic PO part, while hydrophilic EO blocks are pointing outwards.

The result is an inorganic scaffold with a regular arrangement of pores. The template can then be removed by washing with a solvent like ethanol⁹⁵.

MCM-41 sample, obtained with CTABr surfactant, consists of amorphous silica and shows the hexagonal symmetry of the pore ordering (space group: p6m). The pores can be tailored to diameters between $d_p = 1.5$ and 20 nm, largest pores can only be obtained with the addition of swelling agents. The pore walls are quite thin with a thickness between 1 and 1.5 nm. The presence of these thin pore walls leads to low chemical and hydrothermal stabilities^{96, 97}

SBA-15 sample was obtained with Pluronic P123 surfactant, is a combined micro- and mesoporous material with hexagonally ordered tunable uniform mesopores (4–14 nm)^{98,99}. It consists of thick microporous silica pore walls responsible for the high hydrothermal stability of SBA-15 compared to other mesoporous materials with thin pore walls like MCM-41.

Both the materials show hexagonally arranged channels, large surface area [$< 1000\text{m}^2/\text{g}$] and a characteristic long range ordered framework with uniform mesopores. **Figure 2.4.**

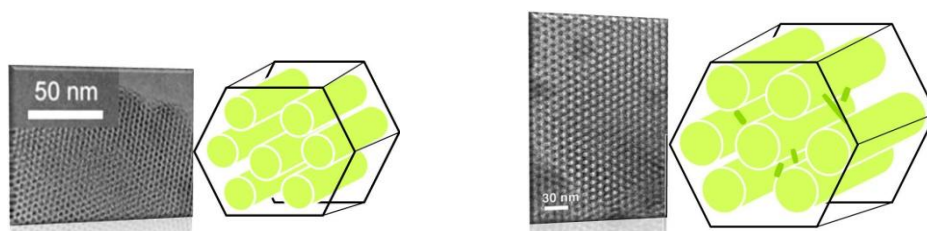


Figure 2.4. MCM-41 and SBA-15 materials with characteristic morphologies. TEM images by V. Meynen et al. / *Microporous and Mesoporous Materials* 125 (2009)

I

n 1999, Brinker et al.¹⁰⁰ reported a new approach, which resulted in highly ordered mesostructured thin films, called “Evaporation Induced Self Assembly” (EISA). One of the most important advantages of this synthesis route is the short mesophase formation (a few minutes).

Hybrid mesostructured silica films were prepared adding a surfactant, Pluronic F127 (EO106-PO70-EO106), to a solution of tetraethoxysilane (TEOS), ethanol (EtOH), water, and chloridric acid (HCl). Then a spatially-patterned¹⁰¹ silica thin-film mesophases is formed thanks to the preferential evaporation of alcohol that accompanies the dip-coating deposition.^{102,103,104,105,106}

2.1.2 Ionic transition-metal complexes

For a long time people thought that the luminescent dyes used since the work of Tang et al. are theoretically limited to an internal conversion efficiency of 25%¹⁰⁷. This factor arrives from quantum mechanics, where 75% of the charge wave functions are of the non-emissive triplet case and only 25% of the singlet case, allowing radiative recombination. Taken into account that only one-fifth of the created photons can leave the device, the external quantum efficiency was limited to 5%¹⁰⁸. But, in contrast to this, the family of the so-called phosphorescent dyes (triplet emitters) permits the opening of an additional radiative recombination channel and harvesting of up to nearly 100% of the excited states to photon creation. Responsible for this is the presence of heavy metal atoms such as Ir¹⁰⁹, leading to a strong spin-orbit coupling¹¹⁰.

Iridium(III) cyclometalated complexes are attracting widespread interest because of their unique photophysical properties and applications in organic light-emitting

diodes (OLEDs). Neutral Ir cyclometalated complexes in OLEDs showed up to 19% external quantum efficiencies^{111,112,113,114}.

As mentioned in the previous chapter, an alternative to the OLEDs, which require a complicated multilayered structure for charge injection, transport, and light emission, is the light-emitting electrochemical cell (LEC)^{115,116,117,118,119}, in which the use of ionic complexes facilitates electronic charge injection into the light-emitting film^{32,120,121}.

OLEDs and LECs require a tunable phosphorescence wavelength emitter with a very high phosphorescent quantum yields.

A strategy to tune the emission color in Ir(III) complexes relies on the selective HOMO stabilization and/or LUMO destabilization of the complex. Mixed ligand Ir complexes with C^N cyclometalating ligands, are particularly appealing in this respect, since the two types of ligands can be almost independently functionalized to obtain the desired color tuning¹²².

In particular, electron-withdrawing substituents on the C^N ligands decrease the donation to the metal and therefore stabilize the metal-based HOMO.

Electron-releasing substituents on the C^N ligand, lead, on the other hand, to destabilization of the ligand-based LUMO, ultimately leading to increased HOMO–LUMO gaps and emission energies.

On the other hand, the control of the factors that act in order to increase the emission quantum yields in mixed ligand complexes, is a daunting task. It is indeed generally assumed that emission quantum yields should increase with increasing emission energy, due to the increase of the radiative rate constant and decrease of the non-radiative rate constants. These follow, respectively, the Einstein law of spontaneous emission¹²³ and the so-called energy gap law¹²⁴, even though exceptions to these rules are quite common.

Photophysical Properties

The photophysics of polypyridyl complexes of Ir can be understood with the aid of an energy level diagram, as shown in **Figure 2.5**.

In these complexes there are three possible types of excited states: (a) metal-centered (MC) excited states, which are due to promotion of an electron from t_{2g} to e_g orbitals; (b) ligand-centered (LC) states that are π – π^* transitions; (c) MLCT states. An electronic transition from metal t_{2g} orbitals to empty ligand orbitals

without spin change is allowed, which is called singlet–singlet absorption. The allowed transitions are identified by large extinction coefficients. The transitions

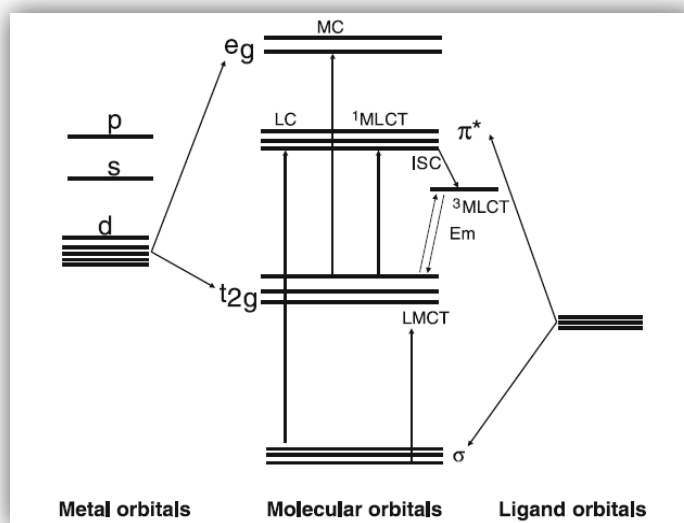


Figure 2. Schematic and simplified molecular orbital diagram for an octahedral d6 metal complex involving 2-phenylpyridine (C3 symmetry)-type ligands in which various possible transitions are indicated.

with spin change are called singlet–triplet absorption, which are forbidden and associated with small extinction coefficients.

However, the excited singlet state may be involved in spin flip, which is called intersystem crossing (ISC), resulting in an excited triplet state. The radiative process of a singlet and triplet excited state to a singlet ground state is termed fluorescence and phosphorescence, respectively. The excited singlet states associated with LC π – π^* and MLCT transition can undergo ISC into the triplet state efficiently in Ir complexes due to spin-orbit coupling, resulting in enhanced phosphorescence quantum yields.

For the cyclometalated Ir complexes, the wave function of the excited triplet state, responsible for phosphorescence, is principally expressed as a combination of the LC and the MLCT excited triplet state. However, not all the complexes are highly luminescent because of the different deactivation pathways²⁷.

Tuning of Phosphorescence Colors in Neutral Iridium Complexes

Neutral Ir complexes were obtained by an orthometalation reaction with ligands that contain a benzene ring attached to a functional group containing a donor atom such as 2-phenylpyridine (ppy)¹²⁵. The coordination of ppy ligands to metal is analogous to that found in 2,2'-bipyridine except that nitrogen is replaced by

carbon anion¹²⁶. In a typical example, three ppy ligands coordinate around Ir(III) resulting in a neutral complex, in which the phenyl group carries a formal negative charge due to loss of proton and subsequent orthometalation to Ir metal. The HOMO in tris-phenylpyridine Ir(III) [Ir(ppy)₃] is principally composed of orbitals of the phenyl ring and the metal d orbitals. The pyridine is formally neutral and is the major contributor to the LUMO in the [Ir(ppy)₃] complex¹²⁷.

The absorption spectra of [Ir(ppy)₃] display strong ligand-to-ligand (LC, $\pi-\pi^*$) and MLCT transitions in the UV and the visible region, respectively.

The MLCT transition bands are lower in energy than the LC $\pi-\pi^*$ transitions.

The excited triplet state shows strong phosphorescence in the green region at around 515 nm, with an excited state lifetime of 2 μs ¹²⁸.

In order to tune the phosphorescence color of [Ir(ppy)₃], Watts et al. synthesized several substituted ppy-based neutral Ir complexes^{45,129,130}. The phosphorescence lifetime of these complexes is in the range of 2–3 μs in nitrogen-saturated acetonitrile at room temperature⁴⁶.

Controlling Quantum Yields in Iridium Complexes

Orthometalated Ir complexes are known to have highest triplet emission quantum yields due to several factors^{131,132}:

- Ir has a large d-orbital splitting compared to other metals in the group.
- Strong ligand field strength of the ppy anionic ligand increases the d-orbital splitting, leading to an enlarged gap between the e_g orbitals of Ir and the LUMO of the ligand.
- Close-lying $\pi-\pi^*$ and MLCT transitions, together with the heavy atom effect, enhance the spin-orbit coupling.

However, the mixed ligand cationic Ir complexes show appreciably lower quantum yields compared to the tris-orthometalated Ir complexes because of the lower LUMO orbitals of the 2,2'-bipyridine ligand^{32,45,133}. One strategy to increase the quantum yields of Ir complexes is to introduce F and/or CF₃ substituents. This results in a stabilization of both the HOMO and the LUMO. Since the HOMO stabilization is larger than that of the LUMO, this leads to an increase in the gap between HOMO–LUMO¹³⁴.

Application

Introducing dye molecules, with appropriate energy levels for color tuning, in the emitting layer of a light-emitting device, is an established way to improve the optoelectronic device performance.

Besides this aspect, *doping* also leads to a change of the transport characteristics and to a considerable increase of the lifetime and of the quantum efficiency.

The common way of device realization is to mix a small concentration of a highly phosphorescent guest into a host material with suitable charge transport abilities. Taking into account an unchanged out-coupling factor of one-fifth, the theoretical external quantum efficiency for the triplet dyes jumps up to 20%¹³⁵.

As stated above, photochemical, photophysical and electrochemical properties of Ir(III) cyclometalated phenylpyridine (ppy) compounds, has been intensively investigated because of their potential application as light-emitting device and solar cells²⁷.

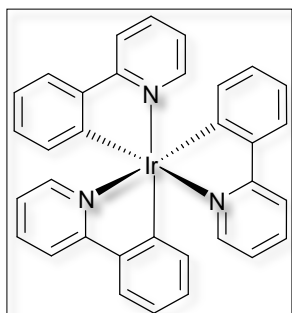


Figure 2.6. Chemical structure of *fac*-isomer of the neutral homoleptic tris-cyclometalated 2-phenylpyridine Iridium(III) complex, *fac*-Ir(ppy)₃ where Hppy= 2-phenylpyridine.

Luminescent iridium(III) complexes are highly appealing due to their wider range of emission energies, longer lifetimes, higher luminescence quantum yields, and for their properties of being liquid crystal systems.

However, it is also noteworthy that the actual performances of these molecular materials can be often severely limited because of the reduced emission efficiency in the solid state, owing to a concentration-driven quenching.¹³⁶

Although different approaches, such as the dispersion of the emitters in a polymeric matrix or the introduction of sterically hindered substituents into the auxiliary ligands^{137,138} have been explored to limit the concentration quenching effect, at present none of them seem to sufficiently solve this problem. In this context, mesostructured materials can be a useful way for the emitting Iridium(III) complexes dispersion, thus obtaining best performing Iridium(III)-based

luminescent materials. In fact, an homoleptic tris-cyclometalated Iridium(III) surfactant has been recently employed in the synthesis of an amphiphile/silica co-assembled nanocomposite which was successfully used as active layer for organic light-emitting diode. This provided a better performing device with respect to the one based on the pristine solid.¹³⁹

2.2 Materials preparation

The incorporation of functionalities, such as luminescent Iridium(III) complex, can generally be achieved in three ways. *Grafting* is a post-synthesis treatment of a mesoporous material by which a subsequent attachment of functional molecules onto a mesoporous silica matrix takes place. **Figure 2.7.**

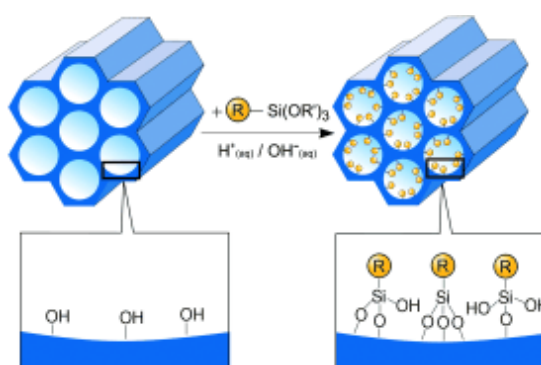


Figure 2.7. Grafting (post-synthetic functionalization) for organic modification of mesoporous pure silica phases with terminal organosilanes of type $(R'O)_3SiR$. R' =organic functional group.

Through *incorporation* of condensable organosilane inside the pore wall of the porous mesophase that lead to periodic mesoporous organosilicas (PMOs)¹⁴⁰, unlike in organic functionalized mesoporous silica phases obtained via grafting or co-condensation procedures the organic groups in PMOs are direct parts of the 3D framework structure, **Figure 2.8.**

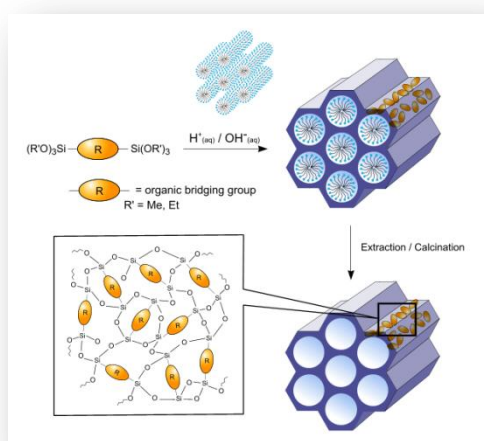
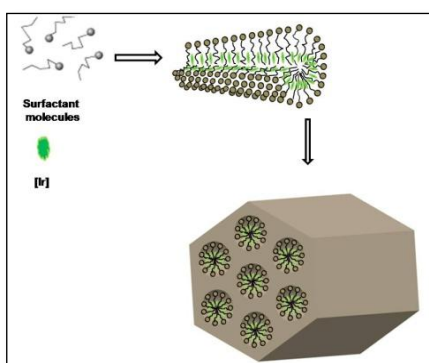


Figure 2.8. Periodic mesoporous organosilicas (PMOs).

Image copyright: <http://www.uni-giessen.de/cms/fbz/fb08/chemie/iaac/froeber/research/pmo>

The *co-condensation* technique is a simultaneous reaction of condensable inorganic silica species and silylated organic compounds (co-condensation is equal to one-pot synthesis), the co-condensation synthesis often caused the loss of ordering structure of mesoporous silica.

During this Thesis work we have investigated two methods, the impregnation technique, a post-synthesis method similar to a grafting, which consists in the soaking of mesoporous material into a dye solution, and a *one-pot-like* method, in



which new materials are formed by the co-condensation of a luminescent complex, with the inorganic silica precursor in the presence of template. Co-condensation properties are simultaneous functionalization and structure formation, homogeneous distribution of dyes into the porous matrix and controlled final stoichiometry similar to original solution

composition. **Figure left.**

The new materials described and discussed herein are obtained by a one-step procedure, similar to that developed by Zhou et al.¹⁴¹, co-assembling the neutral luminescent Iridium complex with a surfactant, which acts as structure-directing agent, and tetraethoxysilane (TEOS) as inorganic source. Moreover, because of the negligible solubility of Iridium(III) complex in H₂O, EtOH has been used as co-solvent in order to increase, at least slightly, the Iridium(III) complex solubility and make easier its inclusion within the hydrophobic regions of the surfactant during the template self-assembly process.

The silica-based luminescent materials prepared according to the above summarized procedure, with the general formula SiO₂([Ir]•CTAB) and SiO₂([Ir]•P123), have been structurally and photophysically investigated.

The differences induced by *i*) the nature of the reacted surfactant with respect to the neutral character of Iridium(III) complex *ii*) the resulting structural differences induced by the use of ethanol as co-solvent in the synthetic procedure and *iii*) the resulting structural differences induced by the introduction of the Iridium(III) complex luminescent complex will be discussed.

2.2.1 Co-condensation

The new ordered mesostructured materials, as mentioned above, were prepared by co-condensation of an appropriate inorganic source and the surfactant self-assembling species doped with an optically active compound, in particular the **chromophore is added to the reaction mixture**, which was stirred at room temperature for 5 h, then the SiO₂ precursor, TEOS, is added.

Mesostructured materials with a geometrically regular inorganic skeleton have been shown to be appropriate scaffolds for the confinement of dyes.^{142,143,144,145} The goal was to incorporate a highly luminescent species in a mesoporous material preserving, at the same time, the ordered porosity and the high surface area of the matrix.

Materials

Tetraethyl orthosilicate (TEOS, 98%), ammonium hydroxide (NH₄OH, 29 wt% NH₃ in water), poly(ethylene glycol)-block-poly(propylene glycol)-block-poly(ethylene glycol) (P123), hydrochloric acid (HCl 37%), and absolute ethanol (EtOH, 99.98%) were used as supplied by Sigma-Aldrich. Cetyltrimethyl ammonium bromide (CTAB, 99.8 wt%) was purchased from Alfa Aesar. Water was produced from a Milli-Q system. *fac*-Ir(ppy)₃, [Ir], was synthesized according to the procedure reported in the literature.¹⁴⁶

Synthesis

Preparation of mesostructured blank SiO₂(CTAB)

SiO₂(CTAB) was prepared using a procedure similar to the one described in the literature.¹⁴⁷ Molar composition: 1 TEOS: 0.3 CTAB: 3.8 NH₄OH: 153 H₂O: 17.1 EtOH. The template solution was prepared by dissolving 1.09 g (0.003 mol) of CTAB in 10ml (0.171 mol) of EtOH under magnetic stirring. Then, 27.5ml (1.53 mol) of H₂O and 2.49ml (0.038 mol) of NH₄OH were added to this solution. After 5 min, 2.21ml (0.01 mol) of TEOS was added under rapid stirring. The mixture was stirred for 3 days at room temperature, then filtered, washed with H₂O and dried at 343K overnight.

Preparation of mesostructured blank SiO₂(P123)

SiO₂(P123) was prepared adapting the procedure described in the literature.¹⁴⁸ Molar composition: 1 TEOS: 0.0174 P123: 6 HCl: 167 H₂O: 17.1 EtOH. 1 g (1.74·10⁻⁵ mol) of P123 was dissolved in 10ml (0.171 mol) of EtOH, under vigorous stirring at room temperature. Then, 30ml (1.67 mol) of H₂O and 1.83ml (0.060 mol) of HCl were added to the solution. Finally, 2.21ml (0.01 mol) of TEOS were added under stirring. The resulting mixture was aged at 373K for 24h, then filtered, washed with H₂O and dried at 333K for 12h.

Preparation of mesostructured hybrid, SiO₂([Ir]•CTAB)

Molar ratio: 1 TEOS: 0.3 CTAB: 3.8 NH₄OH: 153 H₂O: 17.1 EtOH: 0.0016 Iridium(III) complex. CTAB (1.09 g, 0.003 mol) was dissolved in 10ml (0.171 mol) of EtOH; Iridium(III) complex (0.01 g, 1.6·10⁻⁵ mol) was added to the reaction mixture, which was stirred at room temperature for 5 h. The obtained yellow suspension was filtered to remove the solid. Then 27.5ml (1.53 mol) of H₂O and 2.49ml (0.038 mol) of NH₄OH were added to the resulting solution. After 5 min, 2.21ml (0.01 mol) of TEOS were added under vigorous stirring. The mixture was stirred for 3 days at room temperature, then filtered, washed with H₂O and dried at 343 K overnight.

Preparation of SiO₂([Ir]•P123)

Molar composition: 1 TEOS: 0.0174 P123: 6 HCl: 167 H₂O: 17.1 EtOH: 0.0016 [Ir]. An ethanolic solution (10ml, 0.171 mol) of P123 (1 g, 1.74·10⁻⁵ mol) was obtained under vigorous stirring. Then, 0.01 g (1.6·10⁻⁵ mol) of Iridium(III) complex was added. The resulting mixture was stirred at room temperature for 5 h. Then the solid product was filtered and 30ml (1.67 mol) of H₂O and 1.83ml (0.060 mol) of HCl were added to the solution. Finally, 2.21ml (0.01 mol) of TEOS were added with stirring at room temperature. The mixture was aged at 373 K for 24 h, then filtered, washed with H₂O and dried at 333K for 12h.

Template extraction

The surfactant removal was performed using a chemical extraction with solvent. In particular, for the materials obtained with CTAB as template directing agent, EtOH (300 ml) and HCl (25 ml) were added to 1 g of the respective solids,

SiO₂(CTAB) and SiO₂([Ir]•CTAB). The mixtures were subsequently stirred for 6 h at reflux. The resulted inorganic scaffolds, named SiO₂(CTAB)* and SiO₂([Ir]•CTAB)* respectively, were dried at 343 K overnight.

For the other mesostructured materials, SiO₂(P123) and SiO₂([Ir]•P123), the removal of the neutral surfactant P123 was made by a chemical extraction using only EtOH (300 ml), which was added to 1 g of solid sample. The resulting mixture was stirred for 6h at reflux. The obtained solids, abbreviated in a similar way to the other extracted materials SiO₂(P123)* and SiO₂([Ir]•P123)* respectively, were dried at 343 K overnight.

2.2.2 EISA (Evaporation Induced Self-Assembly)

The film formation by EISA is a *chemical performance* that implies the coordinated interaction of the following phenomena:

- 1) Sol–gel chemistry (shape, size, hydrophilicity and connectivity of the inorganic or hybrid nano building blocks).
- 2) Self-assembly between template molecules, to form micelles, between micelles, to form extended liquid crystalline domains, and between micelles and inorganic or hybrid nano building blocks..
- 3) A “race towards order” in which the processes of gelling and order from phase separation compete.
- 4) Mass transport, which controls the homogeneity of the processes (and thus the mesostructure) along thickness.

One of the main parameters that govern the entire film-formation process is evaporation.

As soon as a layer of the initial sol is deposited on the substrate, evaporation of volatile components (ethanol, water, and hydrochloric acid) takes place at the air/film interface. The evaporation leads to the fast and progressive (10-30s) enrichment of the film in silica oligomers and template molecules. When the surfactant concentration has reached the equivalent of the critical micelle concentration (*cmc*) for the system, micelles start to form by hydrophobic segregation of alkyl chains. An organized mesostructure with respect to the physical-chemical properties of the surfactant molecule in the actual medium is eventually formed.

The evolution of an EISA system as a function of time (i.e., the kinetics of the system) leads to plot diagrams containing the main phases of film formation¹².

Figure 2.9

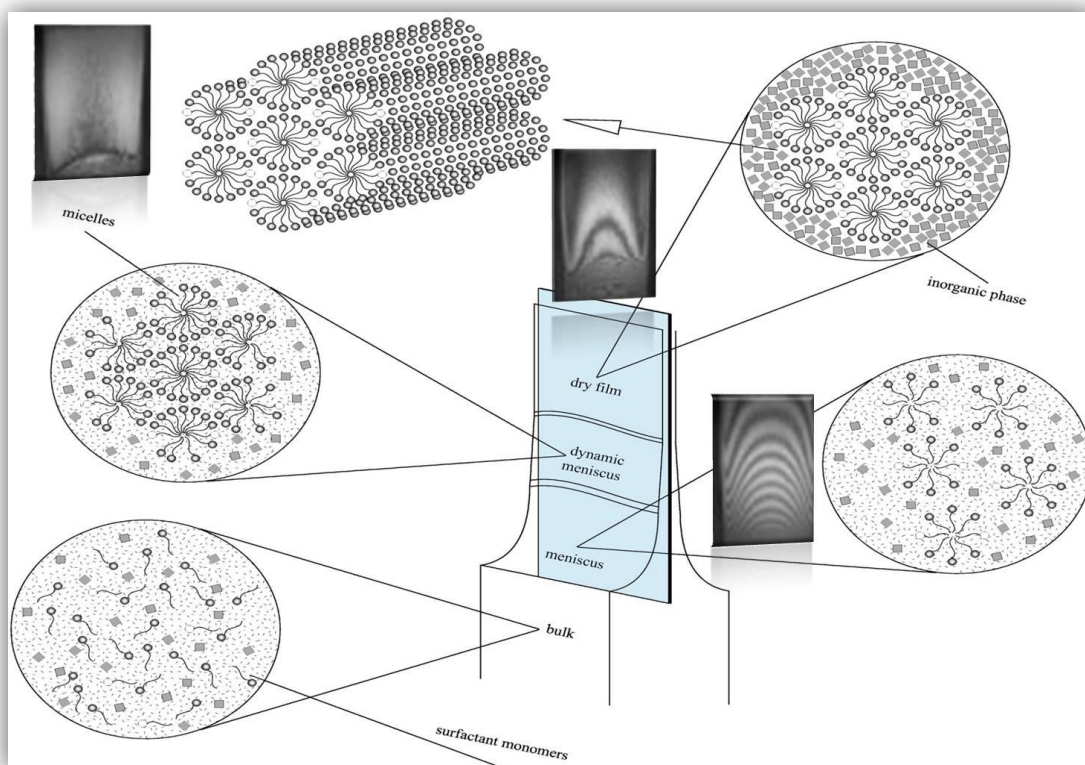


Figure 2.9. Formation of mesostructured thin film by dip-coating. *Step 1:* presence of isotropic initial sol in which the condensation is slowed. *Step 2:* evaporation proceeds and the micelles start to form above *cmc*. *Step 3:* evaporation is completed; the film is in equilibrium with environment and the mesostructure is fixed by relative humidity (RH) before inorganic condensation. *Step 4:* inorganic network is condensed; hybrid mesostructure is stabilized. Lee et al., 2006 *Phys. Fluids* 18, 052105

If the concentration of the inorganic and template species in the initial dilute solutions is low, no liquid crystalline species will be formed; even micelle formation is difficult under these conditions, because the critical micelle concentration (*cmc*) of the template in the solvent (often a mixture of low weight alcohols and lower water quantities) is relatively high.

When solvent evaporates, template self-assembly properties become evident, and aggregation processes (i.e., micellization) begin to take place.

When higher concentrations are reached, a liquid crystalline phase is formed, due to micelle aggregation. In the ideal case, micelles pile up in ordered structures and the inorganic building blocks locate themselves in the outside (polar) fraction of

the organic liquid crystal formed. A hybrid mesostructure (inorganic skeleton surrounding an organic liquid-crystalline phase) is thus formed. EISA can thus be described by competitive processes related to the kinetics of condensation versus the kinetic of organization, both influenced by the kinetics of diffusion of the volatile species. However, these processes are difficult to control and thus difficult to predict if they occur successively or simultaneously during drying.

In-situ SAXS experiments coupled with interferometry shed light into these complex assembly processes^{149,150,151,152}. In most of the cases, the mesostructure appears after the drying line (i.e., when practically all the solvent is evaporated and the film attains more or less its final thickness).

This multiplicity of mesophases upon mesostructure formation has been observed by insitu X-ray reflectometry experiments on silica/cationic surfactant films grown at the air–water interface¹⁵³. In the case of nonionic templates, the formation of a short-range order phase (often called a “wormlike phase”) precedes the formation of an organized and well-oriented product mesophase. This kind of “disorder-to-order” transition has also been observed in the initial stages of formation of thick films or xerogels¹⁵⁴. When a well-defined organization at the mesoscale is desired, the system has to be designed to separate phases and organize completely before the medium becomes rigid enough to “freeze” a disordered phase, or even to “freeze” before any phase separation, leading to a non-mesoporous, or poorly ordered film. In other words, the *race towards order* must be won¹⁵⁵.

If the thermodynamic differences between ordered or disordered mesophase are not significant at ambient temperature¹⁵⁶, the order phase can be formed if

- 1) the nucleation rate for an organized mesophase made upon the self-assembly of micelles and inorganic counterparts (i.e., the Nano Building Blocks of the hybrid mesophase) is high and
- 2) the medium is compliant enough to permit rearrangement of the nano building blocks.

Some clues of the condensation kinetics can be obtained by applying in-situ spectroscopic techniques, such as ATR-FTIR spectroscopy¹⁵⁷, FTIR ellipsometry¹⁵⁸, and IR synchrotron radiation.

2.2.2.1 Dip-coating

Mesoporous films are typically synthesized by evaporation-induced self-assembly (EISA), **Figure 9**, via dip-coating, using inorganic precursors such as alkoxides, organo-alkoxides or chlorides, and organic templating agents such as amphiphilic block copolymers^{159,160,161}. Mesoporous films show large surface areas up to 1000 m² g⁻¹, and pore volumes up to 1.3 cm³ g⁻¹¹⁶².

The thickness of the film is mainly determined by the rate of evaporation of the solvent and the viscosity of the solution. When the velocity of substrate and the viscosity of liquid aren't very high, the thickness of film can be obtained from Landau and Levich equation:

$$h = \frac{0.94(\eta U)^{2/3}}{\gamma_{LV}^{1/6}(\rho g)^{1/2}}$$

where U is the speed of extraction, η is the viscosity, γ_{LV} is the surface tension liquid-vapor. It is important to observe that for polymeric systems the thickness of film change with $U^{2/3}$. This equation assumes constant viscosity and Newtonian behavior, without effects of evaporation. Landau and Levich equation is effective for sol prepared in acid catalysis¹².



Figure 2.10. Dip-coater with temperature and humidity control panels.

In this thesis work, we introduced a Iridium(III) complex as light emitting guest species into a mesoporous silica film acting as host matrix. The synthesis of the luminescent material has been performed by a co-condensation approach, similar to the one described above for the powders.

The instrument used was a dip-coater fabricated by workers of University of Calabria spin-off, CalTec s.r.l.(Calabria Liquid Crystals Technology) **Figure 2.10**.

Materials

Pluronic F127 (OH(CH₂-CH₂O)₁₀₆(CHCH₃-CH₂O)₇₀(CH₂CH₂O)₁₀₆H), tetraethyl orthosilicate 99% (TEOS), hydrochloric acid (HCl 37%), and absolute ethanol (EtOH, 99.98%) were used as supplied by Sigma-Aldrich. Water was produced from a Milli-Q system. *fac*-Ir(ppy)₃, [Ir], was synthesized according to the procedure reported in the literature.³⁵ Quartz slides, with area=3cm², were employed as the substrates. The slides were accurately washed by distilled water, ethanol and acetone before using.

Preparation of silica sol

A first solution, the template solution, was prepared by dissolving 1.3 g of Pluronic F127 and 0.01 g ($1.6 \cdot 10^{-5}$ mol) of Iridium(III) complex in 15 ml of EtOH and 1.5 ml of HCl acid aqueous solution (5.7×10^{-2} M). The resulting mixture was stirred at room temperature for 5 h. A stock solution was prepared by adding (in the following order) ethanol, TEOS, water, and HCl in the molar ratios TEOS:EtOH:H₂O:HCl = 1:2.78:1.04:1.43x10⁻². The sol was left to react under stirring 75 min at room temperature. The final sol was obtained by adding 7.7 ml of the stock sol to the solution containing the block copolymer. The final molar ratios were TEOS:EtOH:H₂O:HCl:PluronicF127:[Ir]=1:16.3:5.4:1.88x10⁻²:5x10⁻³:0.0016 [Ir]. The sol was stirred at room temperature for 15 min and immediately used for film deposition.

Preparation of silica films

The films were deposited on the substrates via dip-coating at room temperature. The film depositions were performed at 24% relative humidity (RH), at the withdrawal speed of 15cm min⁻¹. After the deposition, the films were dried at 60°C for 12h. We obtained two kind of materials: a mesostructured SiO₂([Ir]•F127) and a mesostructured blank SiO₂(F127), then calcined in air for 60min at 350°C. At the moment silica films are subject to further improvements and investigations.

2.3 Mesoporous characterization

Low angle X-ray diffraction (XRD) measurements were performed in the 2θ range of 1.0° - 10.0° with a Philips 1730/10 diffractometer using Cu K α radiation ($\lambda = 1.5416 \text{ \AA}$) at 40 kV and 200 mA and at-a-step width of 0.005° .

Nitrogen sorption isotherms were measured at 77 K on a Micromeritics ASAP 2010 porosimeter. The materials were outgassed for 12 h under vacuum at 423 K before the measurements.

Specific surface areas were calculated by the Brunauer-Emmett-Teller (BET) method and pore sizes by the Barrett-Joyner-Halenda (BJH) methods.^{163,164}

Scanning electron microscopy images (SEM) were obtained with FEI FP 2353/OX. The thermogravimetric analysis (TGA) was carried out between 298 K and 1093 K under an air flow and at a heating rate of 10 K/min in a Perkin Elmer thermobalance.

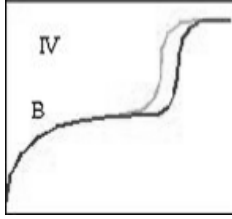
Transmission electron microscopy (TEM) images of mesoporous materials were obtained in the bright field mode on a JEOL 200C9 microscope equipped with a tungsten cathode operating at 200 kV. Mesoporous powders were deposited on a carbon-coated copper grid. Performed in the Laboratory of Materials Science and Nanotechnologies, CR-INSTM, University of Sassari.

Steady-state emission spectra were recorded on a Horiba Jobin Yvon Fluorolog 3 spectrofluorimeter, equipped with a Hamamatsu R-928 photomultiplier tube.

The procedure involves in mesoporous materials characterization, are, primarily, X-Ray powder Diffraction (XRD) which should be carried out at wide and low angles. The XRD powder d spacings of well-prepared MCM-41 can be indexed on a hexagonal and cubic lattice, respectively. XRD combined with other techniques, such as HRTEM, electron diffraction, and lattice images, are key methods for the characterization of these materials and identification of the phase obtained, i.e. hexagonal (MCM-41).

Adsorption of molecules has been widely used to map the pore size distribution of mesoporous solids. In this sense, the physisorption of gases such as N₂, O₂, and Ar have been used to characterize the porosity of M41S samples and more specifically MCM-41.

When adsorption was carried out on a MCM-41 sample, it was found that the



isotherm for N₂ is type IV in the IUPAC classification, see **figure on the left**, and no adsorption-desorption hysteresis

was found at the boiling temperature of N₂ (77.4 K). In the case of Ar and O₂ the isotherm is also of type IV, but they exhibit well-defined hysteresis loops, figure gray line. These results can be attributed to capillary condensation taking place within a narrow range of tubular pores confirming the high degree of pore uniformity. Owing to the success of N₂ and Ar adsorption in terms of the determination of the pore diameter, one can combine the XRD results together with the pore size determined from gas adsorption experiments to find the thickness of the wall.

Adsorption studies, besides their convenience for measuring the textural properties of these materials, can also be used to study the interaction of molecules with the walls of the pores, a feature of particular importance from the point of view of the diffusion and catalytic properties of the material. In this sense, adsorption studies of polar and non-polar molecules can be quite useful for measuring the hydrophobic and hydrophilic properties of M41S mesoporous materials.

By analyzing the multilayer physisorption and capillary condensation of a gas within the pores, a plot of the adsorbed volume of gas versus the partial pressure P/P_0 of gas is obtained. The mono and multilayer physisorption of the gas observed at low P/P_0 can be plotted by the Brunauer-Emmett-Teller (BET) equation:

$$\frac{P}{n(P_0 - P)} = \frac{1}{n_m C} + \frac{C - 1}{n_m C} \frac{P}{P_0}$$

It allows the determination of the surface area, with n_m being the number of molecules needed to cover the accessible surface with a monolayer of molecules, n , the number of molecules adsorbed at the partial pressure P/P_0 , and C , a parameter characteristic of the net heat of adsorption of the molecule at the surface^{165,166}. The gas uptake observed at higher P/P_0 values, defined as capillary condensation, is used for the determination of the PSD between 2 and 50 nm via the Kelvin equation

$$RT \ln \left(\frac{P}{P_0} \right) = -\gamma V_L \frac{G}{r_p}$$

that describes the condition of appearance of the capillary condensation at a given value of P/P_0 , with γ , the condensed liquid surface tension, V_L the molar volume of the liquid adsorbate, r_p the radius of the pore, and G , a geometrical factor characteristic of the liquid-air meniscus curvature (BJH model)¹⁶⁷.

Another technique is differential scanning calorimetry (DSC) in which the difference in the amount of heat required to increase the temperature of a sample and reference are measured as a function of temperature. The main application of DSC is in studying phase transitions, such as melting, glass transitions, or exothermic decompositions. These transitions involve energy changes or heat capacity changes that can be detected by DSC with great sensitivity. This curve can be used to calculate enthalpies of transitions. This is done by integrating the peak corresponding to a given transition.

Thermogravimetric Analysis (TGA) is a type of testing that is performed on samples to determine changes in weight in relation to change in temperature. Such analysis relies on a high degree of precision in three measurements: weight, temperature, and temperature change. TGA is commonly employed in research and testing to determine characteristics of materials such as polymers, to determine degradation temperatures, absorbed moisture content of materials, the level of inorganic and organic components in materials, decomposition points of explosives, and solvent residues. For mesoporous materials, TGA allows to know the amount of surfactant or other organic species, present into the structure and water absorbed from the sample¹⁶⁸.

The emission quantum yields (Φ) of the samples were obtained by means of a 102 mm diameter integrating sphere coated with Spectralon[®] and mounted in the optical path of the spectrofluorimeter using a 450 W Xenon lamp as excitation source, coupled with a double-grating monochromator for selecting wavelengths. Φ is a ratio of “number of photons emitted” to “number of photons absorbed”.

The number of photons absorbed is calculated by monitoring the scattered excitation peak firstly with the blank sample in the sphere (L_a) and secondly with the sample in the sphere (L_c). The differences in peak intensity between these two measurements is caused by sample absorption and thus the number of absorbed photons can be calculated as the differences of the integrated curves (L_a-L_c).

The number of photons emitted is calculated as the difference of the integrated luminescence of the sample (E_c) and of the blank (E_a) and therefore ($E_c - E_a$). As a result, $\Phi = (E_c - E_a) / (L_a - L_c)$. The experimental uncertainty on the Φ is 5%. In particular mesostructured $\text{SiO}_2(\text{CTAB})$ and $\text{SiO}_2(\text{P123})$ were used as blank samples for the determination of Φ of $\text{SiO}_2([\text{Ir}] \cdot \text{CTAB})$ and $\text{SiO}_2([\text{Ir}] \cdot \text{P123})$, respectively.

Time-resolved measurements were performed using the time-correlated single-photon counting (TCSPC) option on the Fluorolog 3. NanoLED at 370 nm, fwhm < 200 ps, was used to excite the sample. Excitation sources were mounted directly on the sample chamber at 90° to a single-grating emission monochromator (2.1 nm mm^{-1} dispersion; 1200 grooves mm^{-1}) and collected with a TBX-04-D single-photon-counting detector. The photons collected at the detector were correlated by a time-to-amplitude converter (TAC) to the excitation pulse. Signals were collected using an IBH Data Station Hub photon counting module and data analysis was performed using the commercially available DAS6 software (HORIBA Jobin Yvon IBH). Goodness of fit was assessed by minimizing the reduced Chi squared function (χ^2) and visual inspection of the weighted residuals. The average lifetimes were calculated as $\langle \tau \rangle = \sum_i (A_i \tau_i) / \sum_i A_i$.

2.3.1 Photoluminescence properties

The chemistry of cyclometalated Iridium(III) complexes is a current topic of investigations because they display unique photophysical properties such as good photo- and thermal stability, high phosphorescence quantum efficiencies, relatively short lifetimes and simple colour tuning through ligand structure and control, a set of key features for molecular-based light emitting devices applications.^{169,170,171,172,173}

Since several dyes undergo luminescence quenching phenomena at relatively high concentrations, preventing advantageous applications, a possible way to overcome this drawback is given by the mesostructured materials presented previously. These materials present a well-defined organic-inorganic phase segregation at the nanometer scale which may effectively prevent the aggregation and the related luminescence quenching phenomena. Moreover, it is worth recalling further excellent advantages, such as the increased mechanical stability and the shielding

against chemical, thermal or photochemical degradation of the incorporated dye, which are carried out by the scaffolds itself.

2.3.1.1 Emission spectra, phosphorescence quantum yield and time-resolved luminescence

For Iridium(III) complexes luminescence, the quantum yield in the solid state is a function of aggregation. Aggregate formation often quenches light emission limiting the development of photoluminescent materials that exhibit strong solid-state emission properties.¹⁷⁴ Nevertheless in some cases it has been demonstrated that luminescence quantum yield of Iridium(III) complexes in solid states such as doped polymer films or powder state with suitable supramolecular organization of the chromophores is higher than that in fluidic solutions.¹⁷⁵ Specifically in the case of [Ir] it has been shown that its photoluminescence efficiency can vary from 1% in neat film to 40% in solution reaching a value of 90% in highly dispersed polymeric matrix.¹⁷⁶

In order to investigate the photoluminescence properties of the new synthesized mesostructured materials a full photophysical investigation including emission spectra, phosphorescence quantum yield and time-resolved luminescence were performed for comparison on the two hybrid solids and on the pristine [Ir] powder. The full photophysical results compared to the photophysical properties of [Ir] complex in solution^{176,177} are summarized in **Table 2.1**.

Table 2.1 Photoluminescence properties

Materials	λ_{\max} [nm]	Φ	$\tau_{\text{Ph}}/(A_i)$ [ns]	τ_{rad} [ns]	$\langle\tau\rangle$ [ns]	Φ_{calc} [ns]
[Ir] ^a	515	0.73	1090	1500	-	-
[Ir] ^b	-	0.91	1200	1300	-	-
[Ir] ^c	534	0.012	$\tau_1 = 0.1$ (49%) $\tau_2 = 38$ (50 %)	-	19	~1.4%
SiO ₂ ([Ir]•CTAB)	509	0.3	$\tau_1 = 576$ (27%) $\tau_2 = 1077$ (72%)	-	931	~72%
SiO ₂ ([Ir]•P123)	515	0.04	$\tau_1 = 527$ (25%) $\tau_2 = 1120$ (76%)	-	983	~75%
SiO ₂ ([Ir]•F127)	517	-	$\tau_1 = 19$ (2%) $\tau_2 = 1254$ (80%) $\tau_3 = 402$ (18%)	-	1076	~83%

^a Data concerning [Ir] in deoxygenated toluene solution taken from ref. 176,177. ^b Data concerning [Ir] in polystyrene matrix (1 wt%) taken from ref. 176. ^c [Ir] pristine powder.

In **figure 2.11** are reported the emission spectra of the mesostructured powders $\text{SiO}_2([\text{Ir}] \cdot \text{CTAB})$ and $\text{SiO}_2([\text{Ir}] \cdot \text{P123})$ compared to the emission spectra of the $[\text{Ir}]$ powder. With reference to the emission spectra of both $\text{SiO}_2([\text{Ir}] \cdot \text{CTAB})$ and $\text{SiO}_2([\text{Ir}] \cdot \text{P123})$ no red shift of the emission maxima is observed on moving from solution to the two different mesostructured powders whereas a substantial red shift is observed for pristine $[\text{Ir}]$ solid. In **figure 2.12** are reported the emission spectra of the mesostructured films $\text{SiO}_2([\text{Ir}] \cdot \text{F127})$ and of the powder $\text{SiO}_2([\text{Ir}] \cdot \text{P123})$ compared with the emission spectra of the $[\text{Ir}]$ powder. With reference to the emission spectra of $\text{SiO}_2([\text{Ir}] \cdot \text{P123})$ and $\text{SiO}_2([\text{Ir}] \cdot \text{F127})$, no red shift of the emission maxima is observed on moving from solution to the two different mesostructured powders whereas a substantial red shift is observed for pristine $[\text{Ir}]$ solid.

Since a significant red shift of the emission maxima is expected for aggregation states which favour the occurrence of a high degree of interchromophore contacts,¹⁷⁸ the observed spectral features seem to indicate *i*) a substantial absence of strictly interacting Iridium(III) moieties in the mesoporous powders as a result of a very good dispersion of the host in the matrixes and *ii*) the existence of a high degree of interchromophore contact in the pristine solid.

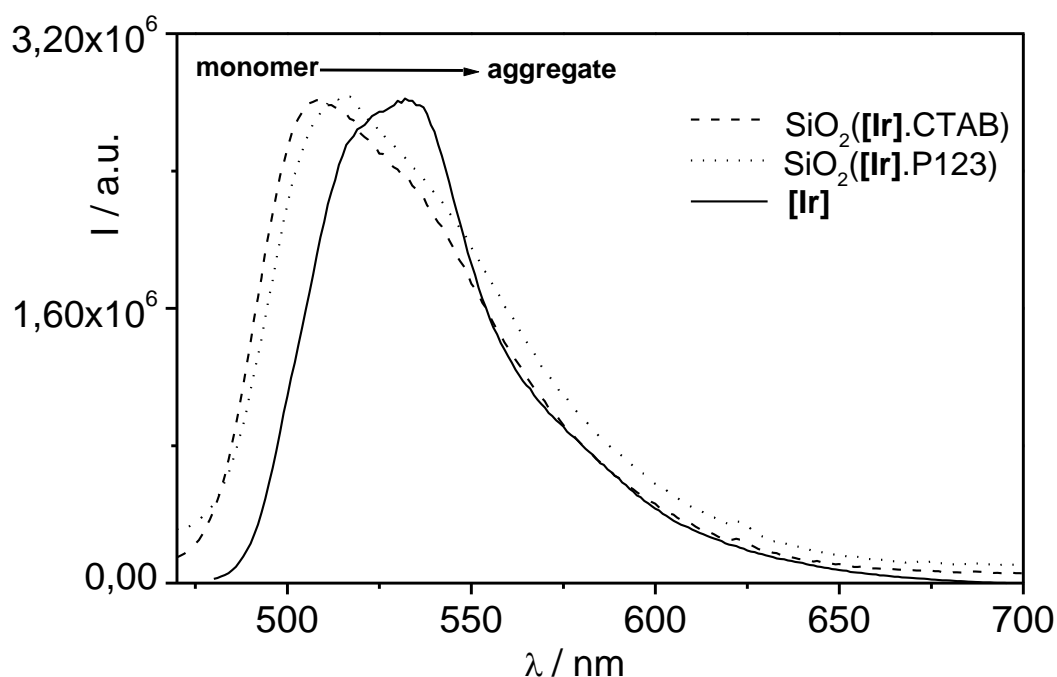


Figure 2.11. Emission spectra of $\text{SiO}_2([\text{Ir}] \cdot \text{CTAB})$ (dash line), $\text{SiO}_2([\text{Ir}] \cdot \text{P123})$ (dot line) and emission spectra of $[\text{Ir}]$ pristine powder (solid line).

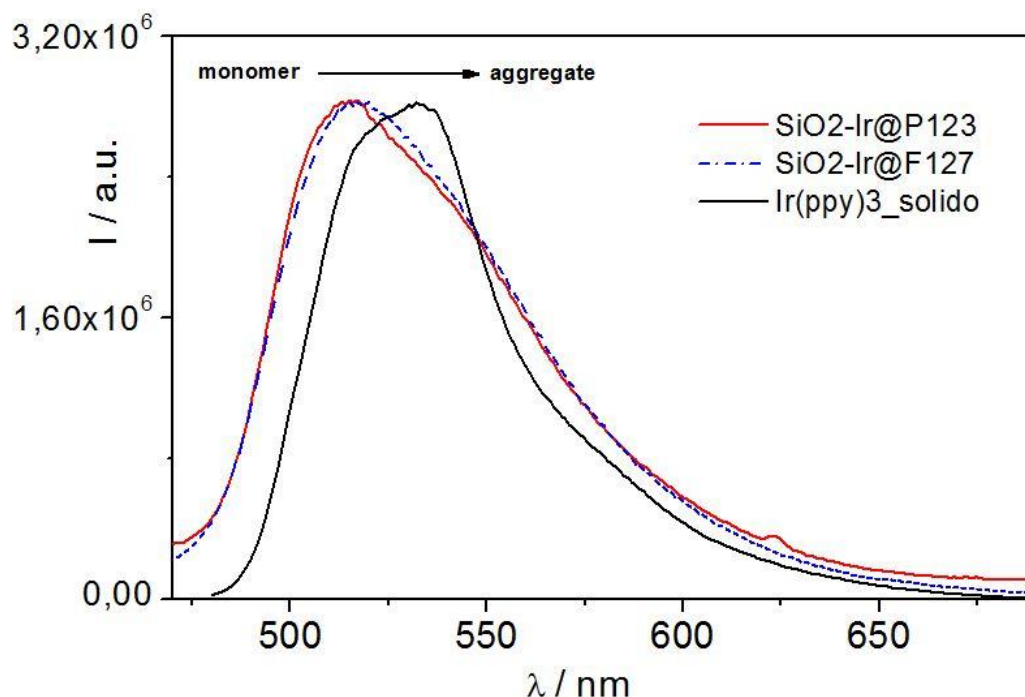


Figure 2.3 Emission spectra of SiO₂([Ir]•P123) (solid red line), SiO₂([Ir]•F127) (dash blue line) and emission spectra of [Ir] pristine powder (solid black line).

Regarding phosphorescence quantum efficiency the [Ir] solid shows a considerably reduced phosphorescence quantum yield with respect both to solutions and dispersed polymeric matrix (**Table 2.1**).

Moreover its luminescence decay turned out to be considerably fast and non-exponential thus indicating the presence of additional non-radiative decay channels caused by aggregation in the solid state.

Differently from the [Ir] solid, SiO₂([Ir]•CTAB), SiO₂([Ir]•P123) and SiO₂([Ir]•F127) show much longer luminescence lifetimes, even if still non-exponential. In particular both powder solids show a longer lifetime component of ~ 1100 ns, which account for most of the signal (75%) and a shorter one of ~ 500 ns accounting for the 25% of the total decay; mesoporous film shows a longer lifetime component of ~ 1254 ns, which account for most of the signal (80%) and two shorter ones of ~ 402 ns and ~ 19 ns accounting for the 18% and 2% of the total decay respectively.

The longer luminescent lifetime component is comparable with that observed for [Ir] highly dispersed in a polymeric rigid matrix (**Table 2.1**) which is usually associated with the lifetime of the isolated rigid molecule. Therefore this component could be attributed to a large fraction of non-interacting Iridium(III)

moieties reasonably included in the interior of the micelle cores where the chromophore is preferentially shielded from aggregation and consequently from luminescence quenching phenomena.

Furthermore the faster lifetime component may result from a fraction of Iridium(III) chromophore whose luminescence can be quenched through exciton migration quenching phenomena between closely packed Iridium(III) chromophores and/or iridium chromophores and impurity traps possibly present in the materials.

Phosphorescence quantum yields of $\text{SiO}_2([\text{Ir}]\cdot\text{CTAB})$, $\text{SiO}_2([\text{Ir}]\cdot\text{P123})$ and $\text{SiO}_2([\text{Ir}]\cdot\text{F127})$ mesostructured solids were determined following the procedure described in the experimental section. Different results were obtained for the two powders (30% and 4% respectively) despite the very similar photophysical data deriving from both steady state and time-resolved luminescence measurements. On the other hand, due to the small mesostructured film thickness and since there is a limit of instrument resolution, the phosphorescence quantum yields of $\text{SiO}_2([\text{Ir}]\cdot\text{F127})$ cannot be reported. Moreover these values disagree significantly with respect to the value reported for the [Ir] complex dispersed in polystyrene matrix (**Table 2.1**) despite the similarity of the lifetimes values.

Therefore our measured phosphorescence quantum yields should be affected by instrumental artefacts likely arising from important light scattering phenomena typical of such materials and affecting substantially the calculated values of absorbed photons. Nevertheless the phosphorescence quantum yields (Φ_p) were roughly estimated. When only one type of emitting species is present in the sample, the phosphorescence lifetime (τ_p) and Φ_p values are related to the radiative lifetime (τ_r) of the emissive state as:

$$\phi_p = \phi_{isc} \left(\frac{\tau_p}{\tau_r} \right)$$

where Φ_{isc} is the intersystem crossing quantum yield and it is assumed as unitary value.¹⁷⁷

Considering the value reported in the literature for [Ir] dispersed in a polystyrene matrix as radiative lifetime and the medium values $\langle\tau\rangle$ calculated from experimental data as phosphorescence lifetime, the phosphorescence quantum yields obtained for $\text{SiO}_2([\text{Ir}]\cdot\text{CTAB})$ and $\text{SiO}_2([\text{Ir}]\cdot\text{P123})$ are 72% and 75%

respectively, for mesoporous silica film $\text{SiO}_2([\text{Ir}] \cdot \text{F127})$ the phosphorescence quantum yields obtained is 83%. Moreover, the phosphorescence quantum yield of the [Ir] pristine solid was calculated analogously obtaining a comparable result with respect to that measured (**Table 2.1**).

The calculated luminescence quantum yield values suggest that the experimental approach (technique, set-up) adopted for their determination suffers from a severe limitation arising from the not negligible scattering phenomena displayed by the investigated materials. However, the calculated values seem to be in agreement with both XRD and porosimetric results, showing the [Ir] complexes mainly included in the interior of the micellar aggregates.

2.3.2 Powder X-ray diffraction (XRD)

XRD patterns of all the synthesized mesostructured materials (hybrids and blanks) were recorded (**Figure 2.13**).

Both $\text{SiO}_2(\text{CTAB})$ and $\text{SiO}_2([\text{Ir}] \cdot \text{CTAB})$ exhibit XRD patterns similar to the ones reported in the literature for analogous systems.²⁸ In particular, the patterns consist at small angle of three relatively broad reflections indexed as [100], [110] and [200] characteristic of a hexagonal lattice.

The similar interplanar distances d_{100} , and consequently similar hexagonal lattice constants a (**Figure 2.13a**), indicate that the presence of the [Ir] did not affect the self-assembly process during mesophase formation keeping the mesostructure substantially unchanged. This phenomenon can be explained by the introduction of the chromophore in between CTAB surfactant hydrophobic tails in a periodical manner within a mesostructured channel.¹⁷⁹ However, the decrease of the intensity of the diffraction peaks in the case of the hybrid material $\text{SiO}_2([\text{Ir}] \cdot \text{CTAB})$ may be indicative of a more disorganized material compared with the blank one. In addition both mesostructured materials containing CTAB show shrinkage of the d spacings typically observed when, instead of pure H_2O , a $\text{H}_2\text{O}/\text{EtOH}$ mixture is employed in the synthesis.²⁸

The XRD patterns of $\text{SiO}_2(\text{P123})$ and $\text{SiO}_2([\text{Ir}]\cdot\text{P123})$ samples (**Figure 2.13b**) consist of four peaks that can be indexed as [100], [110], [200] and [210] associated with a hexagonal symmetry. These patterns are similar to the ones exhibited by the analogues P123-template materials reported in the literature,²⁹ with an expected shrinkage of the cell parameters because of the use of EtOH as co-solvent.²⁸ Nevertheless the $\text{SiO}_2([\text{Ir}]\cdot\text{P123})$ sample shows an increase of the interplanar distance and hexagonal unit cell length with respect to $\text{SiO}_2(\text{P123})$ blank (**Figure 2.13 b**).

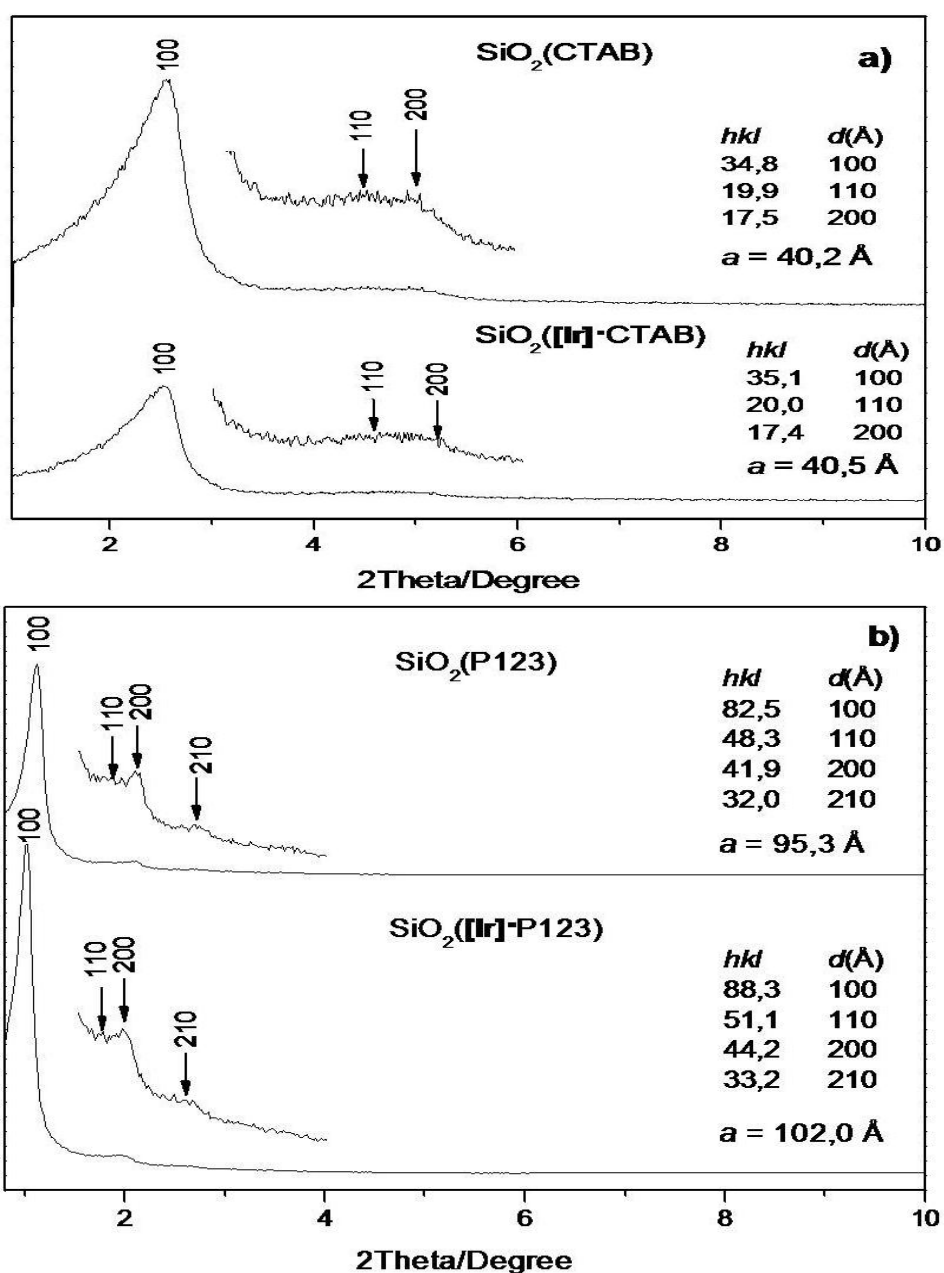


Figure 2.13. XRD patterns of (a) $\text{SiO}_2(\text{CTAB})$ up and $\text{SiO}_2([\text{Ir}]\cdot\text{CTAB})$ down; (b) up- $\text{SiO}_2(\text{P123})$ and down - $\text{SiO}_2([\text{Ir}]\cdot\text{P123})$.

This may be indicative of the placement of [Ir] complex in the interior of the micellar aggregates, which consequently expands the micelles size.³⁰ Furthermore, on the contrary to the systems containing CTAB surfactant, the inclusion of the Iridium(III) complexes seems to enhance slightly the order parameter of the hybrid material SiO₂([Ir]•P123), as the increase of the intensity of the reflection peaks indicate when the patterns are compared with the blank SiO₂(P123) one.

No significant changes were observed for the XRD patterns recorded several weeks later for both CTAB and P123-template materials stored in air this behaviour indicating a very stable structure.

While an X-ray diffraction method provides information about the structure of silica mesoporous materials, porosimetry can give the size distribution of pores in these materials.

2.3.3 N₂ sorption

Many techniques have been developed to characterize the porous structure of this kind of solids. Among them the nitrogen adsorption technique is the most popular one that can obtain the data on total pore volume, the BET surface area and the pore size distribution.

According to the International Union of Pure and Applied Chemistry (IUPAC), the majority of adsorption-desorption isotherms may be classified into six types¹⁸⁰ as shown in **Figure 2.14**.

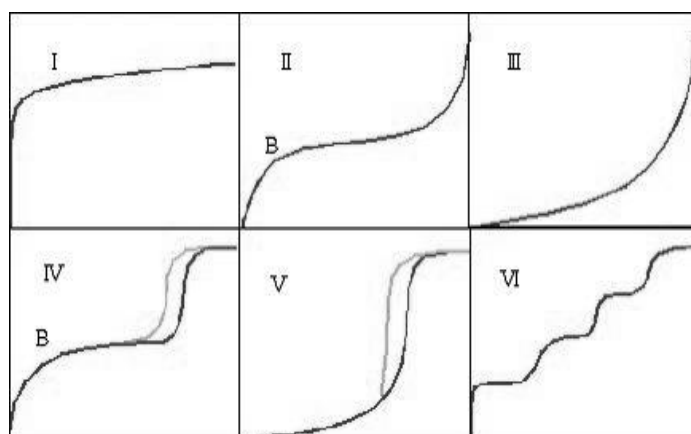


Figure 2.14. The six IUPAC standard adsorption isotherms.

The Type I isotherm is typical of microporous solids and chemisorption isotherms. Types II and III give adsorption isotherm on macroporous adsorbent with strong and weak affinities, respectively. Type IV and type V are typical of mesoporous adsorbents strong and weak affinities, respectively. For lower temperatures they show adsorption hysteresis, generated by the capillary

condensation of the adsorbate in the mesopores of the solid. Finally, the rare type VI step-like isotherm is shown by nitrogen adsorbed on special carbon.

Normally, in the adsorption-desorption isotherms, the desorption isotherms do not retrace the adsorption ones but rather lie above them over a range of relative pressure, which form a hysteresis loop before eventually rejoining the adsorption isotherms.

Hysteresis appearing in the multilayer range of physisorption isotherms is usually associated with capillary condensation in mesoporous structures.

The specific surface areas (S_{BET}), pore diameters (d_p) and pore volume (V_p) of all prepared materials were calculated by the BET method and BJH model, respectively (**Table 2.2**).

Materials	$S_{BET}^a/m^2 g^{-1}$	d_p^b/nm	$V_p/cm^3 g^{-1}$
$SiO_2(CTAB)^*$	1240	3.1	0.92
$SiO_2([Ir] \cdot CTAB)^*$	1002	3.4	0.98
$SiO_2(P123)^*$	794	3.6	0.68
$SiO_2([Ir] \cdot P123)^*$	738	4.0	0.79

Table 2.2 Physicochemical parameters of mesoporous silica materials derived from Nitrogen sorption measurements; ^a Determined using the BET. ^b Determined by the BJH algorithm using the absorption branch.

The adsorption/desorption isotherms of $SiO_2(CTAB)^*$, $SiO_2([Ir] \cdot CTAB)^*$, $SiO_2(P123)^*$ and $SiO_2([Ir] \cdot P123)^*$ were shown in **Figure 2.15**.

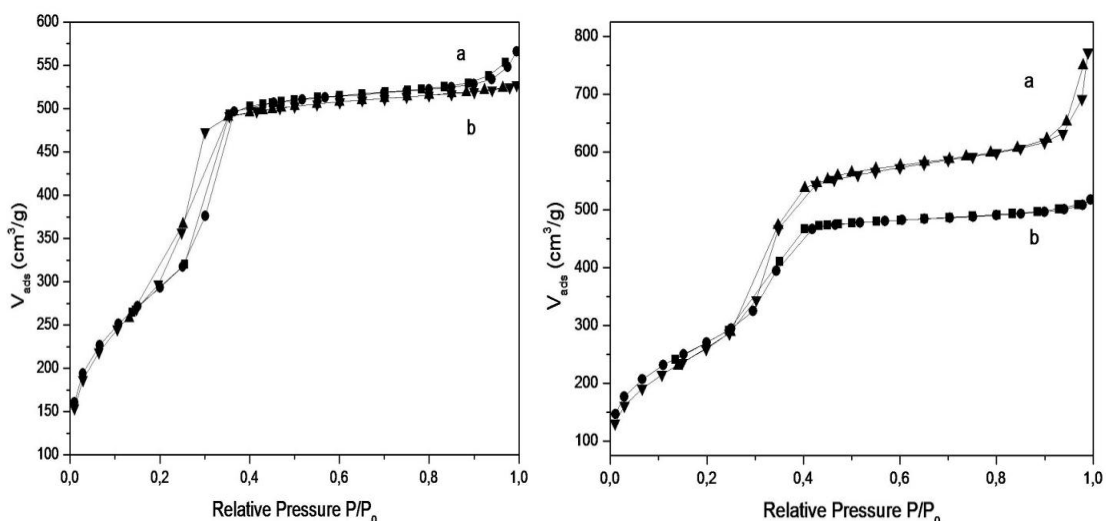


Figure 2.15. Nitrogen adsorption and desorption isotherms for (a) $SiO_2(CTAB)^*$ and (b) $SiO_2([Ir] \cdot CTAB)^*$ on the left and for (a) $SiO_2(P123)^*$ and (b) $SiO_2([Ir] \cdot P123)^*$ on the right.

The isotherms of all the extracted samples are type IV according to the IUPAC classification, and typical of mesoporous materials with uniform size distribution.

The porosimetric values d_p , S_{BET} , and V_p determined for all the extracted samples are coherent with that obtained for analogous synthesized materials.^{28,29} Nevertheless the values measured for $\text{SiO}_2([\text{Ir}] \cdot \text{CTAB})^*$ and $\text{SiO}_2([\text{Ir}] \cdot \text{P123})^*$ samples, including d_p and V_p , are slightly increased with respect to the corresponding blank ones. Therefore, it is reasonable to assume that the self-inclusion of $[\text{Ir}]$ inside the micelles during the co-assembly process affect their dimensions, thus leading to an enlargement of the resulted pore size and pore volume values.

2.3.4 Scanning electron microscopy (SEM)

The surface morphology of the studied powders and films was investigated by SEM.

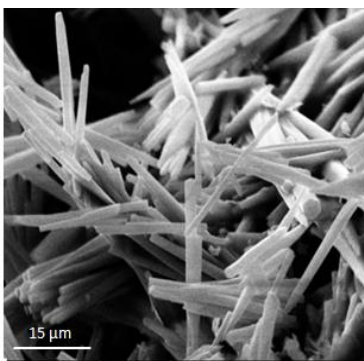


Figure 2.16 shows representative SEM micrographs of the $[\text{Ir}]$ solid. In the solid state this luminescent complex forms long fibres with a hexagonal section and medium diameter of 2-5 μm.

Figure 2.16. Representative SEM image of $[\text{Ir}]$.

Figure 2.17 shows SEM micrographs of all mesostructured powders materials synthesised.

The solids exhibit very different morphologies among them. Syntheses using H_2O and EtOH as co-solvent permit spherical particles with ordered mesopores to be obtained. In fact, $\text{SiO}_2(\text{CTAB})$ as $\text{SiO}_2([\text{Ir}] \cdot \text{CTAB})$ (**Fig.17 a,b**) consists of medium-sized spherical particles of 800 nm and a homogeneous size distribution. $\text{SiO}_2(\text{P123})$ as $\text{SiO}_2([\text{Ir}] \cdot \text{P123})$ (**Fig.17 c,d**) samples exhibit larger and much more monolithic aggregates with a minimum dimension of 5-8 μm.

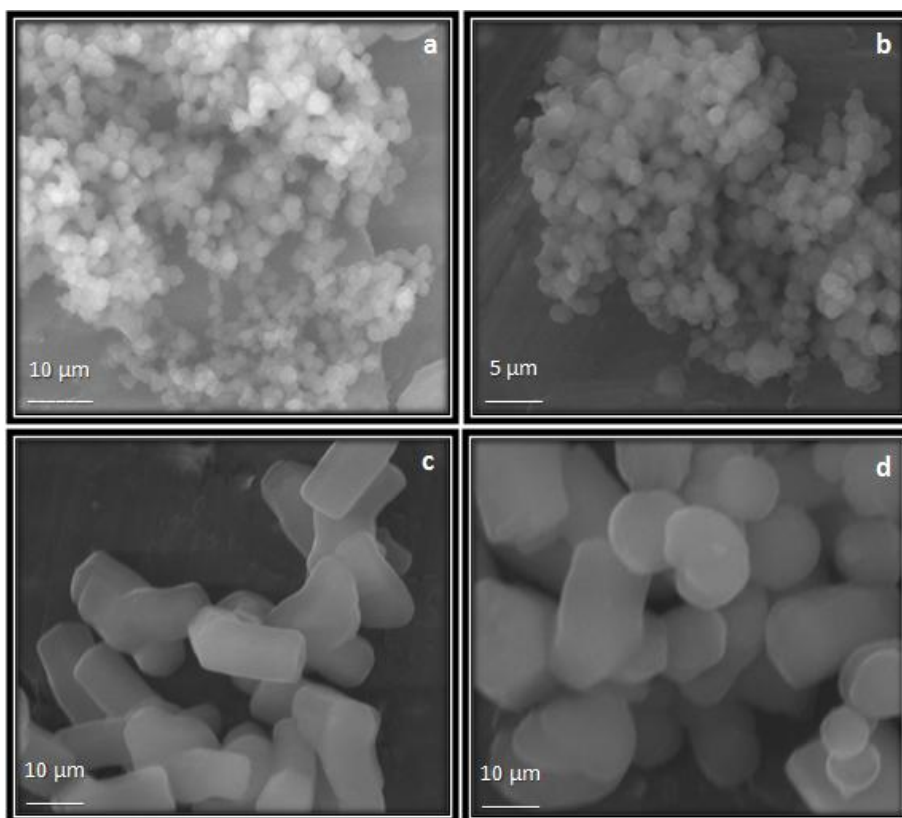


Figure 2.17. Representative SEM image of $\text{SiO}_2(\text{CTAB})$ (a), $\text{SiO}_2([\text{Ir}]\cdot\text{CTAB})$ (b), $\text{SiO}_2(\text{P123})$ (c) and $\text{SiO}_2([\text{Ir}]\cdot\text{P123})$ (d).

2.3.5 Transmission Electron Microscopy (TEM)

Figure 2.18 shows representative direct image of the deposited film. The snapshot suggests that the mesostructure is a distorted cubic. This periodicity is compatible with an orthorhombic $Fmmm$ space group, **Figure 2.19**.

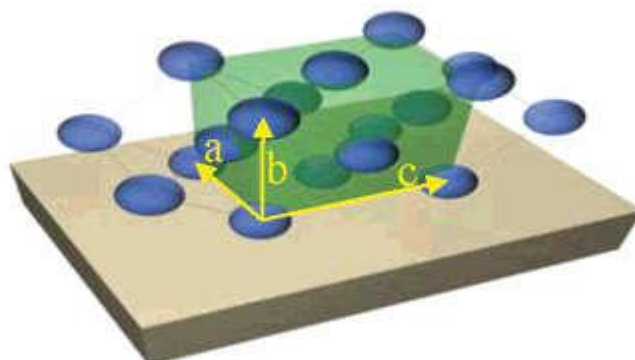


Figure 2.19. $Fmmm$ mesophase.

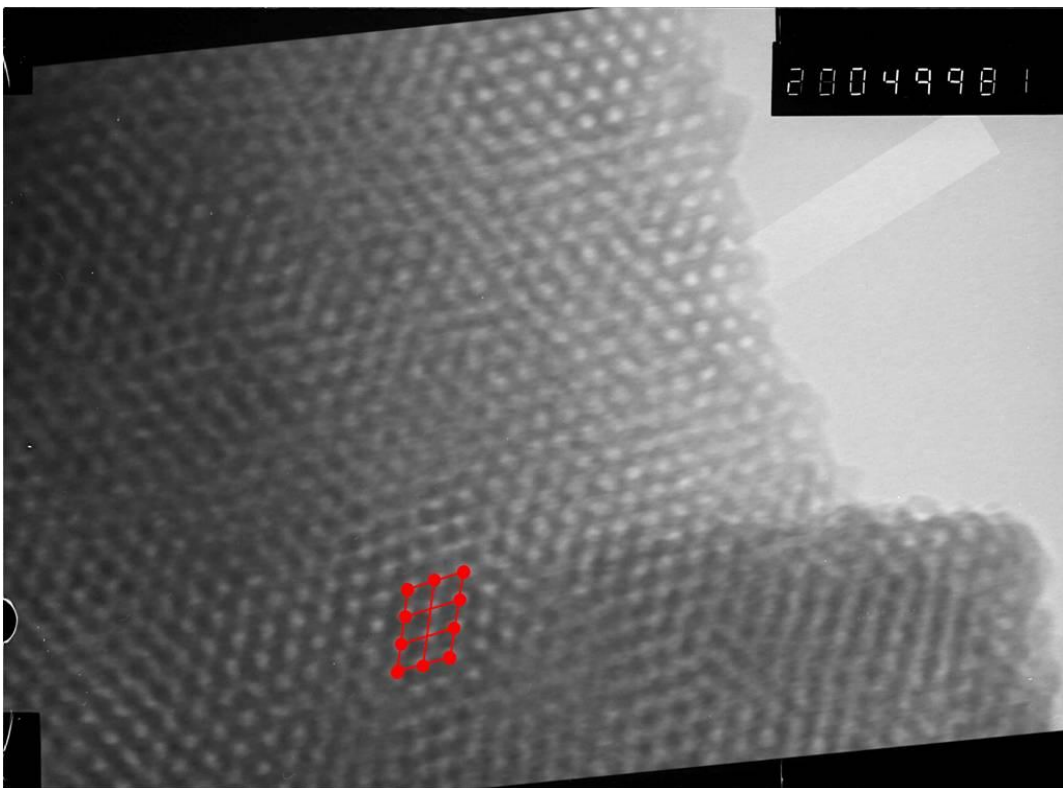
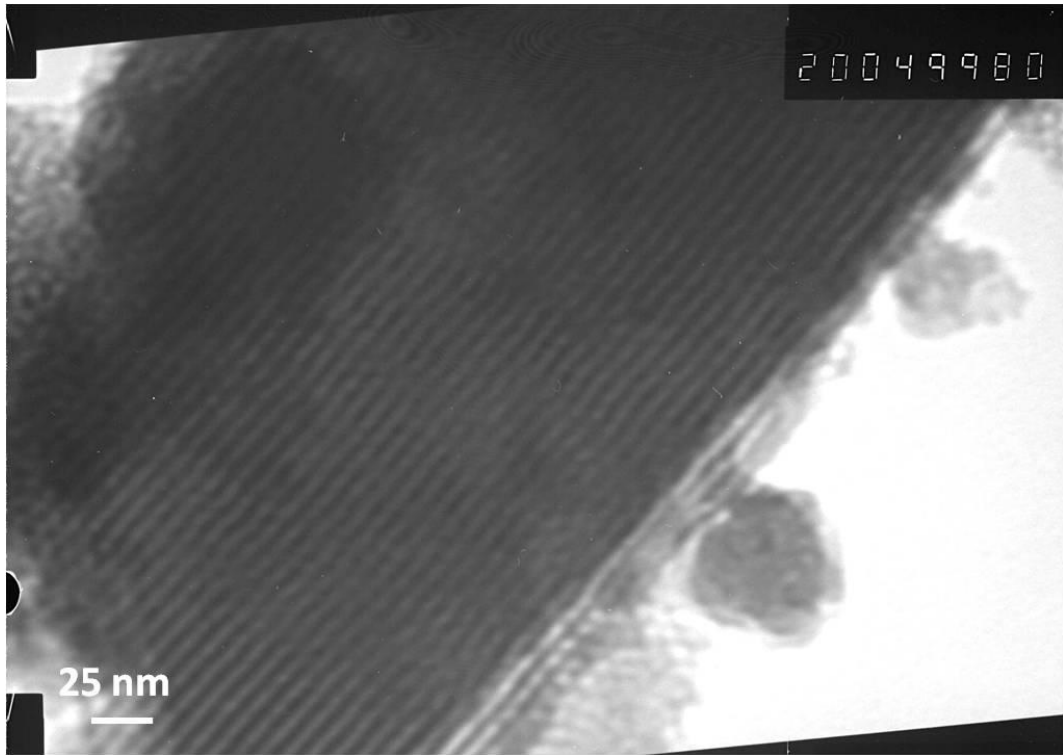


Figura 2.18. Bright field TEM image of the calcined mesoporous silica film

This organization is due to structure distortion during thermal *shrinkage* produced by

T

calcination. The organized interconnected porous structure is very suitable for both post-synthesis grafting of doping molecules or co-condensation.

Several examples are reported in literature and show that after incorporation, both via physical adsorption or chemical bonding, the molecules maintain their activity and are well entrapped within the matrix without significant leakage¹⁸¹.

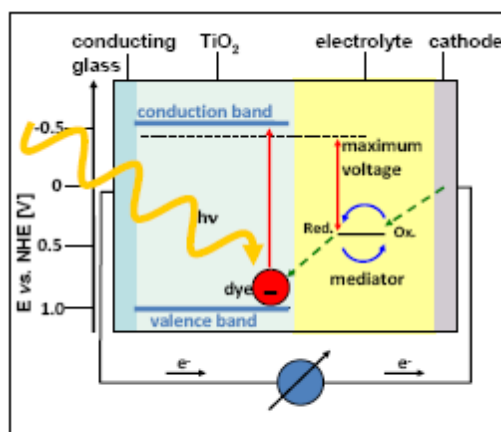
2.3.6 Thermogravimetric analysis (TGA)

The thermal decomposition behaviour of all mesostructured solids (hybrids and blanks) was studied using TGA measurements.

In the range of 413÷873 K, SiO₂(CTAB) and SiO₂(P123) samples exhibit a weight loss attributed to the surfactant decomposition, of 44.8% and 36.5% respectively. In the same range of temperature, SiO₂([Ir]•CTAB) and SiO₂([Ir]•P123) samples exhibit a weight loss of about 48.3% and 39.7%, which probably corresponds to the decomposition of [Ir] together with the surfactant. The detected similar weight losses indicate similar behaviour despite the different templates used in the synthesis. Nevertheless, the difference of weight loss resulting from a comparison among the blank and the corresponding hybrid materials (approximately 3%) cannot be attributed only to the presence of [Ir] chromophore, and it probably arises from both the [Ir] decomposition and the intrinsic difference of weight ratio between the surfactants and the inorganic scaffold due to a different degree of order induced by the [Ir] co-assembling process. These results are supported also by XRD measurements and nitrogen sorption analysis, indicating that the presence of [Ir] in the micelles causes some variations of the surface parameters.

Chapter 3

Solid state dye-sensitized solar cells.



Solid state dye-sensitized solar cell comes from the replacing of the liquid electrolyte by an organic hole-transporting material (HTM) forms organic/inorganic heterojunction.

In 1988 Tennakone¹⁸² reported for the first time a solid-state dye-sensitized heterojunction between TiO_2 and CuSCN , however the *flat* structure of

the junction led to a low sensitized photocurrents. About 10 years later Hagen et al.¹⁸³ reported on a solid-state device based on a molecular semiconductor, which was applied to a $\text{Ru}(\text{dcbpy})_2(\text{SCN})_2$ sensitized nanocrystalline TiO_2 electrode via thermal evaporation. However energy conversion efficiencies were still low (IPCE < 0.2%). The first solid-state dye-sensitized heterojunction of TiO_2 and a semiconducting polymer was reported by Yanagida and co-workers.^{184,185}

The charge transport mechanisms inside the cell are very similar to the dye-sensitized using a liquid electrolyte, except for the electrolyte. In the liquid electrolyte solar cell where there is a migration like a diffusion process, contrary to the solid state solar cell where exists an *hopping* of charges through the solid charge transport material, more correctly the Hole-Transport Material (HTM). The **Figure 3.1** shows this hopping mechanism where electrons are hopping from one hole-conductor molecule to the other.

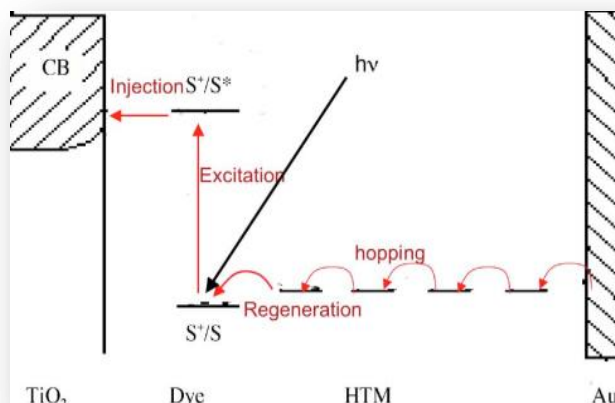


Figure 3.1. Principle of operation scheme of the solid-state dye-sensitized solar cell.

The choice of organic/inorganic heterojunction joins the well know properties of the former, such as flexibility, amorphous structure, almost unlimited chemical tunability and easy processability and with the high charge mobility, and long-term stability of the inorganic materials.

The main problem of these cells has been fast interfacial electron-hole recombination, reducing the diffusion length of the conduction band electrons to a few microns as compared to 20–100 microns for the electrolyte-based DSC¹⁸⁶.

As a consequence, the film thickness employed in these cells is restricted to only 2 microns, which is insufficient to harvest the sunlight by the adsorbed sensitizer, thus reducing the resultant photocurrent. The dye monolayer itself blocks this back reaction because it is electrically insulating¹⁸⁷.

Another difficulty encountered has been the filling of the porous network with the hole conductor. This impediment may be overcome by developing oxide films having regular mesoporous channels aligned in a perpendicular direction to the current collector. On the other hand, the V_{OC} values obtained with solid state DSCs are high, reaching nearly 1 V, due to a better match of the hole conductor work function than that of the electrolyte with the redox potential of the sensitizer.

Hence, current efforts are being directed towards molecular engineering of the interface to improve the compactness and order of monolayer and prevent in this fashion the charge carriers from recombining.

Moreover the solid hole-conductor is the less efficient hole transport respect to the liquid electrolyte as a result of the relatively low hole mobilities in organic semiconductors. Low conductivities imply high resistance causing voltage losses, in particular for high current densities. Slow charge transport generates concentration gradients in the hole conductor matrix. The interfacial recombination depends on the concentration gradient of holes in fact as a consequence of the accumulation of holes inside the pores there is a holes-depletion effect in the bulk organic semiconductor. This phenomenon is favored by a low distribution of the solid charge transport material into the porous matrix, respect to the liquid electrolyte that forms a perfect semiconductor/electrolyte junction^{188,189,190}.

A schematic diagram of the solid sate DSC is shown in **Figure 3.2**.

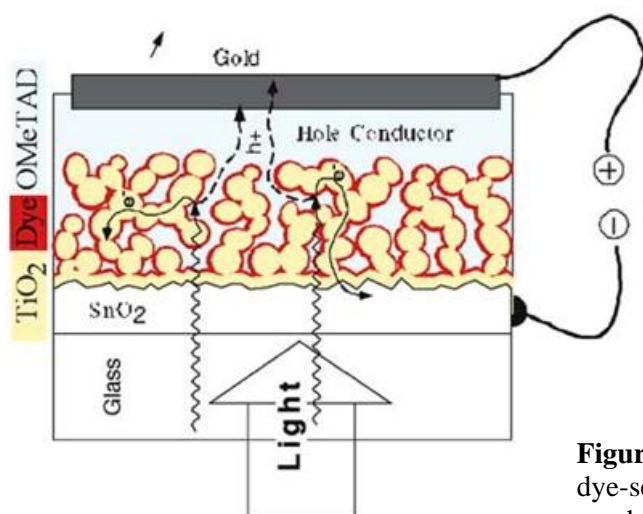


Figure 4. Cross-sectional view of a solid state dye-sensitized photovoltaic cell using the hole conductor spiro-OMeTAD.

3.1 Materials

All reactions were carried out under an argon atmosphere. Solvents were distilled from appropriate reagents. All reagents were purchased from Sigma–Aldrich.

3.1.1 The substrate

The concept of using dispersed particles to provide a sufficient interface area for dyes chemisorptions¹⁹¹ emerged from 1970s¹⁹², and was subsequently employed for photoelectrodes¹⁹³.

In the solid state solar cell there is a monolithic structure, the layer depositions are made one by one from the bottom to the top of the cell.

Highly fluorine-doped transparent conducting oxide films deposited on glass (SnO₂:F) were purchased either from Pilkington (TEC15, USA), distributed in Switzerland by Hartford. TEC15 displays a optimal thermal stability, it was observed after two sintering treatments at 500°C for 10 minutes (heating rate 50 °C/min.) The Fluorine doped Tin Oxide (FTO) layer, was chosen for its low resistance (15 Ω cm) and the better thermal stability compared to Indium doped Tin Oxide (ITO). The FTO layer should improve the mechanical and the electrical contact with the porous semiconductor film.

Titanium dioxide was chosen as semiconductor for the photoelectrode.

The choice of semiconductor is fundamental, it has to fulfill three functions.

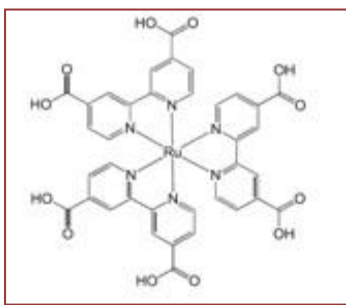
- It has to be in a nanocrystalline form, its structure, with a mesoscopic particle size (15-20nm), has to offer an optimal adsorption surface for the dye.
- It has to have a wide bandgap to accept the electrons from the excited dye.
- It has to be a good electron conductor to diffuse electrons toward the conducting glass.

TiO₂, used in its low-temperature stable form anatase (pyramid-like crystals), is a good choice for photo-electrochemical applications, first of all for its energetic properties (E= 3.2 eV, CB: -3.8 eV), also for its stability, due to the wide band gap, the Lewis acidity of the surface, allowing attachments of dyes, the widely available, low-cost and non-toxic and biocompatible conditions; of course TiO₂ is an isolator which becomes conductive by electron injection of the adsorbed dye. Furthermore the TiO₂ semiconductor has to have a porous structure to enhance the light capture characteristic of dye respect to a flat surface.

Whether the solar cell is fabricated with just the nanocrystalline (porous) layer between the back contact layer FTO and the hole-conductor material it is possible that an ohmic contact appears and a short circuit reduces the dark current of the device. Therefore a thin compact layer of a semiconductor material is deposited under the nanocrystalline one. This compact layer improves the mechanical adhesion of the porous film on the substrates.

3.1.2 Dyes

The history of the sensitization of semiconductors to light of wavelength longer than that corresponding to the band gap is an interesting convergence of photography and photoelectrochemistry⁵, both of which rely on photoinduced charge separation at a liquid–solid interface¹⁹⁴. The silver halides used in



photography have band gaps of the order of 2.7–3.2 eV and are therefore insensitive towards much of the visible spectrum, as are the metal oxide films now used in dye-sensitized solar cells.

Initial photochemical studies employed a [Ru(4,4'-dicarboxylic acid 2,2'-bipyridine)₃] sensitizer.

Progress thereafter, until the announcement in 1991¹⁹⁵ of a sensitized electrochemical photovoltaic device with conversion efficiency of 7.1% under solar illumination, was incremental, through the combining of a synergy of structure, substrate roughness and morphology, dye photophysics, and electrolyte redox chemistry. That evolution has continued progressively since then, with certified efficiencies now over 11%¹⁹⁶.

The dye is the sensitizer of the solar cell, absorbed by the semiconductor layer. It is a photoactive element able to harvest the incident light for the photon-to-electron conversion. To allow a rapid injection of excited electron into the CB of TiO₂, it is sufficient only a thin monolayer of dye by the wetting of the porous film. The dye has to promote the separation and mobility of the charges within the solar cell, therefore it must to fulfill some requirements, high light harvesting; high molecular extinction coefficient; broad spectral response; no aggregation (“filter effect”) on TiO₂; absorb visible light of all colors (panchromatism), ideally, all photons below a threshold wavelength of about 920 nm should be harvested and converted to electric current. This limit is derived from thermodynamic considerations, showing that the conversion efficiency of any single-junction photovoltaic solar converter peaks at approximately 33% near a threshold energy of 1.4 eV^{197,198}.

Also, the sensitizer should have suitable ground and excited state redox properties, and interlocking groups for grafting the dye on the semiconductor surface. These establish intimate electronic coupling between its excited state wave function and the conduction band manifold of the semiconductor^{199,200}.

The photophysical and photochemical properties of 4d and 5d metal complexes containing polypyridyl ligands have been thoroughly investigated over the last three decades. The ground and the excited state electrochemical and photophysical properties of these complexes play an important role in the charge transfer dynamics at the interfaces. The choice of Ru(II) polypyridyl complexes, in nanocrystalline TiO₂-based solar cells^{201,202,203,204}, is of interest for a number of reasons:

- Because of its octahedral geometry specific ligands can be introduced in a controlled manner

- The photophysical and electrochemical properties of Ru complexes can be tuned in a predictable way
- The Ru metal center possess stable and accessible oxidation states from I to III

Electrochemical properties

The solar spectrum is centered in the visible light wavelength range (400nm–900nm) therefore it is very important that the sensitizer absorbs the solar spectrum in this wavelength range. The efficiency of electron injection from the sensitizer to into the TiO₂, is in relation with the energy level of the sensitizer excited state, the last has to be more negative in energy than conduction band level of TiO₂; or in other word the oxidation potential of the dye has to be more positive than the oxidation potential of the electron donor (HTM).

Photophysical properties

In order to optimize the current density, the extinction coefficient of the sensitizer has to be high at wavelengths different from the maximum absorption peak since the white light harvesting efficiency is limited by the absorption in the weaker absorbing regions, and for an efficient electron injection, the lifetime of the excited-state (S*) has to be long enough to avoid the vibration relaxation of the dye itself.

Chemical Properties

To have a good adsorption of the sensitizer onto the semiconductor layer, the dye needs to be bond to the TiO₂ surface. For organometallic dyes, the carboxyl groups are the anchoring group. With decreasing distance of the dye to the surface the electron injection rate increases, it is very important to obtain only a monolayer of dye onto the TiO₂ surface. However the electron injection rate can be accelerated when the system of the dye in the excited state can be delocalized into the semiconductor. Therefore it is fundamental that the substrate is soaked into the dye solution. Generally the dye solution is based on an inert solvent which allows reasonable amounts of dye to be dissolved and which does not interact with semiconductor surface.

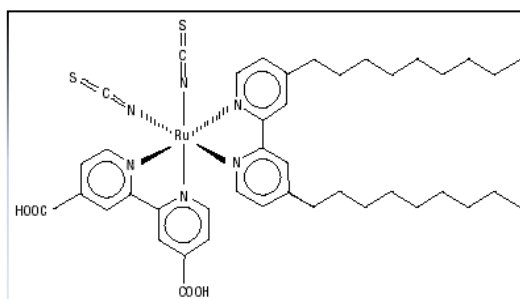
Stability

One major issue that has been settled during this period is that the sensitizers employed in the current dye-sensitized solar cell embodiments can sustain 20 years of outdoor service without significant degradation.

However, as new and more advanced dye structures emerge, and in order to avoid repeating these lengthy tests every time the sensitizer is modified, kinetic criteria have been elaborated to allow prediction of long-term performance.

The dye must possess a long-term photovoltaic performance stability first the final solar cell has to be reproducible and also because of the *real-life* applications require cell lifetime of more than 20 years possess long-term stability.

Nowadays ruthenium complex cis-[RuII(dcpby)₂(NCS)₂] (figure on the right) is the best dye for the application in dye-sensitized solar cells. This is mainly due to the good stability of the ruthenium complex compared to other sensitizers. In



this work a short study about this dye is reported to verify the forthcoming experimental data.

However, due to the precious metal and its rarity, metal-free organic dyes have attracted considerable attention for practical applications. Recently, the solar-cell performances of DSSCs based on organic dyes have been remarkably improved and impressive efficiencies in the range 8–9.7% have been achieved²⁰⁵. The main factors responsible for the low efficiencies of organic dyes compared to the ruthenium sensitizers are narrow absorption bands in the visible region and the formation of dye aggregates on the semiconductor surface²⁰⁶.

Therefore, many attempts have been made to design and construct organic dye molecules with higher molar extinction coefficients and broader spectral responses. Most of the efficient organic dyes contain a donor and acceptor bridged by a p-conjugated linker (D-p-A). To enhance the molar extinction coefficient as well as to realize panchromatic lightharvesting, tuning of the length and torsion angle of the conjugated linker is important.

Recently, a successful approach was introduced in which a p-conjugated linker such as a thiophene²⁰⁷ or thienothiophene²⁰⁸ derivative was incorporated into an

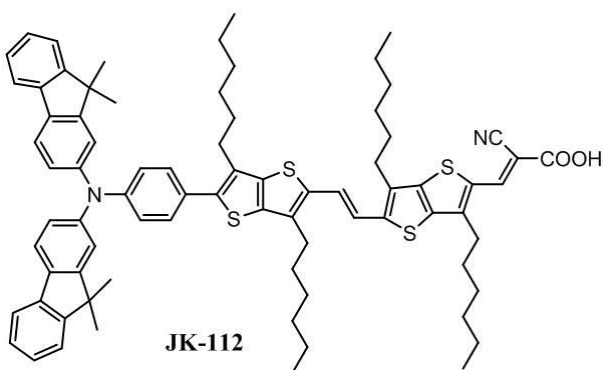
organic framework, thereby enhancing the efficiency and stability. Herein, we report highly efficient organic sensitizers, coded as JK-112 and JK-113 (Scheme 1), which consist of a dimethylfluorenylamino-appended thienothiophene–vinylene–thienothiophene unit with aliphatic chains that maintain the planar geometry of the conjugated linker. This not only increases the extinction coefficient of the sensitizer by extending the p-conjugation of the bridging linker, but also augments its hydrophobicity, increasing the stability under long-term light soaking and thermal stress.

3.1.2.1 Z907

(*cis*-di(thiocyanato)-(2,2'-bipyridyl-4,4'-dicarboxylic acid)(4,4'-dinonyl-2,2'-bipyridyl)-ruthenium (II)) were synthesized, according to published procedures^{209,210,211}, and were used as received from Prof. Graetzel co-workers Dr. Nazeeruddin and Dr. Zakeeruddin. The dyes were dissolved in a 1:1 mixture of acetonitrile:tert.-butanol and were used as received without further purification.

3.1.2.2 New organic dyes

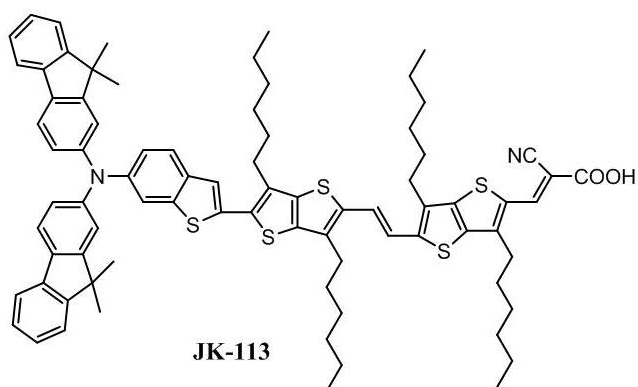
JK-112²¹²



(Z)-3-{5-[(E)-2-(5-{4-[Bis(9,9-dimethyl-9H-fluoren-2-yl)amino]phenyl}-3,6-dihexylthieno [3,2-b]thiophen-2-yl)vinyl]-3,6-dihexylthieno [3,2-b]thiophen-2-yl}-2-cyanoacrylic acid
A mixture of

(*E*)-5-[2-(5-{4-[Bis(9,9-dimethyl-9H-fluoren-2-yl)amino]phenyl}-3,6-dihexylthieno[3,2-b]thiophen-2-yl)vinyl]-3,6-dihexylthieno[3,2-b]thiophene-2-carbaldehyde (0.16 g, 0.140 mmol) and cyanoacetic acid (0.024 g, 0.28 mmol) was vacuum-dried and then dissolved in MeCN (60 mL) containing piperidine (0.012 g, 0.140 mmol). The solution was refluxed for 6 h. After cooling, the volatiles were removed in vacuum. See **section 5.2**.

JK-113²⁰⁷



(Z)-3-{5-[(E)-2-(5-{6-[Bis(9,9-dimethyl-9H-fluorene-2-yl)amino]benzo[b]thiophen-2-yl})-3,6-dihexylthieno [3,2-b]thiophen-2-yl)vinyl]-3,6-dihexylthieno [3,2-b]thiophen-2-yl}-2-

cyanoacrylic acid

Compound JK-113 was synthesized by a procedure similar to that described for JK-112, except that (E)-5-[2-(5-{6-[Bis(9,9-dimethyl-9H-fluorene-2-yl)amino]benzo[b]thiophen-2-yl})-3,6-dihexylthieno[3,2-b]thiophen-2-yl)vinyl]-3,6-dihexylthieno-[3,2-b]thiophene-2-carbaldehyde (0.21 g, 0.175 mmol) was used. See **section 5.2**

3.1.3 Hole Transport Material

The main difference between the liquid electrolyte dye-sensitized solar cell and the solid state one, is that the last makes use of an *hole conductor*, or Hole Transport Material (**HTM**), to regenerate the oxidized dye after electron injection into the semiconductor. The second function of the HTM is to transport the positive charge into the counter electrode. Therefore to achieve these functions some requirements have to be fulfilled.

Electrochemical Properties

The HTM has to be able to reduce the oxidized dye, the redox potential of the hole conductor must be more negative than that of the oxidized dye. Since the maximum photovoltage of the dye-sensitized solar cell depends on the HOMO level of the HTM, this HOMO level should be as low as possible in order to achieve a maximal device voltage under illumination. Furthermore, the hole-conductor should not be able to quench the excited state of the dye, this recombination reaction has to be much slower than the injection of the excited electron into the semiconductor.

For the regeneration of the dye, the hole conductor has to have a redox potential higher than that of the oxidized species. In other words, the HTM has to have a HOMO level higher than that of the oxidized dye. The difference between the two potentials should be large enough to ensure a good driving force for the process.

It is important that the redox-couple must be reversible at the counter electrode, while being inert to the TiO₂. The reaction between HTM and dye has to be slower than the electron transfer between the dye and the TiO₂, the HTM oxidized form, must not interact with the excited state of the dye and the TiO₂.

Photochemical Properties

The HTM should not have any significant light absorption in the visible domain, to avoid an internal filter effects and a competition with the dye.

Morphological Properties

The hole conductor should be deposited on the substrates without damaging the sensitized semiconductor, different techniques are used, in this work the HTM is deposited by spin-coating. The HTM has to have an amorphous structure and it has to be transparent to allow light to penetrate the device, stable and homogeneous. The hole conductor has to penetrate the pores of the nanocrystalline network. This limits the size of the molecules of the compound, as the pores have sizes in the nanometer scale. The contact with the counter-electrode should have an ohmic behaviour to minimize the internal resistance of the device. Finally, the HTM has to be stable to a long storage and exposure to open air that lead to a lower conversion efficiency.

Charge Transport Properties

The Dye/HTM system should be able to transport a current of a few mA/cm² without diffusion losses or high resistance. The limiting current depends on the thickness of the hole transport material, the number of charge carriers and the mobility μ , which is a material constant:

$$J_n = \mu \cdot k \cdot T \cdot \frac{dn}{dx}$$

One of the solutions to this question, for enhancing the conductivity, is to doping the HTM by oxidation, increasing the number of charge carriers. In other words,

the Fermi-level shifts towards the transport states upon doping. Furthermore the resistive losses can be reduced by adjusting the layer thickness of the hole conductor.

Solid-state dye-sensitized solar cells (DSC) based on organic hole conductor, 2,2',7,7'-tetrakis-(*N,N*-di-*p*-methoxyphenylamine)-9,9'-spirobifluorene, spiro-MeOTAD), have been investigated as an alternative to liquid electrolyte solar cells.^{213,214,215,216,217,218}

The *spiro*-OMeTAD is the most successful p-type organic conductor (hole transport material) employed. Its work function is about 4.9 eV and the hole mobility $2 \times 10^{-4} \text{ cm}^2 \text{ s}^{-1}$.

Spiro-OMeTAD was used as received from Dr. Spreitzer - Covion Organic Semiconductor GmbH, Frankfurt/Germany (formerly Aventis, formerly Hoechst AG). If not stated otherwise the purity was > 99.8 %, according to HPLC analysis.

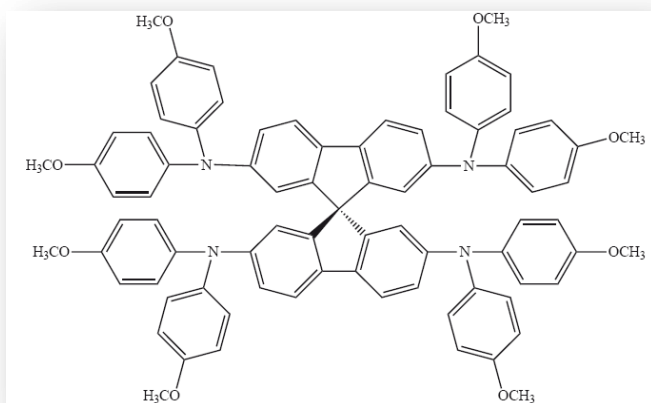


Figure 3.3. Structure of 2,2',7,7'-tetrakis(*N,N*-di-*p*-methoxyphenyl-amine)-9,9'-spirobifluorene (spiro-OMeTAD).

The reduced form of the hole conductor is pale yellow and absorbs in the UV (max=372 nm). The spectrum of spiro-MeOTAD⁺ shows an intense band at 511 nm and a shoulder at 700 nm. The spiro center connects two identical molecule units in a perpendicular arrangement and acts as an electronic barrier. Therefore the spectrum of the spiro-MeOTAD²⁺ is similar to the mono cation but with a doubled extinction coefficient.

The comparison of similar molecules with and without spiro center revealed that the spiro-concept leads to high morphologic stability, without deteriorating its electronic properties.²¹⁹

One of the limits of solid state DSSC is the TiO₂/spiro-OMeTAD thickness that inhibits high light harvesting efficiencies. One reason for this limitation has been identified in the shorter electron lifetime of the cells due to the fast recombination of electrons with holes in spiro-MeOTAD.²²⁰ Another reason, which has been cited as preventing the use of thicker films, is poor pore penetration of spiro-MeOTAD which is usually applied by spin coating from solution.²²¹ In an unfilled pore, the dye molecules can still inject electrons into the TiO₂ but they are not regenerated and the oxidized dye molecules recombine with electrons from the TiO₂. Alternatively, if the HTM is not interconnected everywhere, then all dye molecules can be regenerated but the positive charge cannot be transported out of the cell.
222,223

Another factor that limits the efficiency of these cells is the high rate of back reaction of electrons with the oxidized spiro-MeOTAD. Improved open circuit voltages are observed when tertiary butyl-pyridine (t-BP) is incorporated into the hole transporting matrix.³⁰ Furthermore the un-doped spiro-MeOTAD is insulating, however, when only Li(CF₃SO₂)₂N is added, the film becomes conducting. The spiro-MeOTAD becomes slightly oxidized during cell preparation in air, and the addition of the lithium salt shields the charges so that DC conductivity is observed.

Respect to other hole transport materials, that exhibit an amorphous structure for a short time, spiro-MeOTAD film can stay in the amorphous state for years. The standard deposition technique is spin-coating of a solution of spiro-MeOTAD in chlorobenzene onto the sensitized semiconductor surface.

Preparation of the hole-conducting matrix:

2,2',7,7'-Tetrakis(N,N-dimethoxyphenylamine)-9,9'-spiro-bifluorene

(spiro - OMeTAD), (72 mg) was dissolved in C₆H₅Cl (420 mL) at 60°C.

Distilled 4-tert-butylpyridine (TBP) (7 ml) and 15 ml of a solution of Li [(CF₃SO₂)₂N] (17 mg) in MeCN (100 ml) were then added to the solution.

3.1.4 Counter Electrode

The device was defined between the FTO anode and gold cathode. The gold counter electrode is of advantage due to its higher reflectance and conductivity.

Correspondingly best performance was observed for the thickest counter electrode in a device series with gold layers varying between 20 and 100 nm. The enhanced performance for thicker films was the result of increased short circuit currents. However the deposition of thicker films requires longer evaporation times and thus longer thermal stress for the devices. Gold films thicker than 100 nm become mechanically instable and tend to peel off. Devices were therefore provided with a gold counter electrode of 100 nm.

3.2 Device preparation

The solid state dye-sensitized solar cell technology developed at the EPFL contains broadly five components:

1. Conductive glass substrate
2. Semiconductor film
3. Sensitizer
4. Hole-transport material
5. Counter electrode

3.2.1 TiO₂ layer

The structuring of the FTO on a glass substrate was done via a chemical etching method. Zinc granulates were spread onto the glass (20 mg/cm²) followed by a reaction with HCl 4M (1ml/cm²). Scotch® tape was used to mask the tin oxide area needed to the back contact. The rapid reaction between HCl and Zn leads to the removal of the SnO₂. After two treatments of 3 min reaction time the SnO₂ is removed. The FTO glass structured is then cleaned by rubbing it with a paper soaked in acetone / ethanol mixture, followed by scrubbing with a soft toothbrush and Hellmanex® surfactant (2% in H₂O). The FTO glass was subsequently purified by a UV/Ozone plasma treatment (UVO-Cleaner®, Model No. 256-220, Jelight Company Inc.) for 20 minutes.

Thin compact TiO₂ layers were prepared using as precursor diisopropoxytitaniumbis(acetylacetonate) (TAA®, purchased from Aldrich). The TAA solution, stored under argon, was diluted with ethanol to 0.02M prior to use, as the solution changed color from yellow to orange in air.

The smooth compact film of about 100 nm is deposited by spray pyrolysis onto the conducting oxide glass with the solution of 0.02 M TAA, according to the procedure described by Kavan²²⁴. The sample (11x15 cm), partially etched (removal of SnO₂) was heated on a massive titanium plate (10x280x200 mm). The temperature was set to 450°C and controlled by a NiCr/Ni thermopile. The precursor solution was sprayed from a distance of around 20 cm using a chromatographic atomiser (Glas Keller, K1596)²²⁵. The sample surface was partially masked with 1 mm thin float glass in order to avoid complete coverage of the glass by the compact TiO₂ layer. For layers of approximately 100 nm thicknesses on a surface of 11x15 cm, 8 ml of the precursor solution were sprayed at intervals of 10 sec. This spraying technique corresponds to an overall precursor solution consumption of about 0.05 ml/cm².

In order to obtain complete transformation to TiO₂ and burn of all residual organics, the sample was left 10 minutes on the hot-plate (at 450°C) following deposition²²⁶.

The TiO₂ colloidal pastes were produced by P. Comte and R. Charvet, LPI, EPFL following the procedure described by Barbé²²⁷:

1. precipitation (hydrolysis of Ti-alkoxides using 0.1 M HNO₃)
2. peptisation (heating at 80 °C for 8 h) followed by filtering
3. hydrothermal growth (autoclave: 12 hours at 230°C)
4. sonification (ultrasonic bath, 400 W, 15 x 2 s)
5. concentration (rotavap: 45°C, 30 mbar)
6. Solvent exchange, ethyl cellulose and terpineol addition (flocculation, sedimentation)
7. Homogenize paste (3-roll mill, 15 minutes)
8. Dilution with ethanol 3X (making paste more fluid)

The resulting TiO₂ particles consist of anatase or a mixture of anatase and rutile depending on reaction conditions.

After removal of solvent, addition of a binder and dilution with ethanol, the sol is now ready for deposition onto the thin compact TiO₂ layer.

The nanocrystalline TiO₂ layer was deposited using the “Doctor-blading” method. The substrates were fixed on a glass support using Scotch® tape (60 µm thick), determining the deposition area and the layer thickness. The paste was deposited

onto the substrate-plate using a spatula of the “doctor-blading machine” (speed: 30mm/s). This method leads to a optimal quality/reproducibility of the TiO₂ films. After deposition, the layers were allowed to sit in a dust-free container during 30 min. The substrates were then sintered, this technique is used to form interconnection between nanoparticles to improve the electronic contact; the porous film is typically a few micron thick, transparent and mechanically stable.

The sintering was made according to a programmed sequence:

T=100°C for 10 min → T=150°C for 5 min, *under normal atmospheric conditions in order to evaporate all of the solvents*

→ T=325°C for 10 min → T=450°C for 10 min and finally → T=500°C for 30 min, *in order to obtain reproducible grain growth and phase transformation of the TiO₂ particle.*

This method avoids excessively fast burning-out of the organic compounds present in the paste, which would form undesired carbon inclusions in the pores. The maximum sintering temperature, which is typically 450-600 °C, is determined by the physical properties of the substrate. The sintering program was carried out under a constant oxygen flux, since firing the titanium dioxide in a reducing atmosphere, such as hydrogen for example, may create oxygen vacancies, leading to n-type doping²²⁸.

A final post-treatment by a 40 mM aqueous TiCl₄ solution for 30 min at 70°C, was then carried out. This treatment has been shown to increase the injection of electrons into the TiO₂ and, thus, augment the delivered current. This effect has been assigned to the enlarged surface area for dye adsorption as well as to the formation of a surface TiO₂ layer of higher purity¹⁷.

Furthermore Ti complexes in TiCl₄ solution are believed to condense at the junction points of two particles increasing interparticle connection and, thus, the electron transit from one particle to another. However, the treatment causes a decrease in the average pore size and the porosity. The porosity was calculated, using N₂ adsorption experiments (BET), from the ratio of the cumulative pore volume V_p to the total volume V_{tot}, which is given by $V_{tot}=V_p+\delta(TiO_2)^{-1}$, with density of anatase $\delta(TiO_2)=3.85\text{ g/cm}^3$. The particle size (PS) is approximate by $PS= 6/(SS* \delta(TiO_2))$, SS: specific surface.



Porosity = 66.2%, **particle size** = 20.0 nm, **specific surface** = 78.0 m²/g.

Upon dye uptake the effective porosity of the TiO₂ film is reduced by about 25%²²⁹. **Figure 3.4.**

Figure 4. FTO coated glass with TiO₂ film after sintering.

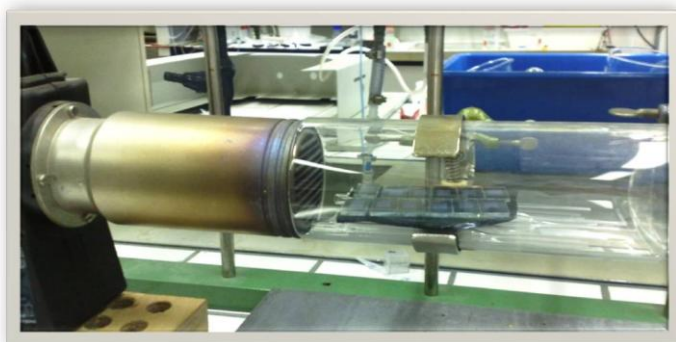


Figure 3.5. Second sintering.

The devices are separated (2.5 x 2.5 cm) and sintered for a second time for 30 minutes at 450°C (ramp: 15 minutes) and allowed to cool to 80°C immediately prior to the sensitizer application. **Figure 3.5.**

3.2.2 Sensitizer soaking

The Z907-dye sensitization of the nanocrystalline oxide films was obtained by immersion of electrodes in a mixture of 1:1 acetonitrile / tert-butanol sensitized solution (3×10^{-4} M) at room temperature for 3 hours in the dark.

For JK112 and JK113, TiO₂ electrodes were immersed in the dye solutions (3 mM in THF) at room temperature in the dark for 3 h.

During that time the concentration and the assembly of the dye on the electrode surface do not change significantly.

After 24 hours, the dye may spontaneously form a double-layer, increasing the pathways for electron injection into the semiconductor. In order to avoid this double-layer effect, the dye-sensitized electrodes were rinsed in acetonitrile prior to spin-coating of the hole-transport material.

3.2.3 Hole-transport material deposition

After rinsing the electrodes, a hole-conducting matrix (72 µl per 2.5x3 cm² area) was applied.

The HTM-matrix solution is deposited on the substrates and then, spun to fill the pores and form a flat, uniform layer at the surface of the substrate.

It is well known that the spin-coating technique is used to improve the penetration of the hole-conductor into the nanoporous layer.

The HTM is dissolved in dry chlorobenzene forming either a solution of 0.11 M. Some additives, such as lithium triflate (13 mM) and tBP (0.13 M), were added to the spiro-solution to increase the conductivity of the hole conducting layer and the open circuit voltage of the cell.

The substrate is spun up to a speed of 2000 rpm for 30 s with an acceleration of 2000 rpm/s. Then is directly dried under a vacuum of 10^{-6} mbar before application the counter-electrode by evaporation.

The Spiro-OMeTAD film thickness on top of the sensitized-nanocrystalline semiconductor is about 250-300 nm. This thickness acts as a spacer to avoid a direct contact between sensitized-heterojunction and the counter-electrode, which would lead to a short circuit.

3.2.4 Counter electrode deposition and the device sealing



Figure 3.6. Metal mask for gold evaporation.

A gold film of 100 nm was used as contact material. This layer was deposited by thermal evaporation under a vacuum of 5×10^{-6} mbar using a Edwards evaporator (Vacotec Auto 500). The evaporation rate was approximately 0.2 nm/s. A metal mask was used to define the contact areas on the sample (Figure 3.6).

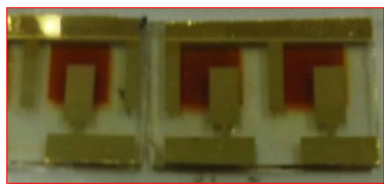


Figure 3.7. Solid state dye-sensitized solar cells.

The thickness of the counter electrode used was optimized with respect to the negative effects of the thermal stress on the dye solar cell, increasing with the evaporation time and the benefit effect of the light reflectance and the conductivity, increasing with the thickness of the layer²³⁰. The active area of each ssDSSC was about 0.2 cm^2 . **Figure 3.7.**

In order to measure the long-term stability of the solid-state dye-sensitized solar cells, the devices were encapsulated with a 2 mm glass sheet and sealing with a combination of the heat sealable Surlyn film and the epoxide Torr Seal, (Varian Vacuum Products). This sealing is necessary to maintain long-term stability devices and protect the active surface against mechanical stress and tBP evaporation.



Side-view of the solid state dye-sensitized solar cell.

3.3 Photovoltaic characterization

Absorption and photoluminescence spectra were recorded on a Perkin–Elmer Lambda 2S UV/visible spectrophotometer and a Perkin LS fluorescence spectrometer, respectively.

For photovoltaic measurements of the solid state DSSCs, the irradiation source was a 450 W xenon lamp (Osram XBO 450, USA), the power of which as an AM 1.5 solar simulator was calibrated using a Tempax 113 solar filter (Schott). The output power of an AM 1.5 solar simulator was calibrated using a reference Si photodiode equipped with a colour-matched IR cut-off filter (KG-3, Schott) to reduce the mismatch in the region 350–750 nm between the simulated light and AM 1.5. The measured IPCE values were plotted as a function of excitation wavelength by using the incident light from a 300W xenon lamp (ILC Technology, USA), which was focused through a Gemini-180 double monochromator (Jobin Yvon Ltd.).

Photovoltaic devices are generally characterized by measuring current density versus applied bias subjected to different intensities of illumination as well as in the dark. In addition, the determination of photocurrent under low intensity monochromatic light, i.e. incident-photon to electron conversion efficiency (IPCE), is often required.

3.3.1 Definitions^{45,231,232,233}

Under light illumination solar cells are often considered to be equivalent to an electrical circuit consisting of a current generation source in parallel with a diode and a resistor (shunt resistance (R_{sh})). There is also likewise a series resistance associated with the device (R_s), which describes the resistances of all of the materials utilised in solar cells fabrication.

In **Figure 3.8**. The equivalent electrical circuit scheme of the dye-sensitized cell. I_{light} represents the current generated from absorbed photons, I_{dark} represents the current which would flow, in the opposite direction, through the charge generation regions in the dark (diode current). The diode characteristics are due to the asymmetry within the device.

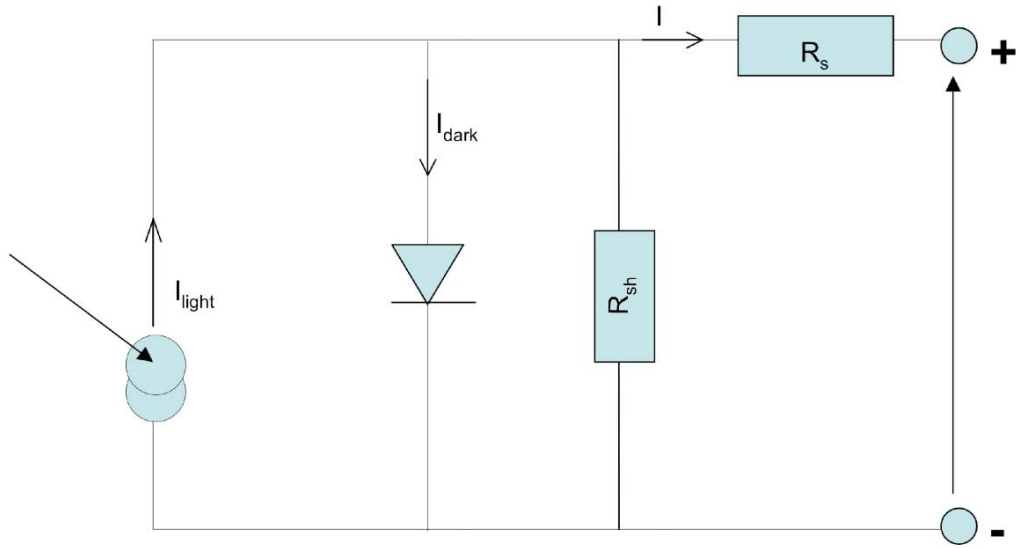


Figure 3.8. Equivalent electrical circuit scheme of the dye-sensitized cell.

The current-voltage characteristics of the solar cell are in according to the following mathematical form:

$$I = I_{light} - I_s \left(e^{V_a/V_{th}} - 1 \right) - \frac{V_a}{R_{sh}} \quad [mA] \quad (i)$$

Where I is the overall photo-current, I_s is the saturation current of the diode and V_{th} , the thermal voltage. I_{light} is assumed to be independent of the applied voltage V_a , which includes an element involving the series resistance.

$$V_a = V + R_s I \quad [V] \quad (ii)$$

The thermal voltage, V_{th} , is defined as

$$V_{th} = \frac{n \cdot k \cdot T}{e} \quad [V] \quad (iii)$$

where n is the ideality factor (typically varies from 1 to 2.4), e , the elementary charge and, k , Boltzmann's constant.

In the equivalent circuit it is showed the dark current in a one-diode system and, therefore, is only a simplified representation of actual dye solar cells. The real structure of the device is more complex and corresponds to a multi-diode model that takes into account the different charge transport processes within the cells.

The shunt resistance, R_{sh} , is normally much larger than the series resistance, R_s , allowing simplification of the (i) equation:

$$I = I_{light} - I_s \left(e^{V_a/V_{th}} - 1 \right) \quad [mA] \quad (iv)$$

The following parameters will be determined during the current-voltage measurements:

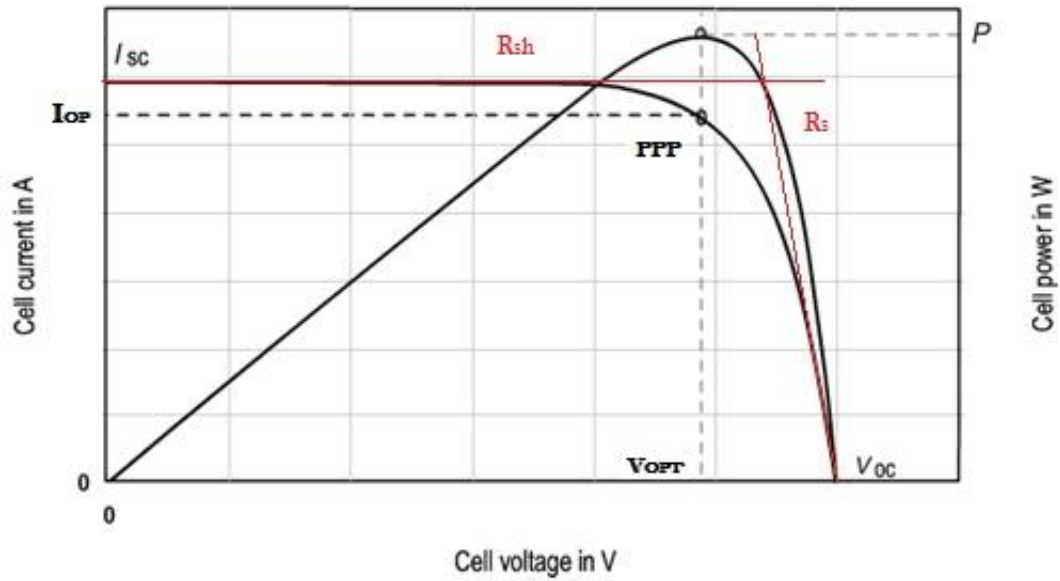


Figure 3.9. Representation of an IV curve (with I_{sc} , V_{oc} , I_{opt} and V_{opt}) and the power curve. PPP is the Point Peak.

Short-circuit current (I_{sc})

The measured current equals the short-circuit current (**Figure 3.9**) when the applied bias potential is zero ($V_a=0$). Equation (iv), thus reduces to:

$$I_{sc} = I_{light} \quad (v)$$

The short circuit current is a function of the irradiance. The short circuit current density (J_{sc}) is the short circuit current divided by the photoactive surface area of the cell.

Open-circuit potential (V_{oc})

When no current is flowing through the cell, ($I=0$), thus $V_a=V_{oc}$ (**Figure 3.8**) yielding equation

$$I_{light} = I_s \left(e^{V_{oc}/V_{th}} - 1 \right) \quad [mA] \quad (vi)$$

$$I_{oc} = V_{th} \ln \left(\frac{I_{light}}{I_s} + 1 \right) \cong V_{th} \ln \left(\frac{I_{light}}{I_s} \right) \quad [V] \quad (vii)$$

demonstrating the dependency of V_{oc} on light intensity (irradiance).

Maximal power output (P_{max})

The power delivered from a solar cell at an applied potential, V_a , is defined as the product of the current (at V_a) times the potential V_a :

$$P = V \cdot a \cdot I \quad [mW] \quad (viii)$$

The point where the power delivered reaches a maximum, P_{max} , corresponds to the so-called Peak Power Point (PPP) for the IV curve (**Figure 3.9**). The current and voltage corresponding to the PPP represent the optimal current (I_{opt}) and potential (V_{opt}) conditions for the cell.

$$P_{max} = V_{opt} \cdot I_{opt} \quad [mW] \quad (ix)$$

Fill factor (FF)

The fill factor (FF) measures the cell's quality as a power source and, therefore, is the ratio of the maximum power to the external short circuit current and open circuit voltage.

$$FF = \frac{V_{opt} \cdot I_{opt}}{V_{oc} \cdot I_{sc}} = \frac{P_{max}}{V_{oc} \cdot I_{sc}} \quad (x)$$

To be considered as a “good” (performing) photovoltaic cell, the fill factor should lie between 0.7 and 0.85. Fill factors values are influenced both by the series as well as the shunt resistances. The former, representing the internal resistance of the current source (depending on the resistivity of the materials and of the contacts with electrodes), should be as small as possible, with the shunt resistance, representing the resistance of the access to the core of the solar cell, as high as possible (**Figure 3.9**).

Efficiency (η)

The efficiency, describes the performance of the solar cell and is defined as the ratio of the maximum electrical power extracted (P_{max}) to the incident light intensity on the solar cell surface (P_{in}).

$$\eta = \frac{P_{max}}{P_{in}} = \frac{V_{oc} \cdot I_{sc} \cdot FF}{P_{in}} \quad (xi)$$

Standard conditions

In order to compare solar cells characterized in different laboratories world-wide, photovoltaic cells are measured under standard test conditions. These conditions specify that the temperature of the cell should be 25°C and that the solar radiation incident on the cell should have a total power density of 1000 W/m², with a spectral power distribution characterized as 1.5 AM. T The Air Mass is the path length which light takes through the atmosphere normalized to the shortest possible path length (that is, when the sun is directly overhead). The Air Mass quantifies the reduction in the power of light as it passes through the atmosphere

and is absorbed by air and dust. The Air Mass is defined as: $AM \approx \frac{1}{\cos \theta}$. where θ is the angle from the vertical (zenith angle). When the sun is directly overhead, the Air Mass is 1

An Air Mass distribution of 1.5 AM, as specified in the standard test conditions, corresponds to the spectral power distribution observed when the sunlight comes from an angle, $\theta = 48^\circ$.

Incident-Photon-to electron Conversion Efficiency (IPCE)

The measurement of the photocurrent under monochromatic illumination conditions yields the incident-photon-to-electron conversion efficiency (IPCE), defined as the ratio of the number of electron/hole pairs ($n_{\text{electrons}}(\lambda)$) generated in the external circuit of the solar cell to the number of photons ($n_{\text{photons}}(\lambda)$) incident on the photovoltaically active surface of the device at a fixed wavelength, λ .

$$ICPE(\lambda) = \frac{n_{\text{electrons}}(\lambda)}{n_{\text{photons}}(\lambda)} = \frac{I(\lambda)/e}{P_{\text{in}}(\lambda)/h \cdot \nu} = \frac{I(\lambda)}{\lambda \cdot P_{\text{in}}(\lambda)} \cdot \frac{hc}{\nu}$$

where $I(\lambda)$ is the current given by the cell subjected to light of wavelength, and $P_{\text{in}}(\lambda)$ the incoming power at wavelength, λ .

In general the IPCE is measured under short-circuit conditions. The spectral sensitivity $S(\lambda)$ is the product of the IPCE(λ) and the wavelength, If the spectral irradiation intensity $E(\lambda)$, is known the short-circuit current I_{sc} as be found utilizing:

$$I_{\text{sc}} = \int S(\lambda) \cdot E(\lambda) \cdot d\lambda$$

If the response (I-V curves) of the cell test is not linear, the IPCE will be a function of the light intensity.

3.3.2 Experimental Data

JK-112 as a sensitizer and 2,2',7,7'-tetrakis(N,N-dimethoxyphenylamine)-9,9'-spiro-bifluorene (Spiro-OMeTAD) as a hole conductor.

This device gave a J_{sc} of 8.0 mAcm^{-2} , a V_{oc} of 900 mV, and an FF of 60%, corresponding to an overall conversion efficiency η of 4.3% under standard global AM 1.5 solar conditions (**Table 3.1**).

JK-113 as a sensitizer and 2,2',7,7'-tetrakis(N,N-dimethoxyphenylamine)-9,9'-spiro-bifluorene (Spiro-OMeTAD) as a hole conductor.

This device gave a J_{sc} of 8.3 mAcm^{-2} , a V_{oc} of 920 mV, and an FF of 60%, corresponding to an overall conversion efficiency η of 4.3% under standard global AM 1.5 solar conditions (**Table 3.1**). At lower light intensity, the power conversion efficiency increased to 4.8% (JK-112), which is a remarkable value for an ssDSSC based on an organic sensitizer. Of particular note are the high V_{oc} values of the cells (both with **JK-112** (900 mV) and **JK-113** (920 mV)). This stems from the thinner TiO_2 film, which retards the charge recombination dynamics due to the higher absorption coefficient arising from extended conjugation.

Table 3.1 J–V characteristics of JK-112- and JK-113-sensitized solar cells with solid-state electrolytes under different light intensities. Comparison between organic and inorganic(Z907) sensitizers.

Dye	Intensity [% sun]	Jsc [mAcm^{-2}]	Voc [mV]	FF [%]	η [%]
JK112	10	0.8	780	73	4.8
	100	8.0	900	60	4.3
JK113	10	0.7	810	70	4.2
	100	8.3	920	57	4.3
Z907	100	12.5	730	67	6.1

Accelerate aging under light soaking at full sun (1000W/m^2).

Table 3.2 Stability-test results for JK-113.

After 24h @ 100% SUN				
JK113	-8,169	683,62	0,559	3,13
After 72h @ 100% SUN				
JK113	-5,005	670,09	0,537	1,80
After 168h (1week) @ 100% SUN				
JK113	-2,60	614,26	0,45	0,72

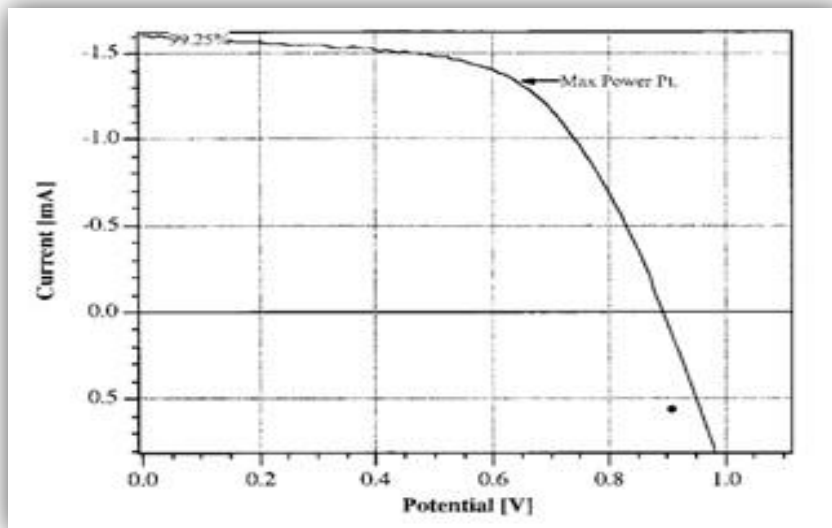


Figure 3.10. J–V characteristic of JK-112-sensitized solar cells with solid-state electrolytes under 100% sun light intensities.

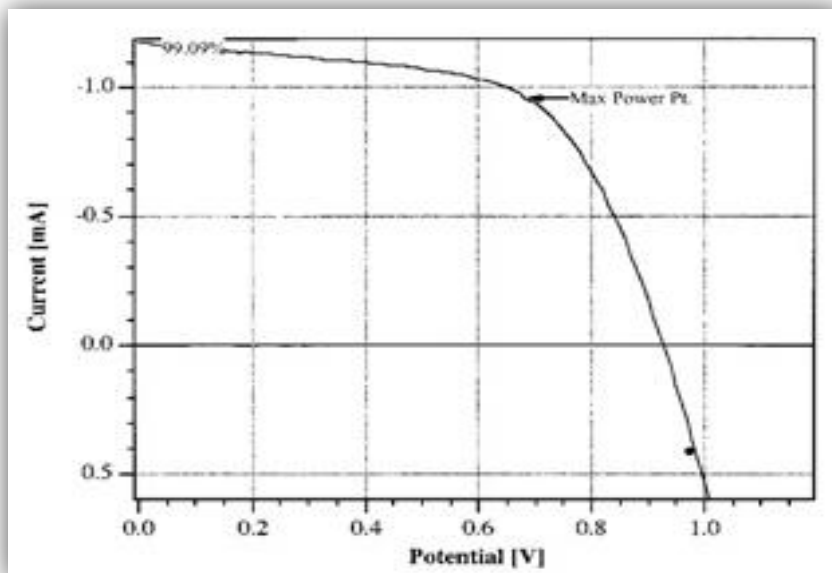


Figure 3.11. J–V characteristics of JK-113-sensitized solar cells with solid-state electrolytes under 100% sun light intensities.

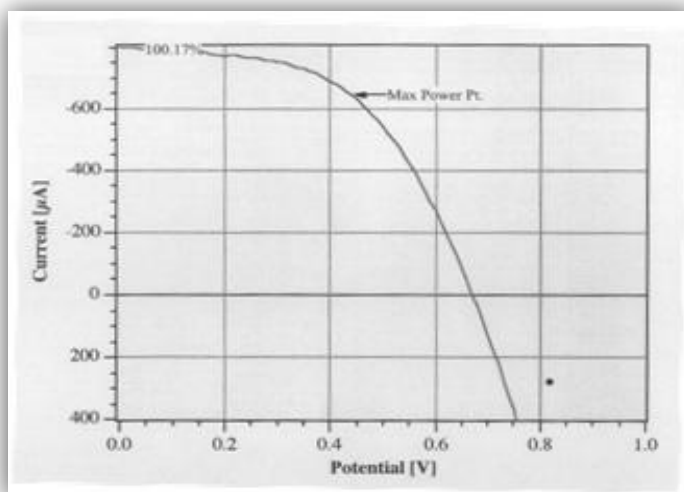


Figure 3.12.

J–V characteristics and JK-113-sensitized solar cells with solid-state electrolytes after 72h, stability test.

The incident monochromatic photo-to-current conversion efficiency (IPCE) of **JK-112** about 60% over the spectral region from 400 to 640 nm, reaching its maximum of 60% at 475 nm (**Figure 3.13**, red line). For JK.113 the IPCE value is about 50% over the spectral region from 400 to 640 nm, reaching its maximum of 50% at 465 nm (**Figure 3.13**, blue line)The band tails off toward 670 nm, contributing to the broad spectral light harvesting.

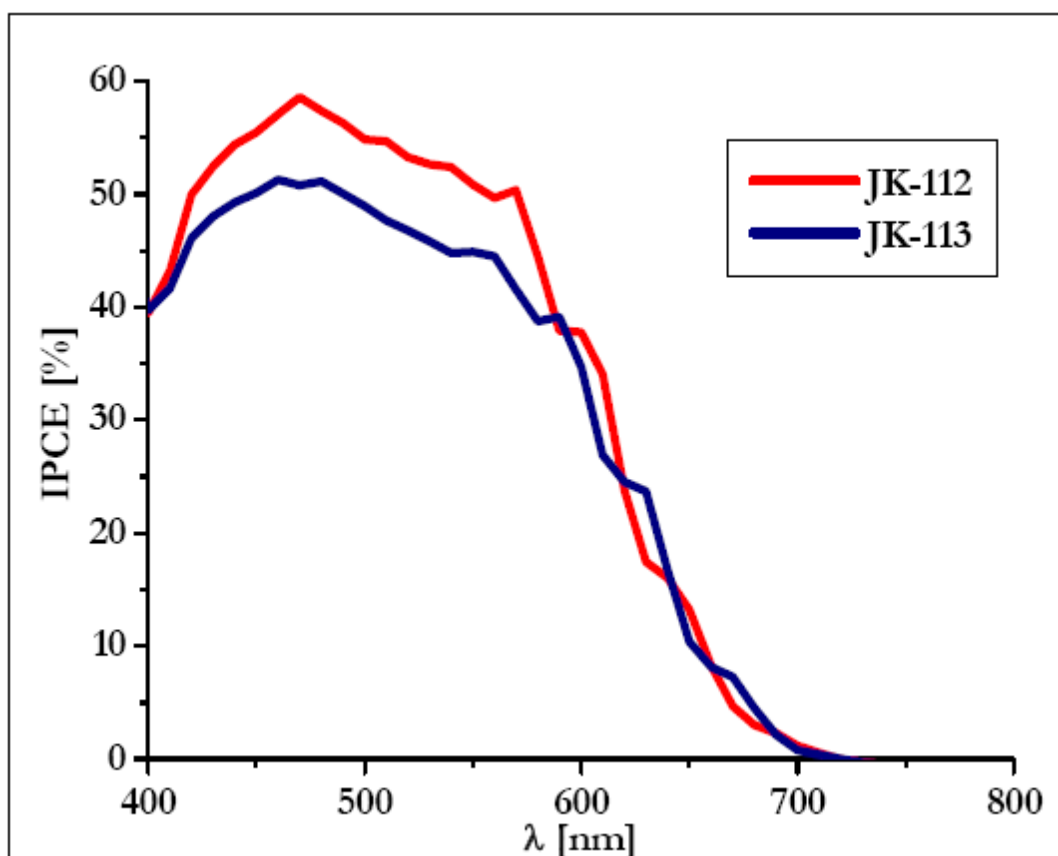


Figure 3.13. IPCE of solid-state DSC with JK-112 and JK-113.

The high extinction coefficients of **JK-112** and **JK-113** derive from increased electron delocalization over the conjugated system. Similar distortions have been reported for other organic dyes.^{234,235} **Table 3.3.**

Dye	λ_{\max} [nm]	ϵ [$M^{-1}cm^{-1}$]
JK112	365	5×10^4
	489	7×10^4
JK113	365	5×10^4
	490	9×10^4

Table 3.3. Extinction coefficients for JK-112 and JK-113-

Chapter 4.

Lighting devices – (LEEC)

Solid state lighting is an illumination technology based on the electroluminescence phenomena. Its applications are, amongst others, LEDs (light-emitting diodes), OLEDs (organic light-emitting diodes), and, sometimes considered as a sub-category of OLEDs, the LEECs (or LECs, light-emitting electrochemical cells). In this thesis, we present some observations of a preliminary study which examined the fabrication and applications of a relatively new light-emitting device, the LEEC.

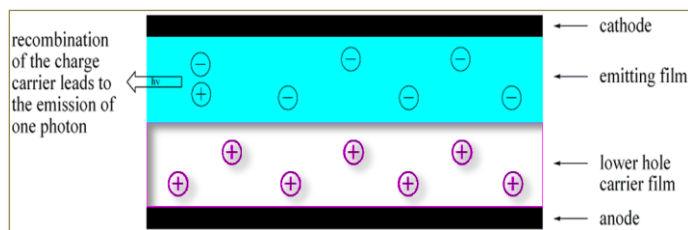
In 1962, *N. Holonyak*, working at the US company “General Electric”, gave the first practical demonstration of LEDs²³⁶. Over the course of the 1970’s, the physics of LED illumination was explained in detail,²³⁷ and by the end of the decade, LEDs had replaced incandescent bulbs for indicator lamps and Nixie tubes (small plasma discharge vacuum tubes) for numeric displays²³⁸. Starting in the mid- to late 1980’s, a new type of solid state lighting source was developed based on organic semiconductors^{239,240}. The performance of these OLED devices improved dramatically in the 1990’s until now, a consequence of worldwide efforts to develop full-color, flat-panel displays. By the turn of the century, the performance of OLEDs clearly showed that they had the potential for use in general illumination. The 1990’s also saw two major breakthroughs in inorganic LED technology²³³. The performance of LED devices, like that of their organic counterparts, steadily increased during the 1990’s. Since LEDs, in fact, SSL devices generally, can be fabricated in all the primary colours, they will, in time, serve as a source of white light for general purposes.

In recent years energy demands and environmental issues such as global warming have led to the search for clean renewable energy sources and more efficient technology, at least on an economical level. Lighting consumes up to 34 % of electricity in the United States, (*Worldwatch Institute, 2007*) and the production of the electricity costs more than \$ 60 billion a year²³³. It is obvious that lighting devices producers promise to replace conventional light sources, such as incandescent and fluorescent lamps, with more efficient devices.

Another important application of lighting technology is found in displays. The development of organic light emitting devices as a potential replacement for liquid

crystal displays (LCDs) has been the principal focus of much of the research in this field over the past decade.

4.1 Device Architecture



An OLED, **figure on the left**, consists of one or more organic layers sandwiched between two metal electrodes, one of

which must be transparent²³³. The organic layers are typically undoped and insulating molecules with a large π -conjugated system or polymers. These materials have essentially no free charges. Hence, the charges that run through the OLED during operation are injected into the organic layers from the electrode contacts. The cathode, which injects electrons into the device, should have a low work function (*i.e.* the minimum energy needed to remove an electron from an uncharged solid), allowing its energy to be close to that of the LUMO of the chromophore.

A good energy match between the LUMO and the cathode means that not much energy is lost when electrons are injected. Likewise, the anode should have a high work function and an energy close to that of the HOMO. Typically, the cathode is made of a reactive metal such as calcium, lithium, or magnesium, either singly or alloyed with another metal, while the anode is formed from indium tin oxide (ITO), a transparent conductor with a relatively high work function²³³. Once electrons and holes are injected into the organic layer, they drift under the influence of the applied field toward the opposite polarity contacts²³³. The electron and hole mobilities in the disordered layer are low, so a high field is required for appreciable current. Thus, the organic layers must be thin (on the order of 100 nm) for low-voltage operation. As electrons and holes hop from site to site, they sometimes land in the same place and form a neutral bound excited state, or exciton.

With properly chosen materials, a significant fraction of these excitons relax by emitting a photon so as to generate light. The color of the emitted light and the electrical characteristics of the OLED depend on the specific organic material and details of the device design.

On the other hand, the major technical problem for OLEDs is the limited lifetime of the organic materials. Furthermore, as three different compounds for each of the three colors red, green, and blue (RGB) are used, they all have differing stabilities resulting in color shifts during the lifetime of an OLED display.

Although OLEDs are not yet widely used, there is already considerable research into a possible successor, namely the light emitting electrochemical cells, abbreviated LEEC or LEC. A LEEC has a significantly simplified architecture compared to an OLED.

The principle of LEECs is essentially a simplified OLED structure. **Figure 4.1** depicts the stack of layers used in a typical LEEC. They are usually composed of two metal electrodes connected by (*i.e.* “sandwiching”) an emissive (“active”) layer containing the chromophore. On the chemical side, the chromophore in the emissive layer is not an uncharged compound (as in OLEDs) but rather an ionic one.

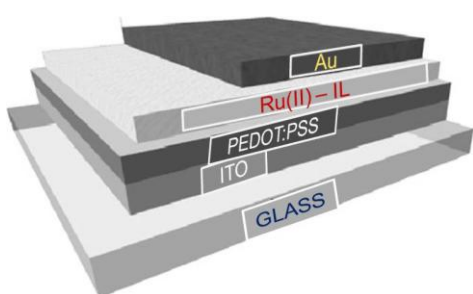


Figure 4.1. LEEC structure.

The invention of the LEEC (based on a conducting polymer) is attributed to the Nobel laureate *A. J. Heeger*.²⁴¹ [120]

LEEC devices are insensitive to the work function of the electrodes employed^{242,243}.

This is due to the generation of a strong interfacial electric field caused by the displacement of the mobile ionic species toward the charged electrodes when an external electric field is applied over the device²⁴⁴. Air-stable electrodes, such as gold, silver, or aluminium can be used.

Soon after the initial polymer-based LEEC by *Heeger et al.*, single-component, solid state light-emitting devices based on ionic transition-metal complexes have been reported^{245,246}. In this type of LEECs, the complexes perform all the necessary roles to generate light:

- (a) the decrease of injection barriers via the displacement of the counterions,
- (b) the transport of electrons and holes via consecutive reduction and oxidation, respectively, of the complex,
- (c) the generation of the photons.

The metal complex is an intrinsic molecular semiconductor, in which the HOMO is the t_{2g} of the metal centre, and the LUMO is a π^* orbital of the ligands²⁴⁷. On

application of a bias in this LEEC, holes and electrons are injected from the anode and the cathode, respectively, into the transition metal complex. These carriers are transported towards the opposite electrode *via* hopping, and may recombine to produce light emission with a characteristic color that corresponds to the energy gap of the complex. Critical to the operation of these LEECs are the counter ions (*e.g.* [PF₆]⁻), which are mobile in the film and at room temperature. Their redistribution on the application of a bias assists the injection of electronic carriers²⁴¹. However, the detailed working principles, such as the electric-field distribution within a device, are still debated,^{241,248} although the internal device operation can be observed directly²⁴⁹.

As with OLEDs, the benefits of LEECs in lighting applications and their usage in displays are numerous. Additionally to the advantages mentioned for OLEDs, LEECs operate at very low voltages, yielding high power efficient devices²³⁸.

Furthermore, they are easy and cheap to produce as they can be fabricated using spin-coating techniques rather than the chemical vapor deposition used for OLEDs. This, together with their overall simpler architecture (no encapsulation of the electrodes, fewer layers), LEECs represent a more economical alternative^{250,251,252,253}.

Unfortunately, LEECs based on ionic transition-metal complexes have limited stability. This has been attributed (in the case of a [Ru(bpy)₃]²⁺-based device) to a water-assisted ligand exchange reaction of the excited state molecule (“exciton”) and the subsequent formation of a new complex that functions as an efficient luminance quencher^{254,255,256}.

4.2 OLEDs vs. LEECs

Lifetime

Lifetime and reliability of OLEDs are major concerns in the practical application, although the fabrication technology has matured during the last decade. Lifetimes exceeding 10,000 hours have been shown²⁵⁷. Typically, luminance decreases with operation time and the higher brightness has the faster degradation. The lifetime corresponds to the time in hours before the overall luminance has been decreased below a given threshold value, often 50% of the initial luminance value.

In OLEDs with poor power efficiency, a high current density is needed in order to produce light. Only a few percentage of the power is applied to emit photons; the rest is converted to heat. The heat developed in the device causes degradation of the device. The increase of heat is proportional to the input current. The development of more power efficient devices would yield a reduction of the developed heat and a longer lifetime. The degradation process depends on colors that the material emits. To emit a blue color, a material with a larger bandgap is needed, which makes it harder to inject charge carriers and consequently more energy is needed. The high amount of current density makes the device more fragile and causes therefore a faster degradation for blue than for red and green emitting materials.

The life time of OLEDs depends strongly on such elements as efficiency, charge injection, mobility of carriers and so on. Charge carriers injected into organic layers are partially trapped and accumulate with time, eventually causing breakdown. This seems to be crucial for the OLED electrochemical long-term stability.

It is possible to reduce the degradation process by finding more power efficient organic materials. Doping the organic materials can result in a better power efficiency and a longer lifetime²⁵⁸.

The triplet excited states are enable to emit light instead of heat through phosphorescent doping. This not only yields a better power efficiency, but also reduces the time spent in the excited state. In the excited state the molecules could be considered more reactive and can cause a degradation of emitting layer due to unwanted chemical reactions. The reduction of triplet excited states would also lead to less heat generated and consequently to a better lifetime of the device.

Better multilayer structures can also bring a longer lifetime²⁵⁸. Depending on how the different layers are designed and in which order they are placed, the lifetime can be extended. The emitting layer plays a great role by affecting the lifetime. The addition of a hole transport layer enhances the lifetime by serving as stabilizer for the flow of holes and by increasing an overall power efficiency due to more recombination. The both transport layers do not only function as transport medium but also in some case function as buffers prevent humidity and oxygen to diffuse into the active emitting layer.

Unlike OLEDs whose operation is like diodes, LEECs can operate between forward and reverse bias. It is helpful to increase the stability by charge detrapping, which is similar to electronic devices; a reverse voltage pulse can be employed to allow charge to be de-trapped²⁵⁹.

An important factor that affects the lifetime is the encapsulation. An organic light-emitting device exposed to air is degraded in hours due to the oxidation- an encapsulation in an inert atmosphere has to be used in order to protect the device from oxygen and humidity diffusing into the layers. The drawback of efficient encapsulation is the increased weight and the reduced flexibility of the device.

Brightness

The operation of an organic light-emitting device is mainly observable through the reduction of light intensity as a function of operation time, the higher brightness leads to the faster intensity reduction. The brightness level is inversely proportional to the lifetime. For organic light-emitting devices, the lifetime is strongly linked to the power efficiency and thus to brightness level- high brightness yields in a deteriorated lifetime and vice versa depending on the current density. The achievable brightness level from an OLEDs have been reported to have the lifetime of more than 100,000 hours when producing a luminance of 100 cd/m² which is equal to a desktop monitor²⁵⁸.

The difference of LEECs compared to conventional organic light-emitting diodes (OLEDs) is a high brightness at very low operating voltages broadly independent of the work functions of the electrodes²⁶⁰.

However, due to the electrochemical nature of operation, the operating voltage is limited to the window of electrochemical stability of the materials used in the device. This is a limiting factor in the maximum brightness that can be achieved with LEECs²⁶¹.

In Ru(bpy)₃²⁺-based devices the highest brightness reported was 400 cd/m² in blends with PMMA at 3V.42 However, higher brightness was achieved at higher operating voltages at the expense of the device stability and efficiency²⁶².

Luminescent efficiency

In accordance with Snell's law, when light passes from a medium of high refractive index to one of lower index, there exists a critical angle of incidence, the angle between the light propagation direction and the perpendicular to the surface,

beyond which the light is totally internally reflected. Thus, a great deal of the light generated by an organic light-emitting device is trapped inside and waveguided out to the sides; this is normally about 80% of the total.

The efficiency of an organic light-emitting device is also affected by several factors. The degree of balance of charge carriers injection, the efficiency of recombination, and the efficiency with which the excited state emits light, the photoluminescence efficiency²⁶³. Recombination efficiency is generally at or near unity if two charges are guaranteed to annihilate. However, if the annihilation process has no quenching, then quantum spin statistics dictate that only 25% of the resulting excited states will be useful emissive ones if the state has a singlet multiplicity.^{264,265}

Although emission from the triplet state is spin forbidden in ordinary organic molecules, the emission from transformation enabled by transition metal complexes containing at least one atom of higher atomic weight, which facilitates the triplet-singlet interchange called intersystem crossing.^{266,267,268}

In OLED, the conjugated polymers are considered to hold a better quantum efficiency due to the formation of intra-chain singlet excitons²⁶⁹.

In LEECs, because there exists a balanced charge injection, the high efficiency can be achieved. In $\text{Ru}(\text{bpy})_3^{2+}$ -based devices, $\text{Ru}(\text{bpy})_3^{2+}$ complexes show a strong absorption band at 452nm due to a metal to ligand charge transfer transition and the excited triplet state can be populated from an excited singlet state by intersystem crossing.^{270,271} Usually the efficiency of the electroluminescence is proportional to the product of the photoluminescence quantum yield and the efficiency of the production of excited states^{272,273}.

Therefore, these complexes have high external efficiency and make them eminent candidates for application of organic light-emitting devices.

Power efficiency

The fundamental quantity important to the user is power efficiency, since this determines how long the battery will last in a portable device. The definition of power efficiency is the ratio between the power and the amount of emitted light. For organic light-emitting devices, the power efficiency is of great concern due to that an improved efficiency leads to a better lifetime. The power efficiency is similar to the external quantum efficiency. The external efficiency includes the internal efficiency but also takes the factors such as light emission from the side of

the device and internal refraction into consideration. Internal quantum efficiency is defined as the amount of emitted photons in comparison to the amount of electrons injected into the emitting layer. The internal quantum efficiency for organic light-emitting devices depends on the electron-hole recombination in the emitting layer, where an increased amount of recombination leads to a better efficiency. It is therefore important to choose a material with good recombination property.

Power efficiency is measured in lumens per watt. The lumen is a measure of luminous power, scaled to the sensitivity of the human eye; thus there are more lumens per watt at the sensitivity peak of 555nm than at a wavelength in either the red or blue region. Incandescent light bulbs used in the home range from about 10-15 lumens/watts; fluorescent bulbs can be as much as 80. Currently the best OLEDs are achieving in excess of 20 lumens/watt, for green, although many devices are well below this, often only a few lumens/watt²⁷⁴.

Progress in improving this number has been rapid during the last few years and will doubtlessly continue; in fact, while it is a long range goal, the use of organic light-emitting devices for general illumination may be proved feasible.

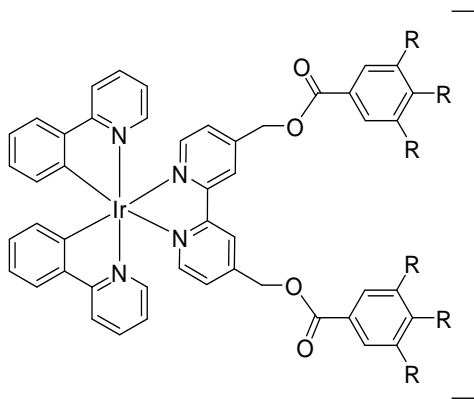
Power efficiency is affected not only by the external quantum efficiency of the device, number of photons out per electron in, but also by the voltage at which the device operates. According to Ohm's law, power is the product of current and voltage. Thus, it is important to obtain low operating voltage which is related to the charge injection barrier. Low voltage is also desirable to provide compatibility with batteries. Voltages for the systems likely to see early application are around 3-6 Volts.²⁷⁵

To summarize, there are several important features that distinguish LECs from conventional OLEDs:

- (1) The "turn-on" voltage of LECs is close to the optical gap and is only very weakly dependent on the film thickness.*
- (2) The quantum efficiencies of LECs do not depend on the electrode work-function.*
- (3) LECs exhibit symmetrical current-voltage and light-voltage characteristics*
- (4) In the operation mechanism, the difference results from the mobile ions present in LEECs and their redistribution during the device operation²⁷⁶.*

4.3 Materials

New cationic Ir(III) materials of general formula $[\text{Ir}(\text{ppy})_2(\text{C}_n\text{bpy})] \text{PF}_6$ {H(ppy) = 2-phenylpyridine; $\text{C}_n\text{-bpy}$ = 3,4,5-R-4,4'-benzoyloxymethyl-2,2'-bipyridine; $n = 8$, $\text{R} = \text{OC}_8\text{H}_{17}$ } were synthesized in CEMIF.CAL laboratories and were used for a



$\text{R} = \text{OC}_8\text{H}_{17}$ $[\text{Ir}(\text{ppy})_2(\text{C}_8\text{-bpy})]\text{PF}_6$

LEEC prototype construction with ITO/Titania electrode²⁷⁷. **Figure left.**

These new materials show liquid-crystalline behaviour and high luminescence²⁷⁸

To reach the necessary experience and improve the method in the LEEC fabrication, and also to test the

appropriate equipments to realize and investigate these new devices, a first LEEC sample, with Ru(II) complex, was fabricated, in order also to compare our results with those shown in literature.

Treated substrates

In addition to polymer materials development, there have been improvements in the injection of carriers at contacts. Poor injection from contacts results in inefficient devices due to the higher drive voltage required to attain a given current and the increased likelihood that the electron and hole currents are imbalanced. Such an imbalance reduces efficiency because it implies that one charge carrier is hopping all the way to the opposite electrode without forming a potentially light-emitting exciton.

Conducting polymers such as PEDOT:PSS (poly(3,4-ethylenedioxythiophene): polystyrene sulfonate) have a Fermi level between that of ITO and the polymer HOMO and thus greatly improve hole injection²⁷⁹. Thin PEDOT films have been shown to reduce sensitivity to ITO treatment and balance the injection of carriers, resulting in overall improvements in efficiency and yield. (PEDOT-PSS)-coated indium tin oxide (ITO) glass was spun at 1500 rpm).

Indium-tin oxide (ITO)-covered glass ($\sim 20\Omega\text{cm}$, Delta Technologies) was thoroughly cleaned before device preparation by sonication, first in acetone for 15

min, then for 20 min in a 20-30% (v/v) solution of acetonitrile in highly pure Millipore water at ~60 °C, followed by several rinsing/sonication steps with pure water at room temperature to remove traces of acetonitrile, and dried under a stream of pure nitrogen.

Research in lighting devices continues to generate considerable interest in all its aspects, i.e. cathode performance. Nanocrystalline metal oxides, such as TiO₂ films, are known to be good electron-transporting materials and are attractive materials for the development of electronic devices. Benefits of these materials include their mechanical and electrical robustness, low cost, visible transparency, excellent stability, ease of fabrication, solution processability, and the potential that exists for controlling their film morphology and interface structure at the micrometer to nanometer length scale employing well-established synthetic routes²⁸⁰. Furthermore, these high-surface-area mesoporous films can be modified by the attachment of molecular dyes, polymers, or biomolecules.

Device top contact

The effects of various top and bottom electrodes on [Ru(bpy)₃]²⁺(PF₆)₂-device performance were studied by *Gorodetsky et al.*²⁸¹. Top electrode was composed of gold, layers, and bottom contact was indium–tin oxide (ITO). As studied by *Costa et al.*²⁸⁰, under forward bias, with the bottom electrode wired as the anode, the steady-state device characteristics were independent of the electrodes used. For devices having an ITO anode, cathode of Au gave identical currents and radiant fluxes, taking into account the differences in reflectivities of the electrodes. These results were interpreted by Costa and co-workers as a consequence of the ionic space-charge effects, the (PF₆)⁻ ions redistribute in each case to effectively inject both holes and electrons. However, this was not the case under reverse bias. For a device having an Au top contact, reversed-bias operation yielded slower turn-on times. Therefore the Costa and collaborators work demonstrated that, for [Ru(bpy)₃]²⁺(PF₆)₂, air-stable electrodes are sufficient for efficient device operation.

4.3.1 Active Layer

Transition metal complexes have emerged as some of the most promising materials for efficient solid-state electroluminescent materials²⁸².

Motivated by the high efficiencies achieved in solution (which approach 25%)²⁸³, a variety of small molecules and polymers have been synthesized and evaluated in solid-state electroluminescent devices. Early attempts led to efficiencies that were fairly low, typically below 0.1%.^{279(a-e)}

Recently, however, *Handy et al.*^{279(f-j)} showed that efficiencies of the order of 1% can be achieved in single layer devices made from $[\text{Ru}(\text{bpy})_3]^{2+}$, where bpy is 2,2'-bipyridine. Further progress was achieved by dilution of this material into polymer matrices, which led to devices with efficiencies of up to 3%^{279(r-s)}, approaching the photoluminescence efficiency. $[\text{Ru}(\text{bpy})_3]^{2+}$ and related complexes carry a net 2+ charge and are compensated by negative counterions such as PF_6^- .²⁸⁴

However, a very long turn-on time of several hundred hours is indicative of a low ionic mobility in the emissive thin film. To speed up the occurrence of the electroluminescence, a higher ratio of ionic liquid in the active layer would help²⁸⁵, or several short high-voltage pulses can be applied²⁸⁶, or also a judicious choice of the counterions can be reduced the turn-on time to a few seconds.^{279(j-s)}

Current-voltage and capacitance-voltage measurements indicated an increase in capacitance at the voltage associated with the onset of current and light emission. This increase was larger for device films with BF_4^{2-} and ClO_4^{2-} counterions versus PF_6^{2-} . Transient measurements also revealed that the smaller counterions of BF_4^{2-} and ClO_4^{2-} gave rise to a faster drop in film resistance and increase in capacitance upon DC driving than did PF_6^{2-} . However smaller counterions also negatively influence lifetime.^{287,288,289,290}

$\text{Ru}(\text{bpy})_3(\text{ClO}_4)_2$ was prepared by a metathesis reaction between commercial $\text{Ru}(\text{bpy})_3\text{Cl}_2$ (Aldrich) and excess sodium perchlorate. $\text{Ru}(\text{bpy})_3(\text{PF}_6)_2$ were prepared using similar procedures with the appropriate sodium or ammonium salts. The resulting crystals were recrystallized from acetonitrile/benzene and dried under vacuum at $\sim 100^\circ\text{C}$ for several hours.

The Ionic Liquid used was 1-Butyl-3-methylimidazolium hexafluorophosphate ($\text{BMIM}^+[\text{PF}_6^-]$). Compared to the device without IL, which shows a ton of 11.5 h, all the devices containing ILs are more than 1 order of magnitude, in fact 1 iMTC (ionic metal-transition complex): 1 IL results in a turn-on time $t_{\text{on}} = 3.5$ min.²⁹¹. The IL increases the average distance between the iTMC cations (density of the

mobile ions) decreasing the self-quenching of the emission, therefore increase of the device luminance and efficiency.

Mechanism

The $\text{Ru}(\text{bpy})_3^{2+}$ LEECs and the mechanism of electroluminescence (EL) is based on recombination of $\text{Ru}(\text{bpy})_3^{3+}$ (holes) and $\text{Ru}(\text{bpy})_2(\text{bpy}^-)^+$ (electrons) species leading to the appearance of the $\text{Ru}(\text{bpy})_3^{2+*}$ excited state, followed by light emission with a maximum around 660 nm.

$\text{Ru}(\text{bpy})_3$ solutions in acetonitrile were always filtered through 0.2 μm syringe filters before use. In general, the $\text{Ru}(\text{bpy})_3$ films (~100 nm) were spin-coated from a 4% (m/v) acetonitrile (Aldrich) solution at 2000 rpm, onto clean PEDOT:PSS/ITO-covered glass. After spin-coating, the device was dried under vacuum for at least 6 h at 120 °C.

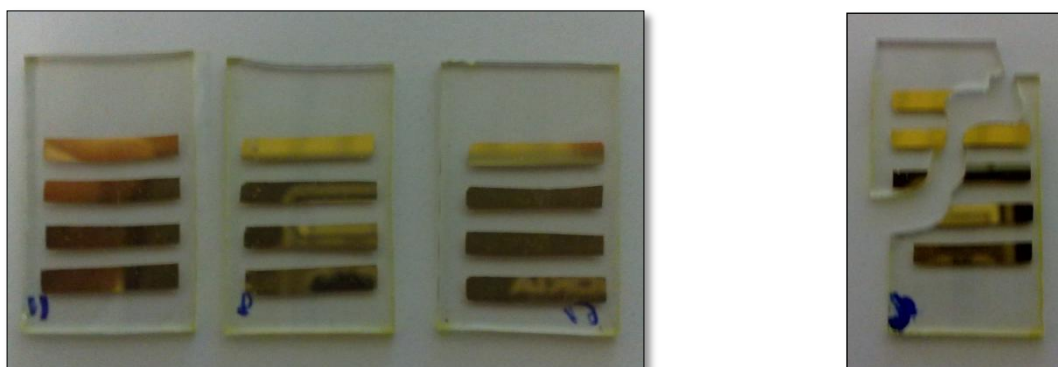


Figure 4.2.

LEECs realized with $\text{Ru}(\text{bpy})_3$ complex on the left.

LEEC broken after preliminary measurements, its damage was probably due to a not good film deposition.

Chapter 5.

The results obtained along the above described experimental work have been collected in Papers and Communications at national or international meetings.

5.1 Luminescent mesostructured material: results

The results obtained from the investigations described in Chapter 2 are summarized in the following Paper and Communications.

5.1.1 Paper

Self-incorporation of a luminescent neutral iridium(III) complex in different mesoporous micelle-templated silicas

Daniela Aiello,^a Anna Maria Talarico,^b Francesca Teocoli,^b Elisabeta I. Szerb,^b Iolinda Aiello,^b Flaviano Testa^a and Mauro Ghedini^{a,b}

Received (in Victoria, Australia) 7th July 2010, Accepted 21st September 2010
DOI: 10.1039/c0nj00533a

The neutral luminescent tris-cyclometallated 2-phenylpyridine iridium(III) complex, (*fac*-Ir(ppy)₃), [Ir] following a self-assembling procedure, has been successfully located in the cavities of mesostructured silica materials through a surfactant-mediated process. Two different structure-directing agents, the cationic cetyltrimethyl ammonium bromide (CTAB) and the non-ionic poly(ethylene glycol)-*block*-poly(propylene glycol)-*block*-poly(ethylene glycol) (P123) were tested. The structural features induced by the metal complex incorporation can be explained by comparing the newly synthesized hybrid mesostructured materials with the corresponding undoped samples which were similarly prepared. X-Ray powder diffraction (XRD), nitrogen sorption, scanning electron microscopy (SEM), thermogravimetric analysis (TGA) and UV-Vis spectroscopy were used to characterize the investigated materials. Medium-sized spherical particles of 800 nm were obtained using CTAB as a structure-directing agent whereas larger monolithic aggregates with a minimum dimension of 5–8 μm were obtained using P123. The new hybrids showed the typical hexagonal symmetry of analogously prepared materials. Moreover high luminescence quantum yield values were obtained for both hybrids as a result of a very good dispersion of the chromophore in the mesostructured matrices, thereby avoiding dramatic self-quenching phenomena. The approach described in this paper provides a simple synthetic way to prepare new luminescent silica-based materials by the inclusion of neutral metal-containing luminophores into the pores of a mesoporous hosting skeleton.

Introduction

An important topic in photonic nanocomposite materials science is the design and synthesis of functional materials, which simultaneously allow satisfaction of the whole set of characteristics required to achieve specific optical properties and performances.

Currently, ordered mesostructured materials, prepared by the co-condensation of an appropriate inorganic source and the surfactant self-assembling species doped with an optically active compound, have attracted a great deal of interest for potential optical applications such as, for example, high sensitive sensors,^{1–4} optical switches,^{5,6} solar cells,⁷ frequency doublers,⁸ and solid-state laser materials.⁹

Mesostructured materials with a geometrically regular inorganic skeleton have been shown to be appropriate scaffolds for the confinement of dyes.^{10–13} Since several dyes undergo luminescence quenching phenomena at relatively high concentrations, preventing advantageous applications, a possible way to overcome this drawback is given by the mesostructured materials,

i.e., materials in which the organic template is not removed from the cavities resulting from the synthetic process adopted. These materials present well-defined organic–inorganic phase segregation at the nanometre scale which may effectively prevent aggregation and the related luminescence quenching phenomena. Moreover, it is worth recalling further excellent advantages, such as increased mechanical stability and shielding of the incorporated dye against chemical, thermal or photochemical degradation provided by the scaffold itself.

The chemistry of cyclometallated iridium(III) complexes is a current topic of investigations because they display unique photophysical properties such as good photo- and thermal stability, high phosphorescence quantum efficiencies, relatively short lifetimes and simple colour tuning through ligand structure and control, and a set of key features for molecular-based light emitting devices applications.^{14–18} However, it is also noteworthy that the actual performances of these molecular materials can be often severely limited because of the reduced emission efficiency in the solid state, owing to a concentration-driven quenching.¹⁹

Although different approaches, such as the dispersion of the emitters in a polymeric matrix or the introduction of sterically hindered substituents in the auxiliary ligands^{20,21} have been explored to limit the concentration quenching effect, at present none of them seem to solve this problem satisfactorily. In this context, mesostructured materials can be a useful tool for the dispersion of the emitting iridium(III) complexes thus obtaining better performing iridium(III)-based luminescent materials.

^a Centro di Eccellenza CEMIF.CAL, CR INSTM, Unità INSTM della Calabria, Dipartimento di Ingegneria Chimica e dei Materiali, 87036 Arcavacata di Rende (CS), Italy
^b Centro di Eccellenza CEMIF.CAL, LASCAMM – CR INSTM, Unità INSTM della Calabria and LiCryl, CNR-INFN, Dipartimento di Chimica, Università della Calabria, 87036 Arcavacata di Rende (CS), Italy.
E-mail: m.ghedini@unicat.it; Fax: +39 984 492066; Tel: +39 984 492062

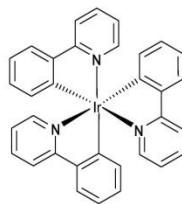


Fig. 1 Chemical structure of **[Ir]**.

In fact, a homoleptic tris-cyclometallated iridium(III) surfactant has been recently employed in the synthesis of an amphiphile/silica co-assembled nanocomposite which was successfully used as an active layer for organic light-emitting diode. This provided a better performing device with respect to the one based on the pristine solid.²²

In this paper, selected as representative of neutral cyclometallated iridium(III) emitters, the synthesis, characterization and photophysical properties of new hybrid mesostructured silica materials incorporating the highly luminescent *fac*-isomer of the neutral homoleptic tris-cyclometallated 2-phenylpyridine iridium(III) complex,²³ *fac*-Ir(ppy)₃ where Hppy = 2-phenylpyridine, which will then be labelled as **[Ir]** (Fig. 1), are reported.

The new materials described and discussed herein are obtained by a one-step procedure, similar to that developed by Zhou and Honma²⁴, co-assembling the neutral luminescent **[Ir]** complex with a surfactant, which acts as the structure-directing agent, and tetraethoxysilane (TEOS) as an inorganic source. The selected surfactants are the cationic cetyltrimethyl ammonium bromide (CTAB) and the non-ionic triblock copolymer poly(ethylene glycol)-*block*-poly(propylene glycol)-*block*-poly(ethylene glycol) (P123). Moreover, because of the negligible solubility of **[Ir]** in H₂O, EtOH has been used as co-solvent in order to increase, at least slightly, the **[Ir]** solubility and facilitate its inclusion within the hydrophobic regions of the surfactant during the template self-assembly process.

The silica-based luminescent materials prepared according to the above summarized procedure, with the general formula SiO₂(**[Ir]**-CTAB) and SiO₂(**[Ir]**-P123), were structurally and photophysically investigated. The differences induced by (i) the nature of the reacted surfactant with respect to the neutral character of **[Ir]**, (ii) the resulting structural differences induced by the use of ethanol as co-solvent in the synthetic procedure and (iii) the resulting structural differences induced by the introduction of the **[Ir]** luminescent complex will be discussed.

Experimental

Materials

Tetraethyl orthosilicate (TEOS, 98%), ammonium hydroxide (NH₄OH, 29 wt% NH₃ in water), poly(ethylene glycol)-*block*-poly(propylene glycol)-*block*-poly(ethylene glycol) (P123), hydrochloric acid (HCl 37%), and absolute ethanol (EtOH, 99.98%) were used as supplied by Sigma-Aldrich. Cetyltrimethyl ammonium bromide (CTAB, 99.8 wt%) was purchased from Alfa Aesar. Water was produced from a Milli-Q system.

fac-Ir(ppy)₃, **[Ir]**, was synthesized according to the procedure reported in the literature.²⁵

Methods used for characterization

Low angle X-ray diffraction (XRD) measurements were performed in the 2θ range of 1.0°–10.0° using a Philips 1730/10 diffractometer using Cu K α radiation ($\lambda = 1.5416 \text{ \AA}$) at 40 kV and 200 mA and at a step width of 0.005°. Nitrogen sorption isotherms were measured at 77 K on a Micromeritics ASAP 2010 porosimeter. The materials were outgassed for 12 h under vacuum at 423 K before the measurements. Specific surface areas were calculated by the Brunauer–Emmett–Teller (BET) method and pore sizes by the Barrett–Joyner–Halenda (BJH) method.^{26,27} Scanning electron microscopy images (SEM) were obtained with FEI FP 2353/OX. The thermogravimetric analysis (TGA) was carried out between 298 K and 1093 K under airflow and at a heating rate of 10 K min⁻¹ in a Perkin Elmer thermobalance. Infrared spectra (FT-IR) were recorded on KBr pellets using a Perkin Elmer Spectrum One FT-IR spectrophotometer. Steady-state emission spectra were recorded on a Horiba Jobin Yvon Fluorolog 3 spectrofluorimeter, equipped with a Hamamatsu R-928 photomultiplier tube. The emission quantum yields (Φ) of the samples were obtained by means of a 102 mm diameter integrating sphere coated with Spectralon[®] and mounted in the optical path of the spectrofluorimeter using a 450 W Xenon lamp as an excitation source, coupled with a double-grating monochromator for selecting wavelengths. Φ is a ratio between “number of photons emitted” and the “number of photons absorbed”. The number of photons absorbed was calculated by monitoring the scattered excitation peak first with the blank sample in the sphere (L_a) and then with the sample in the sphere (L_c). The differences in peak intensity between these two measurements are caused by sample absorption and thus the number of absorbed photons can be calculated as the differences of the integrated curves ($L_a - L_c$). The number of photons emitted is calculated as the difference between the integrated luminescence of the sample (E_c) and that of the blank (E_a) and is therefore ($E_c - E_a$). As a result, $\Phi = (E_c - E_a)/(L_a - L_c)$. The experimental uncertainty on the Φ was 5%. In particular, mesostructured SiO₂(CTAB) and SiO₂(P123) were used as blank samples for the determination of Φ of SiO₂(**[Ir]**-CTAB) and SiO₂(**[Ir]**-P123), respectively. Time-resolved measurements were performed using the time-correlated single-photon counting (TCSPC) option on the Fluorolog 3. NanoLED at 370 nm, fwhm < 200 ps, was used to excite the sample. Excitation sources were mounted directly on the sample chamber at 90° to a single-grating emission monochromator (2.1 nm mm⁻¹ dispersion; 1200 grooves mm⁻¹) and collected with a TBX-04-D single-photon-counting detector. The photons collected at the detector were correlated by a time-to-amplitude converter (TAC) to the excitation pulse. Signals were collected using an IBH Data Station Hub photon counting module and data analysis was performed using the commercially available DAS6 software (HORIBA Jobin Yvon IBH). Goodness of fit was assessed by minimizing the reduced Chi squared function (χ^2) and visual inspection of the weighted residuals. The average lifetimes were calculated as $\langle \tau \rangle = \sum_i (A_i \tau_i) / \sum_i A_i$.

Synthesis

Preparation of mesostructured blank $\text{SiO}_2(\text{CTAB})$. $\text{SiO}_2(\text{CTAB})$ was prepared using a procedure similar to the one described in the literature.²⁸ Molar composition: 1 TEOS:0.3 CTAB:3.8 NH_4OH :1.53 H_2O :17.1 EtOH. The template solution was prepared by dissolving 1.09 g (0.003 mol) of CTAB in 10 mL (0.171 mol) of EtOH under magnetic stirring. Then, 27.5 mL (1.53 mol) of H_2O and 2.49 mL (0.038 mol) of NH_4OH were added to this solution. After 5 min, 2.21 mL (0.01 mol) of TEOS was added under rapid stirring. The mixture was stirred for 3 days at room temperature, then filtered, washed with H_2O and dried at 343 K overnight.

Preparation of mesostructured blank $\text{SiO}_2(\text{P123})$. $\text{SiO}_2(\text{P123})$ was prepared adapting the procedure described in the literature.²⁹ Molar composition: 1 TEOS:0.0174 P123:6 HCl:1.67 H_2O :17.1 EtOH. 1 g (1.74×10^{-5} mol) of P123 was dissolved in 10 mL (0.171 mol) of EtOH, under vigorous stirring at room temperature. Then, 30 mL (1.67 mol) of H_2O and 1.83 mL (0.060 mol) of HCl were added to the solution. Finally, 2.21 mL (0.01 mol) of TEOS was added under stirring. The resulting mixture was aged at 373 K for 24 h, then filtered, washed with H_2O and dried at 333 K for 12 h.

Preparation of mesostructured hybrid, $\text{SiO}_2(\text{Ir}-\text{CTAB})$. Molar ratio: 1 TEOS:0.3 CTAB:3.8 NH_4OH :1.53 H_2O :17.1 EtOH:0.0016 [Ir]. CTAB (1.09 g, 0.003 mol) was dissolved in 10 mL (0.171 mol) of EtOH; [Ir] (0.01 g, 1.6×10^{-5} mol) was added to the reaction mixture, which was stirred at room temperature for 5 h. The obtained yellow suspension was filtered to remove the solid (mixture of undissolved [Ir] and CTAB). Then 27.5 mL (1.53 mol) of H_2O and 2.49 mL (0.038 mol) of NH_4OH were added to the resulting solution. After 5 min, 2.21 mL (0.01 mol) of TEOS was added under vigorous stirring. The mixture was stirred for 3 days at room temperature, then filtered, washed with H_2O and dried at 343 K overnight.

Preparation of $\text{SiO}_2(\text{Ir}-\text{P123})$. Molar composition: 1 TEOS:0.0174 P123:6 HCl:1.67 H_2O :17.1 EtOH:0.0016 [Ir]. An ethanolic solution (10 mL, 0.171 mol) of P123 (1 g, 1.74×10^{-5} mol) was obtained under vigorous stirring. Then, 0.01 g (1.6×10^{-5} mol) of [Ir] was added. The resulting mixture was stirred at room temperature for 5 h. Then the solid product (mixture of undissolved [Ir] and P123) was filtered and 30 mL (1.67 mol) of H_2O and 1.83 mL (0.060 mol) of HCl were added to the solution. Finally, 2.21 mL (0.01 mol) of TEOS was added while stirring at room temperature. The mixture was aged at 373 K for 24 h, then filtered, washed with H_2O and dried at 333 K for 12 h.

Template extraction. Surfactant removal was performed using a chemical extraction with solvent. In particular, for the materials obtained with CTAB as a template directing agent, EtOH (300 mL) and HCl (25 mL) were added to 1 g of the respective solids, $\text{SiO}_2(\text{CTAB})$ and $\text{SiO}_2(\text{Ir}-\text{CTAB})$. The mixtures were subsequently stirred for 6 h at reflux. The resulted inorganic scaffolds, named $\text{SiO}_2(\text{CTAB})^*$ and $\text{SiO}_2(\text{Ir}-\text{CTAB})^*$, respectively, were dried at 343 K overnight.

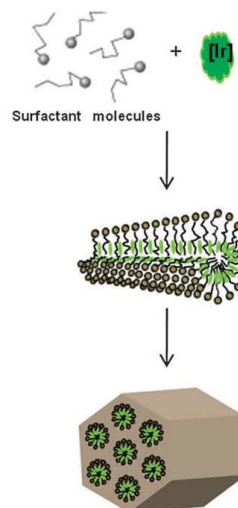
For the other mesostructured materials, $\text{SiO}_2(\text{P123})$ and $\text{SiO}_2(\text{Ir}-\text{P123})$, the removal of the neutral surfactant P123 was carried out *via* chemical extraction using only EtOH (300 mL), which was added to 1 g of solid sample. The resulting mixture was stirred for 6 h at reflux. The obtained solids, abbreviated in a similar way to the other extracted materials, $\text{SiO}_2(\text{P123})^*$ and $\text{SiO}_2(\text{Ir}-\text{P123})^*$, respectively, were dried at 343 K overnight.

Results and discussion

Synthesis

The new mesostructured hybrid materials containing the luminescent neutral iridium(III) chromophore, $\text{SiO}_2(\text{Ir}-\text{CTAB})$ and $\text{SiO}_2(\text{Ir}-\text{P123})$ were synthesized using a one-pot procedure, *via* a modified synthetic strategy. In particular, the chromophore [Ir] was incorporated into the micelles formed by two different types of surfactants (cationic CTAB and non-ionic P123), using a $\text{H}_2\text{O}/\text{EtOH}$ mix solvent system, which furthermore acts as structure-directing agents for the synthesis of the final hybrid materials (Scheme 1). In order to investigate the differences induced by the use of ethanol as co-solvent, their analogous blank materials without the luminescent chromophore, $\text{SiO}_2(\text{CTAB})$ and $\text{SiO}_2(\text{P123})$ were also prepared, characterised and discussed with reference to those reported in the literature.^{28,29}

Furthermore, to investigate the surface properties after the inclusion of the luminescent iridium(III) chromophore, the porosity producing templates were completely removed (FT-IR evidences) by extraction with specific solvents. Comparison of the two types of extracted solids, blanks and hybrids was useful for understanding the surface effects in terms of diameters and pore volumes.



Scheme 1 A possible schematic illustration of [Ir] incorporation into the mesostructured silica materials.

X-Ray diffraction investigations (XRD)

The XRD patterns of all the synthesized mesostructured materials (hybrids and blanks) were recorded (Fig. 2). Both $\text{SiO}_2(\text{CTAB})$ and $\text{SiO}_2(\text{[Ir]}\cdot\text{CTAB})$ exhibit XRD patterns similar to the ones reported in the literature for analogous systems.²⁸ In particular, the patterns consist of small angle of three relatively broad reflections indexed as [100], [110] and [200], characteristic of a hexagonal lattice.

Similar interplanar distances d_{100} , and consequently the similar hexagonal lattice constant a (Fig. 2a) indicate that the presence of [Ir] did not affect the self-assembly process during mesophase formation, leaving the mesostructure substantially unchanged. This phenomenon can be explained by the fact that the chromophore was introduced between the hydrophobic tails of the CTAB surfactant in a periodical manner within a mesostructured channel.³⁰ However, the decrease in the intensity of the diffraction peaks, in the case of the hybrid material $\text{SiO}_2(\text{[Ir]}\cdot\text{CTAB})$, may be indicative of a more disorganized material compared with the blank one. In addition both mesostructured materials containing CTAB showed a shrinkage of the d spacings typically observed when, instead of pure H_2O , a $\text{H}_2\text{O}/\text{EtOH}$ mixture is employed in the synthesis.²⁸

The XRD patterns of the $\text{SiO}_2(\text{P123})$ and $\text{SiO}_2(\text{[Ir]}\cdot\text{P123})$ samples (Fig. 2b) consisted of four peaks that can be indexed as [100], [110], [200] and [210] associated with a hexagonal symmetry. These patterns are similar to the ones exhibited by the analogues P123-template materials reported in the literature,²⁹ with an expected shrinkage of the cell parameters because of the use of EtOH as co-solvent.²⁸ Nevertheless the $\text{SiO}_2(\text{[Ir]}\cdot\text{P123})$ sample shows an increase in the interplanar distance and hexagonal unit cell length with respect to the $\text{SiO}_2(\text{P123})$ blank (Fig. 2b). This may be indicative of the placement of the [Ir] complex within the interior of the micellar aggregates, which consequently expands the micelles size.³⁰ Furthermore, contrary to systems containing the CTAB surfactant, the inclusion of the iridium(III) complex seems to enhance slightly the order parameter of the hybrid material $\text{SiO}_2(\text{[Ir]}\cdot\text{P123})$, as the increase in the intensity of the reflection peaks indicated when the patterns are compared with the blank $\text{SiO}_2(\text{P123})$.

No significant changes were observed for the XRD patterns recorded several weeks later for both CTAB and P123-template materials stored in air, indicating that these structures were very stable.

Nitrogen sorption

The specific surface areas (S_{BET}), pore diameters (d_p) and pore volume (V_p) of all prepared materials were calculated by the BET method and BJH model, respectively (Table 1).

The adsorption/desorption isotherms of $\text{SiO}_2(\text{CTAB})^*$, $\text{SiO}_2(\text{[Ir]}\cdot\text{CTAB})^*$, $\text{SiO}_2(\text{P123})^*$ and $\text{SiO}_2(\text{[Ir]}\cdot\text{P123})^*$ are shown in Fig. 3 and Fig. 4.

The isotherms of all the extracted samples are type IV according to the IUPAC classification, and typical of mesoporous materials with uniform size distribution. The porosimetric values d_p , S_{BET} , and V_p determined for all the extracted samples are coherent with that obtained for analogously synthesized materials.^{28,29} Nevertheless the values measured for $\text{SiO}_2(\text{[Ir]}\cdot\text{CTAB})^*$ and $\text{SiO}_2(\text{[Ir]}\cdot\text{P123})^*$ samples, including d_p and V_p , are slightly increased with respect to the corresponding blank ones. Therefore, it is reasonable to assume that the self-inclusion of [Ir] inside the micelles during the co-assembly process affects their dimensions, thus leading to an enlargement of the resulting pore size and pore volume.

Scanning electron microscopy (SEM)

Fig. 5 shows representative SEM micrographs of the [Ir] solid. In the solid state this luminescent complex forms long fibres with a hexagonal section and medium diameter of 2–5 μm .

Fig. 6a–d shows SEM micrographs of all mesostructured materials synthesised. The solids exhibit very different

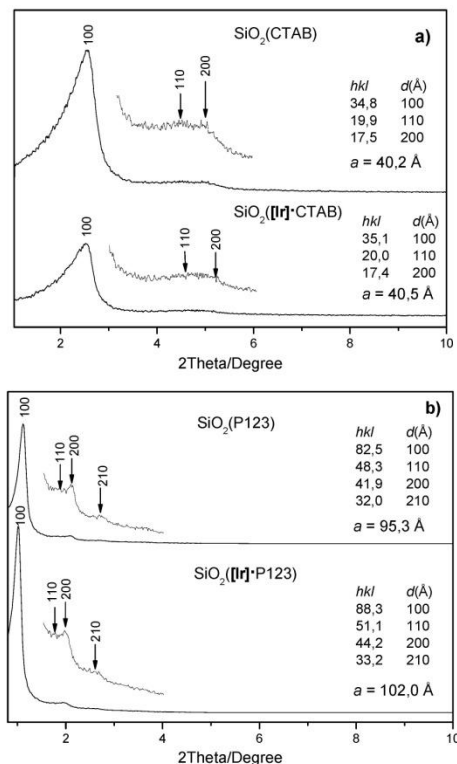


Fig. 2 XRD patterns of (a) $\text{SiO}_2(\text{CTAB})$ top and $\text{SiO}_2(\text{[Ir]}\cdot\text{CTAB})$ bottom; (b) top— $\text{SiO}_2(\text{P123})$ and bottom— $\text{SiO}_2(\text{[Ir]}\cdot\text{P123})$.

Table 1 Physicochemical parameters of mesoporous silica materials derived from nitrogen sorption measurements

Materials	$S_{\text{BET}}^a/\text{m}^2 \text{g}^{-1}$	d_p^b/nm	$V_p/\text{cm}^3 \text{g}^{-1}$
$\text{SiO}_2(\text{CTAB})^*$	1240	3.1	0.92
$\text{SiO}_2(\text{[Ir]}\cdot\text{CTAB})^*$	1002	3.4	0.98
$\text{SiO}_2(\text{P123})^*$	794	3.6	0.68
$\text{SiO}_2(\text{[Ir]}\cdot\text{P123})^*$	738	4.0	0.79

^a Determined using the BET. ^b Determined by the BJH algorithm using the absorption branch.

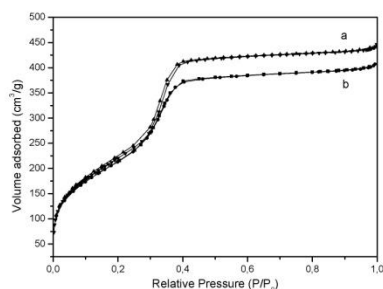


Fig. 3 Nitrogen adsorption and desorption isotherms for (a) $\text{SiO}_2(\text{CTAB})^*$ and (b) $\text{SiO}_2([\text{Ir}]\text{-CTAB})^*$.

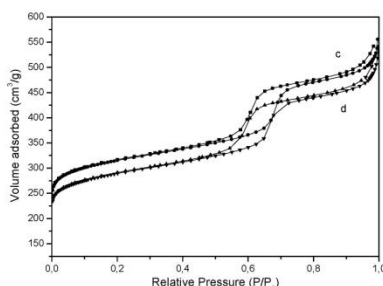


Fig. 4 Nitrogen adsorption and desorption isotherms for (c) $\text{SiO}_2(\text{P123})^*$ and (d) $\text{SiO}_2([\text{Ir}]\text{-P123})^*$.

morphologies. Syntheses using H_2O and EtOH as co-solvent permit spherical particles with ordered mesopores to be obtained. In fact, $\text{SiO}_2(\text{CTAB})$ as $\text{SiO}_2([\text{Ir}]\text{-CTAB})$ (Fig. 6a and b) consists of medium-sized spherical particles of 800 nm and a homogeneous size distribution. $\text{SiO}_2(\text{P123})$ as $\text{SiO}_2([\text{Ir}]\text{-P123})$ (Fig. 6c and d) samples exhibits larger and much more monolithic aggregates with a minimum dimension of 5–8 μm .

Thermogravimetric analysis (TGA)

The thermal decomposition behaviour of all mesostructured solids (hybrids and blanks) was studied using TGA measurements.

In the range of 413–873 K, $\text{SiO}_2(\text{CTAB})$ and $\text{SiO}_2(\text{P123})$ samples exhibit a weight loss attributed to a surfactant

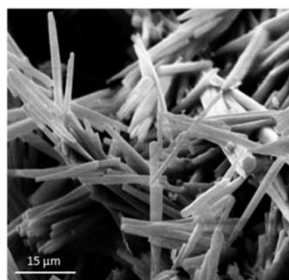


Fig. 5 Representative SEM image of $[\text{Ir}]$.

decomposition of 44.8% and 36.5% respectively. In the same temperature range, $\text{SiO}_2([\text{Ir}]\text{-CTAB})$ and $\text{SiO}_2([\text{Ir}]\text{-P123})$ samples exhibit a weight loss of about 48.3% and 39.7%, which probably corresponds to the decomposition of $[\text{Ir}]$ together with the surfactant. The similar weight losses indicate similar behaviours despite the different templates used in the synthesis. Nevertheless, the difference of weight loss resulting from a comparison among the blank and the corresponding hybrid materials (approximately 3%) cannot be attributed only to the presence of the $[\text{Ir}]$ chromophore, and it probably arises from both $[\text{Ir}]$ decomposition and an intrinsic difference of the weight ratio between the surfactants and the inorganic scaffold due to a different degree of order induced by the $[\text{Ir}]$ co-assembling process. These results are supported also by XRD measurements and nitrogen sorption analysis, indicating that the presence of $[\text{Ir}]$ in the micelles causes some variations in surface parameters.

Photoluminescence properties

It is well known that for iridium(III) complexes, luminescence quantum yield in the solid state is a function of aggregation. Aggregate formation often quenches light emission limiting the development of photoluminescent materials that exhibit strong solid-state emission properties.³¹ Nevertheless, in some cases, it has been demonstrated that the luminescence quantum yield of iridium(III) complexes in solid states, such as doped polymer films or powder states with suitable supramolecular organization of the chromophores, is higher than that in solutions.³² Specifically in the case of $[\text{Ir}]$, it has been shown that its photoluminescence efficiency can vary from 0.0098 in neat film, to 0.7 in solution, reaching a value of 0.9 in highly dispersed polymeric matrix.³³

In order to investigate the photoluminescence properties of the newly synthesized mesostructured materials, a full photophysical investigation including emission spectra, phosphorescence quantum yield and time-resolved luminescence was performed for comparison of the two hybrid solids and the pristine $[\text{Ir}]$ powder. The full photophysical results compared to the photophysical properties of $[\text{Ir}]$ complex in solution^{33,34} are summarized in Table 2.

In Fig. 7 are reported the emission spectra of the mesostructured powders $\text{SiO}_2([\text{Ir}]\text{-CTAB})$ and $\text{SiO}_2([\text{Ir}]\text{-P123})$ compared to the emission spectra of the $[\text{Ir}]$ powder. With reference to the emission spectra of both $\text{SiO}_2([\text{Ir}]\text{-CTAB})$ and $\text{SiO}_2([\text{Ir}]\text{-P123})$ no red shift of the emission maxima is observed on moving from solution to the two different mesostructured powders whereas a substantial red shift is observed for pristine $[\text{Ir}]$ solid.

Since a significant red shift of the emission maxima is expected for aggregation states which favour the occurrence of a high degree of interchromophore contacts,³⁵ the observed spectral features seem to indicate (i) a substantial absence of strictly interacting iridium(III) moieties in the mesoporous powders as a result of a very good dispersion of the host in the matrices and (ii) the existence of a high degree of interchromophore contact in the pristine solid.

Regarding phosphorescence quantum efficiency, the $[\text{Ir}]$ solid shows considerably reduced phosphorescence quantum

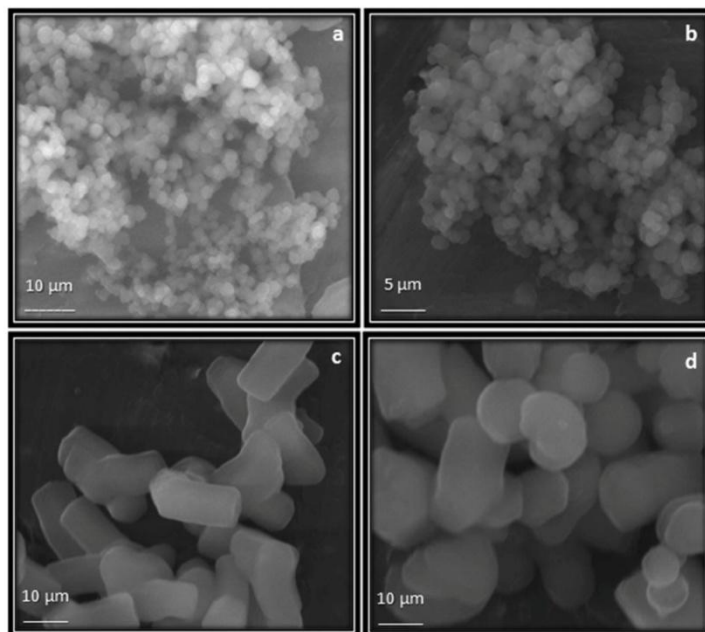


Fig. 6 Representative SEM image of SiO₂(CTAB) (a), SiO₂([Ir]-CTAB) (b), SiO₂(P123) (c) and SiO₂([Ir]-P123) (d).

Table 2 Photoluminescence properties

Materials	$\lambda_{\text{max}}/\text{nm}$	Φ	$\tau_{\text{ph}}/(A_i)$ ns	$\tau_{\text{rad}}/\text{ns}$	$\langle\tau\rangle/\text{ns}$	$\phi_{\text{calc.}}$
[Ir] ^a	515	0.73	1090	1500	—	—
[Ir] ^b	—	0.91	1200	1300	—	—
[Ir] ^c	534	0.012	$\tau_1 = 0.1$ (49%) $\tau_2 = 38$ (50%)	—	19	~0.014
SiO ₂ ([Ir]-CTAB)	509	0.3	$\tau_1 = 576$ (27%) $\tau_2 = 1077$ (72%)	—	931	~0.72
SiO ₂ ([Ir]-P123)	515	0.04	$\tau_1 = 527$ (25%) $\tau_2 = 1120$ (76%)	—	983	~0.75

^a Data concerning [Ir] in deoxygenated toluene solution taken from ref. 33 and 34. ^b Data concerning [Ir] in polystyrene matrix (1 wt%) taken from ref. 33. ^c [Ir] pristine powder.

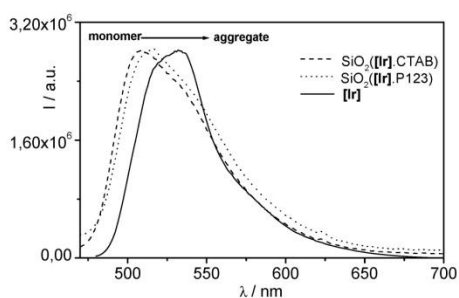


Fig. 7 Emission spectra of SiO₂([Ir]-CTAB) (dash line), SiO₂([Ir]-P123) (dotted line) and of [Ir] pristine powder (solid line).

yield with respect both to solutions and dispersed polymeric matrix (Table 2). Moreover, its luminescence decay turned out to be considerably fast and non-exponential thus indicating the presence of additional non-radiative decay channels caused by aggregation in the solid state.

Differently from the [Ir] solid, SiO₂([Ir]-CTAB) and SiO₂([Ir]-P123) showed much longer luminescence lifetimes, even if still non-exponential. In particular both solids showed a longer lifetime component of ~1100 ns, which account for most of the signal (75%) and a shorter one of ~500 ns accounting for 25% of the total decay.

The longer luminescent lifetime component is comparable with that observed for [Ir] highly dispersed in a polymeric rigid matrix (Table 2) which is usually associated with the lifetime of the isolated rigid molecule. Therefore this component could be

attributed to a large fraction of non-interacting iridium(III) moieties reasonably included in the interior of the micelle cores where the chromophore is preferentially shielded from aggregation and consequently from the luminescence quenching phenomena. Furthermore, the faster lifetime component may result from a fraction of iridium(III) chromophore whose luminescence can be quenched through the exciton migration quenching phenomena between closely packed iridium(III) chromophores and/or iridium chromophores and impurity traps possibly present in the materials.

Phosphorescence quantum yields of SiO₂([Ir]-CTAB) and SiO₂([Ir]-P123) mesostructured solids were determined following the procedure described in the Experimental section. Different results were obtained for the two solids (0.3 and 0.04 respectively) despite the very similar photophysical data derived from both steady state and time-resolved luminescence measurements. Moreover, these values disagree significantly with the value reported for the [Ir] complex dispersed in polystyrene matrix (Table 2) despite the similarity of lifetimes values. Therefore, our measured phosphorescence quantum yields should be affected by instrumental artefacts likely to arise from important light scattering phenomena typical of such materials and affecting substantially the calculated values of absorbed photons. Nevertheless, the phosphorescence quantum yields (ϕ_p) were roughly estimated. When only one type of emitting species is present in the sample, the phosphorescence lifetime (τ_p) and ϕ_p values are related to the radiative lifetime (τ_r) of the emissive state as:

$$\phi_p = \phi_{isc} \left(\frac{\tau_p}{\tau_r} \right)$$

where ϕ_{isc} is the intersystem crossing quantum yield and it is assumed as a unitary value.³⁴

Considering the value reported in the literature for [Ir] dispersed in a polystyrene matrix as the radiative lifetime and the medium values (τ) calculated from experimental data as the phosphorescence lifetime, the phosphorescence quantum yields obtained for SiO₂([Ir]-CTAB) and SiO₂([Ir]-P123) are 0.72 and 0.75, respectively. Moreover, the phosphorescence quantum yield of the [Ir] pristine solid was calculated analogously obtaining a result which was comparable to that measured (Table 2).

The calculated luminescence quantum yield values suggest that the experimental approach (technique, set-up) adopted for their determination suffers from a severe limitation arising from the non-negligible scattering phenomena displayed by the investigated materials. However, the calculated values seem to agree with both XRD and porosimetric results, showing the [Ir] complexes to be mainly included within the interior of the micellar aggregates.

Conclusions

These investigations were made in order to test a synthesis protocol which can be beneficial for the preparation of new emitting materials for optical applications. In particular, in order to evaluate the possible effects induced by the different electrostatic interactions that could take place between the templating agent and the neutral [Ir] compound, mesostructured

materials containing a cationic or a non-ionic surfactant have been prepared. The adopted approach allowed for the incorporation of the [Ir] guest into a mesostructured matrix host by a co-organizing process involving the two selected surfactants: the cationic CTAB and the non-ionic P123. The XRD and nitrogen sorption measurements of the obtained materials evidenced the preferential inclusion of the iridium(III) chromophore into the hydrophobic channels of the mesostructure without any substantial changes to the typical hexagonal symmetry, with respect to both the blank samples and analogous synthesized materials. Nevertheless, XRD measurements showed that when the cationic CTAB is used as a structure directing agent, the [Ir] complex is preferentially placed in between the hydrophobic tails of the surfactants. In contrast, the non-ionic P123 directs the chromophore mainly into the centre of micelle cores.

Moreover, the resultant hybrid materials exhibit the characteristic emission of the [Ir] complex with a high luminescence quantum yield originating from the effective good dispersion of the chromophore within the mesostructured matrices. Further investigations are currently under way in order to extend the described approach to ionic chromophores.

Acknowledgements

The work was supported by the Consorzio Interuniversitario Nazionale per la Scienza e la Tecnologia dei Materiali (INSTM) and the Ministero dell'Istruzione, dell'Università e della Ricerca (MiUR), through the PRISMA 2007 (PC26/2007) and the Progetti di Ricerca di Interesse Nazionale (PRIN 2007-2007WJMF2W).

References

- 1 T. A. Dickinson, J. White, J. S. Kauer and D. R. Walt, *Nature*, 1996, **382**, 697.
- 2 H. Y. Fan, Y. F. Lu, A. Stump, S. T. Reed, T. Baer, R. Schunk, V. Perez-Luna, G. P. Lopez and C. J. Brinker, *Nature*, 2000, **405**, 56.
- 3 G. Wirnsberger, B. J. Scott and G. D. Stucky, *Chem. Commun.*, 2001, 119.
- 4 B. H. Han, I. Manners and M. A. Winnik, *Chem. Mater.*, 2005, **17**, 3160.
- 5 B. Schaudel, C. Guerneur, C. Sanchez, K. Nakatani and J. A. Delaire, *J. Mater. Chem.*, 1997, **7**, 61.
- 6 M. Levitus and P. F. Aramendia, *J. Phys. Chem. B*, 1999, **103**, 1864.
- 7 B. V. Bergeron, C. A. Kelly and G. J. Meyer, *Langmuir*, 2003, **19**, 8389.
- 8 G. Ihlein, B. Junges, U. Junges, F. Laeri, F. Schüth and U. Vietze, *Appl. Organomet. Chem.*, 1998, **12**, 305.
- 9 G. Wirnsberger, P. D. Yang, B. J. Scott, B. F. Chmelka and G. D. Stucky, *Spectrochim. Acta, Part A*, 2001, **57**, 2049.
- 10 P. Yang, G. Wirnsberger, H. C. Huang, S. R. Cordero, M. D. Mc Gehee, B. Scott, T. Deng, G. M. Whitesides, B. F. Chmelka, S. K. Buratto and G. D. Stucky, *Science*, 2000, **287**, 465.
- 11 B. J. Scott, G. Wirnsberger and G. D. Stucky, *Chem. Mater.*, 2001, **13**, 3140.
- 12 E. Dovgolevsky, S. Kirmayer, E. Lakin, Y. Yang, C. J. Brinker and G. L. Frey, *J. Mater. Chem.*, 2008, **18**, 423.
- 13 N. Mizoshita, Y. Goto, T. Tani and S. Inagaki, *Adv. Mater.*, 2009, **21**, 4798.
- 14 M. S. Lowry and S. Bernhard, *Chem.-Eur. J.*, 2006, **12**, 7970.
- 15 L. Flamigni, A. Barbieri, C. Sabatini, B. Ventura and F. Barigelletti, *Top. Curr. Chem.*, 2007, **281**, 143.
- 16 M. K. Nazeeruddin and M. Grätzel, *Struct. Bonding*, 2007, **123**, 113.

- 17 Y. You and S. Young Park, *Dalton Trans.*, 2009, 1267.
- 18 C. Ulbricht, B. Beyer, C. Friebe, A. Winter and U. S. Schubert, *Adv. Mater.*, 2009, **21**, 4418.
- 19 Y. Kawamura, J. Brooks, J. J. Brown, H. Sasabe and C. Adachi, *Phys. Rev. Lett.*, 2006, **96**, 017404.
- 20 C. Rothe, C.-J. Chiang, V. Jankus, K. Abdullah, X. Zeng, R. Jitchati, A. S. Batsanov, M. R. Bryce and A. P. Monkman, *Adv. Funct. Mater.*, 2009, **19**, 2038, and references therein.
- 21 C.-H. Chang, C.-C. Chen, C.-C. Wua, C.-H. Yang and Y. Chi, *Org. Electron.*, 2009, **10**, 1364.
- 22 C.-H. Yang, S.-H. Yang and C.-S. Hsu, *Nanotechnology*, 2009, **20**, 315601, and references therein.
- 23 A. B. Tamayo, B. D. Alleyne, P. I. Djurovich, S. Lamansky, I. Tsyba, N. N. Ho, R. Bau and M. E. Thompson, *J. Am. Chem. Soc.*, 2003, **125**, 7377.
- 24 H. S. Zhou and I. Honma, *Adv. Mater.*, 1999, **11**, 683.
- 25 A. B. Tamayo, B. D. Alleyne, P. I. Djurovich, S. Lamansky, I. Tsyba, N. N. Ho, R. Bau and M. E. Thompson, *J. Am. Chem. Soc.*, 2003, **125**, 7377.
- 26 S. Brunauer, P. H. Emmett and E. Teller, *J. Am. Chem. Soc.*, 1938, **60**, 309.
- 27 E. P. Barrett, L. G. Joyner and P. P. Halenda, *J. Am. Chem. Soc.*, 1951, **73**, 373.
- 28 R. I. Nooney, D. Thirunavukkarasu, Y. Chen, R. Josephs and A. E. Ostafin, *Chem. Mater.*, 2002, **14**, 4721.
- 29 D. Zhao, Q. Huo, J. Feng, B. F. Chmelka and G. D. Stucky, *J. Am. Chem. Soc.*, 1998, **120**, 6024.
- 30 H. S. Zhou, H. Sasabe and I. Honma, *J. Mater. Chem.*, 1998, **8**, 515, and references therein.
- 31 Y. Kawamura, J. Brooks, J. J. Brown, H. Sasabe and C. Adachi, *Phys. Rev. Lett.*, 2006, **96**, 017404.
- 32 Y. You and S. Y. Park, *Dalton Trans.*, 2009, 1267.
- 33 W. Holzer, A. Penzkofer and T. Tsuboi, *Chem. Phys.*, 2005, **308**, 93.
- 34 E. B. Nandas, A. Ruseckas, I. D. W. Samuel, S. C. Lo and P. L. Burn, *J. Phys. Chem. B*, 2004, **108**, 1570.
- 35 H. Wang, Q. Liao, H. Fu, Y. Zeng, Z. Jiang, J. Maa and J. Yao, *J. Mater. Chem.*, 2009, **19**, 89.

5.1.2 Communications

Teocoli F., Aiello D. , Aiello I., Talarico A. M. , Ghedini M. Oral Presentation: "**Synthesis and Characterization of new hybrid organic/inorganic materials for electro-optic applications**". V Doctorate Workshop Encounter with Foreign Partners – Ph.D.'S Research Activities, Grand Hotel San Michele – Cetraro (CS) Italia., **27 - 28 Settembre 2010**.

Teocoli F. , Aiello D. , Talarico A. M. , Szerb E. I. , Aiello I. , Testa F. , Ghedini M. Oral Presentation: "**Auto-assembling di complessi luminescenti di iridio(III) in materiali mesoporosi prodotti con diversi templanti**". 10° Convegno Nazionale AIMAT, Capo Vaticano (VV) Italia, **5-8 settembre 2010**. Atti del Convegno: 2010, Centro Editoriale e Librario Università della Calabria:2010, pp. 609-612.

Szerb E. I. , Teocoli F. , Aiello D. , Talarico A. M. , Aiello I. , Ghedini M. , Godbert N. , Yadav Y. J., Poster presentation: "**Metallomesogeni ottaedrici luminescenti utilizzati come surfattanti per la costruzione di materiali mesoporosi funzionali**". 10° Convegno Nazionale AIMAT, Capo Vaticano (VV) Italia, **5-8 settembre 2010**. Atti del convegno 2010, Centro Editoriale e Librario Università della Calabria:2010, pp. 605-608.

Teocoli F., Aiello D., Aiello I. , Talarico A. M., Ghedini M., Poster presentation: "**Luminescent iridium(III) complexes confined in silica mesoporous film**". 17th Interdisciplinary Surface Science Conference, University of Reading, United Kingdom, **30 March-2 April, 2009**.

Teocoli F., Aiello D., Aiello I., Talarico A. M., Ghedini M., Oral Presentation: "**Hybrid mesoporous titania materials**". III Doctorate Workshop Encounter with Ph.D.'S Research Activities., Cetraro (Cs), **25 October 2008**.

Teocoli F., Aiello D., Aiello I., Talarico A. M., Ghedini M., Poster presentation: "**Hibrid mesoporous titania films: an example of pore filling**". IV Convegno Congiunto delle Sezioni Sicilia e Calabria della Società Chimica Italiana, Università della Calabria, Rende (Cosenza), **1-3 Dicembre, 2008**.

Teocoli F., Aiello I., Aiello D., Talarico A. M., Ghedini M., Poster presentation:"**Synthesis and characterization of functionalized mesoporous titania films**".

XIV Scuola Nazionale Scienza dei Materiali, Bressanone (Bolzano), **22-30
Settembre, 2008.**

5.2 Solid state dye-sensitized solar cells: results

The results obtained from the investigations described in Chapter 3 are summarized in the following Paper and Communications.

5.2.1 Paper

FULL PAPER

DOI: 10.1002/chem.200902197

High Molar Extinction Coefficient Organic Sensitizers for Efficient Dye-Sensitized Solar Cells

Hyunbong Choi,^[a] Ines Raabe,^[b] Duckhyun Kim,^[a] Francesca Teocoli,^[b] Chulwoo Kim,^[a] Kihyung Song,^[c] Jun-Ho Yum,^[b] Jaejung Ko,^{*,[a]} Md. K. Nazeeruddin,^{*,[b]} and Michael Grätzel^{*,[b]}

Abstract: We have designed and synthesized highly efficient organic sensitizers with a planar thienothiophene–vinylene–thienothiophene linker. Under standard global AM 1.5 solar conditions, the **JK-113**-sensitized cell gave a short circuit photocurrent density (J_{sc}) of 17.61 mA cm⁻², an open-circuit voltage (V_{oc}) of 0.71 V, and a fill factor (FF) of 72%, corresponding to an overall conversion efficiency (η) of

9.1%. The incident monochromatic photo-to-current conversion efficiency (IPCE) of **JK-113** exceeds 80% over the spectral region from 400 to 640 nm, reaching its maximum of 93% at 475 nm. The band tails off toward

Keywords: dyes/pigments · sensitizers · solar cells · solid-state electrolytes · thienothiophenes

770 nm, contributing to the broad spectral light harvesting. Solar-cell devices based on the sensitizer **JK-113** in conjunction with a volatile electrolyte and a solvent-free ionic liquid electrolyte gave high conversion efficiencies of 9.1% and 7.9%, respectively. The **JK-113**-based solar cell fabricated using a solvent-free ionic liquid electrolyte showed excellent stability under light soaking at 60 °C for 1000 h.

Introduction

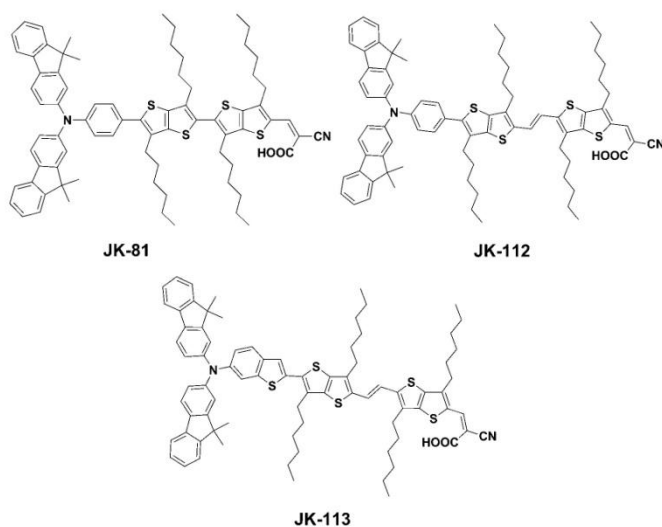
Energy demands and environmental issues such as global warming have led to the search for clean renewable energy sources in recent years.^[1] In this context, dye-sensitized solar cells (DSSCs) are attracting widespread interest due to their low cost and high performance.^[2] Some polypyridyl ruthenium sensitizers achieve power conversion efficiencies in excess of 11%^[3] and show good stability. However, due to the precious metal and its rarity, metal-free organic dyes have attracted considerable attention for practical applications. Recently, the solar-cell performances of DSSCs based

on organic dyes have been remarkably improved and impressive efficiencies in the range 8–9.7% have been achieved.^[4] The main factors responsible for the low efficiencies of organic dyes compared to the ruthenium sensitizers are narrow absorption bands in the visible region and the formation of dye aggregates on the semiconductor surface.^[5] Therefore, many attempts have been made to design and construct organic dye molecules with higher molar extinction coefficients and broader spectral responses. Most of the efficient organic dyes contain a donor and acceptor bridged by a π -conjugated linker (D- π -A). To enhance the molar extinction coefficient as well as to realize panchromatic light-harvesting, tuning of the length and torsion angle of the conjugated linker is important. Recently, a successful approach was introduced in which a π -conjugated linker such as a thiophene^[6] or thienothiophene^[7] derivative was incorporated into an organic framework, thereby enhancing the efficiency and stability. Herein, we report highly efficient organic sensitizers, coded as **JK-112** and **JK-113** (Scheme 1), which consist of a dimethylfluorenylamino-appended thienothiophene–vinylene–thienothiophene unit with aliphatic chains that maintain the planar geometry of the conjugated linker. This not only increases the extinction coefficient of the sensitizer by extending the π -conjugation of the bridging linker, but also augments its hydrophobicity, increasing the stability under long-term light soaking and thermal stress.

[a] Dr. H. Choi, Dr. D. Kim, C. Kim, Prof. Dr. J. Ko
Department of New Material Chemistry, Korea University
Jochiwon, Chungnam 339-700 (Korea)
Fax: (+82)41-867-5396
E-mail: jko@korea.ac.kr

[b] Dr. I. Raabe, F. Teocoli, Dr. J.-H. Yum, Dr. Md. K. Nazeeruddin,
Prof. Dr. M. Grätzel
LPI, Institut des Sciences et Ingénierie Chimiques
Faculté des Sciences de Base
École Polytechnique Fédérale de Lausanne
1015 Lausanne (Switzerland)

[c] Prof. Dr. K. Song
Department of Chemistry, Korea National University of Education
Cheongwon, Chungbuk 363-791 (Korea)



Scheme 1. The structures of **JK-81**, **JK-112**, and **JK-113**.

Results and Discussion

The organic sensitizers have been efficiently synthesized by the stepwise synthetic protocol illustrated in Scheme 2. Compound **2** was prepared from **1** by a McMurry reaction and was then converted into **3** by lithiation with *n*-butyllithium and subsequent quenching with pinacol borate. Suzuki coupling reactions of *N,N*-bis(9,9-dimethylfluoren-2-yl)-4-bromoaniline^[11] and 6-[bis(9,9-dimethylfluoren-2-yl)amino]-2-bromobenzo[*b*]thiophene^[12] with 1.2 equivalents of **3** yielded **4** and **5**, respectively. Suzuki coupling reaction of *N,N*-bis(9,9-dimethylfluoren-2-yl)-4-bromoaniline with 2-(3,6-dihexylthieno[3,2-*b*]thiophen-2-yl)-4,4,5,5-tetramethyl-1,3,2-dioxaborolane led to **8**. Bromination of **8** with Br₂ gave **9**. Compound **10** was prepared from **9** with 2-(3,6-dihexylthieno[3,2-*b*]thiophen-2-yl)-4,4,5,5-tetramethyl-1,3,2-dioxaborolane by a Suzuki reaction. The thienothiophene-vinylene-thienothiophene derivatives **4** and **5** and the dithienothiophene derivative **10** were converted into their corresponding carbaldehydes **6**, **7**, and **11** by Vilsmeier-Haack reactions. Reactions of the aldehyde derivatives with cyanoacetic acid in the presence of piperidine in acetonitrile produced the dyes **JK-81**, **JK-112**, and **JK-113**, respectively.

The visible absorption spectrum of **JK-112** displays two absorption maxima at 480 nm ($\epsilon = 73\,800\text{ M}^{-1}\text{ cm}^{-1}$) and 365 nm ($\epsilon = 51\,800\text{ M}^{-1}\text{ cm}^{-1}$), which are due to the π - π^* transitions of the conjugated system. Under the same conditions, the dye **JK-113** exhibits absorption bands at 490 nm ($\epsilon = 85\,000\text{ M}^{-1}\text{ cm}^{-1}$) and 365 nm ($\epsilon = 50\,400\text{ M}^{-1}\text{ cm}^{-1}$), as shown in Figure 1. Such high coefficients can be expected to permit a reduction in film thickness in solar-cell applications, which should increase the open-circuit voltage and overall efficiency. The slight blueshift in the absorptions of **JK-112** com-

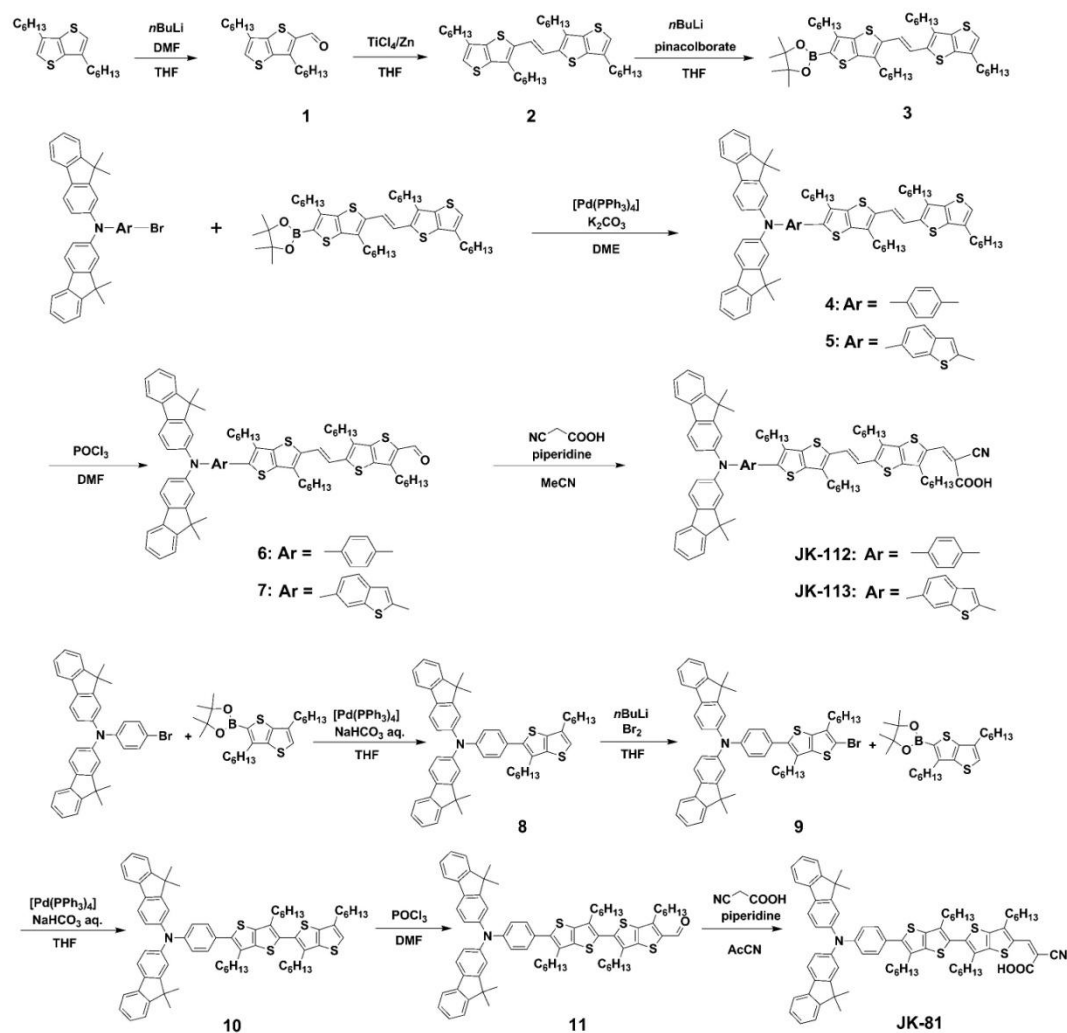
pared to those of **JK-113** can be readily understood from molecular modeling studies (Figure 2). The ground-state structures of **JK-112** and **JK-113** have twist angles of 51.0° and 46.6°, respectively, between the aminophenyl or -benzo[*b*]thiophenyl moieties and the thienothiophene units, indicating that the latter has a more planar geometry due to a smaller torsion angle. On the other hand, the dye **JK-81** exhibits a further blue shift to 372 nm due to the wide dihedral angle (64.7°) of the two thienothiophene units, which gives rise to a twisted nonplanar geometry. For **JK-112** and **JK-113**, the dihedral angles of the thienothiophene-vinylene-thienothiophene bridged units are 1.8° and 0.8°, respectively. Accordingly, the higher extinction co-

efficients of **JK-112** and **JK-113** relative to that of **JK-81** and the associated redshifts derive from increased electron delocalization over the conjugated system. Similar distortions have been reported for other organic dyes.^[7b,8]

When **JK-112** and **JK-113** are excited within their π - π^* bands, they exhibit strong luminescence maxima at 632 nm, with $E_{0,0}$ transition energies of 2.28 and 2.24 eV, respectively (Table 1). The excited-state oxidation potentials (E_{ox}^*) of the dyes (**JK-112**: -1.15 V; **JK-113**: -1.18 V vs. NHE) are much more negative than the conduction band of TiO₂, located at -0.5 V versus NHE, allowing efficient electron injection from the LUMO of the dye to the conduction band of TiO₂.

Molecular-orbital calculations have indicated that the HOMOs of **JK-112** and **JK-113** are spread over the fluorenylamino unit through the phenyl or benzo[*b*]thiophene groups and that the LUMOs are located on the cyanoacrylic units and extend to the thienothiophene moieties (Figure 3). Examination of the HOMOs and LUMOs of these dyes indicates that HOMO-LUMO excitation moves the electron from the phenyl- or benzo[*b*]thiophene unit to the cyanoacrylic acid moiety. The change in local electron density distribution induced by photoexcitation results in efficient charge separation.

The incident monochromatic photo-to-current conversion efficiency (IPCE) of **JK-113** exceeds 80% over the spectral region from 400 to 640 nm, reaching its maximum of 93% at 475 nm (Figure 4, top). The band tails off toward 770 nm, contributing to the broad spectral light harvesting. Under standard global AM 1.5 solar conditions, the **JK-113**-sensitized cell gave a short circuit photocurrent density (J_{sc}) of 17.61 mA cm⁻², an open-circuit voltage (V_{oc}) of 0.71 V, and a

Scheme 2. Synthetic routes to **JK-112**, **JK-113**, and **JK-81**.

fill factor (*FF*) of 72%, corresponding to an overall conversion efficiency (η) of 9.1%. Integrating the IPCE curve for **JK-113** over the standard AM 1.5 global solar spectrum results in a short circuit current of 17.4 mA cm^{-2} , in good agreement with the measured photocurrent of the device. To the best of our knowledge, this is the highest efficiency ever reported for a DSSC based on an organic sensitizer without using 3 α ,7 α -dihydroxy-5 β -cholic acid as a co-adsorbent. Using a TiO_2 electrode stained with 0.15 mm **JK-113** in the presence of 1 mM tetrabutylammonium deoxycholic acid salt (DCA-TBA) in THF, the cell displayed a J_{sc} of 14.9 mA cm^{-2} , a V_{oc} of 810 mV, and an *FF* of 79%, corresponding to an η of 9.5% when the spectra were measured

two days after cell fabrication (Figure 5). Reproducible efficiencies of 9.2–9.5% were obtained with the solar cell based on **JK-113**. Using a solvent-free ionic-liquid electrolyte composed of 0.2 M I_2 , 0.5 M N-methyl benzimidazole (NMBI), and 0.1 M guanidinium thiocyanate (GuNCS) in 1-methyl-3-propylimidazolium iodide (PMII)/1-methyl-3-ethylimidazolium thiocyanate (EMINCS) (13:7), the **JK-113** sensitizer displayed a strikingly high conversion efficiency of 7.9%, which is comparable to the highest values hitherto achieved for solvent-free DSSCs based on ruthenium sensitizers.^[3c,d,9] Devices based on **JK-113** using ionic liquid electrolytes showed excellent long-term stability under accelerated light soaking at 60°C. Figure 6 shows stability data for **JK-112**

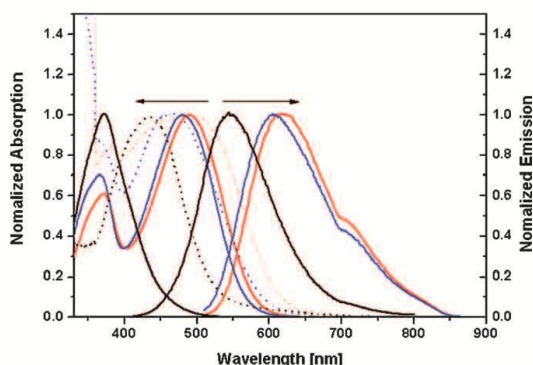


Figure 1. Absorption (left scale) and emission (right scale) spectra of **JK-81** (black solid line), **JK-112** (blue solid line), and **JK-113** (red solid line) in THF. The absorption spectra as anchored sensitizers on TiO₂ film of **JK-81** (black dotted line), **JK-112** (blue dotted line), and **JK-113** (red dotted line) are also included. The emission spectra were obtained using the same solutions by exciting at 370, 480, and 490 nm for **JK-81**, **JK-112**, and **JK-113**, respectively, at 298 K.

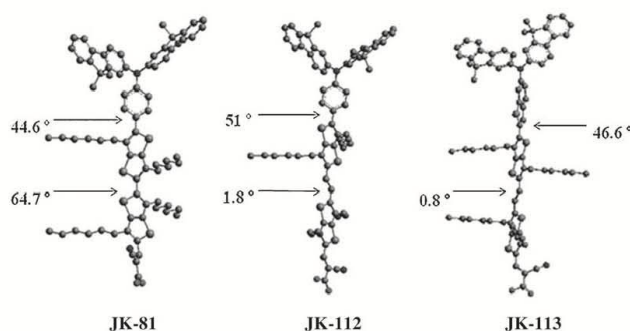


Figure 2. Optimized structures calculated by TD-DFT using the B3LYP functional and the 3-21G* basis set for **JK-81**, **JK-112**, and **JK-113**.

Table 1. Optical, redox, and DSSC performance parameters of **JK-81**, **JK-112**, and **JK-113**.

	JK-81	JK-112	JK-113
$\lambda_{\text{abs}}^{[a]}$ [nm]	372 (55 800)	365 (51 800),	365 (50 400),
ϵ [$\text{M}^{-1}\text{cm}^{-1}$]		480 (73 800)	490 (85 000)
$E_{\text{redox}}^{[b]}$ [V]	1.06	1.13	1.06
$E_{00}^{[c]}$ [V]	2.71	2.28	2.24
$E_{\text{ox}}^{* [d]}$ [V]	-1.65	-1.15	-1.18
$J_{\text{sc}}^{[e]}$ [mA cm^{-2}]	9.4	15.7	17.6
V_{oc} [mV]	710	690	710
FF [%]	75	74	72
η [%]	5.1	8.0	9.1

[a] Absorption spectra were measured in THF solution. [b] Redox potentials of the dyes on TiO₂ were measured in CH₃CN with 0.1 M [(*n*-C₄H₉)₄N][PF₆] as supporting electrolyte at a scan rate of 50 mV s⁻¹ (vs. NHE). [c] E_{00} was determined from the intersection of the absorption and emission spectra in ethanol. [d] E_{ox}^{*} was calculated as $E_{\text{redox}}^{*} - E_{00}$. [e] Performances of the DSSCs were measured with 0.18 cm² working area. Electrolyte 1: 0.6 M DMPImI, 0.05 M I₂, 0.1 M LiI, and 0.5 M *tert*-butylpyridine in acetonitrile.

and **JK-113** during long-term accelerated aging. After 1000 h of light soaking, the V_{oc} of **JK-113** had decreased by 54 mV, but the loss was compensated by a slight increase in the short-circuit current density from 16.5 to 16.7 mA cm⁻² and in the fill factor from 68% to 69%. The initial efficiency of 7.9% slightly decreased to 7.4% during the 1000 h light-soaking test.

An all-solid-state dye-sensitized solar cell (ssDSSC) was constructed, employing **JK-112** as a sensitizer and 2,2',7,7'-tetrakis(*N,N*-dimethoxyphenylamine)-9,9'-spiro-bifluorene (Spiro-OMeTAD) as a hole conductor. This device gave a J_{sc} of 8.0 mA cm⁻², a V_{oc} of 900 mV, and an FF of 60%, corresponding to an overall conversion efficiency η of 4.3% under standard global AM 1.5 solar conditions (Table 2). At lower light intensity, the power conversion efficiency increased to 4.8%, which is a remarkable value for an ssDSSC based on an organic sensitizer. Of particular note are the high V_{oc} values of the cells (both with **JK-112** (900 mV) and **JK-113** (920 mV)). This stems from the thinner TiO₂ film, which retards the charge recombination dynamics due to the higher absorption coefficient arising from extended conjugation.

AC impedance spectra of the cells were measured to check for any changes in the electric circuit elements of the DSSC during aging. Figure 7 shows the AC impedance spectra of the DSSCs measured in the dark and under illumination (bottom). In the dark under forward bias (-0.68 V), the semicircle in the intermediate frequency regime reflects mainly the recombination impedance caused by electron loss from the conduction band of TiO₂ to I₃⁻ ions in the electrolyte.^[10] A larger radius of the semicircle in this intermediate frequency regime implies a lower rate of electron recombination at the TiO₂/dye/electrolyte interface. In the dark at 0.68 V forward bias, the radius of this semicircle increases in the order **JK-112** (50.0 Ω) < **JK-113** (60.7 Ω) < **JK-81** (68.51 Ω), in accord with the trends in the values of V_{oc} . Upon illumination under open-circuit conditions (100 mW cm⁻²), the radius of the intermediate-frequency semicircle in the Nyquist plot decreased in the order **JK-81** (24.1 Ω) > **JK-112** (12.0 Ω) > **JK-113** (11.7 Ω), indicating improved electron generation and transport. These results are in good agreement with the trends observed in the overall efficiency.

Conclusions

In summary, we have designed and synthesized three highly efficient organic sensitizers with a planar thienothiophene-

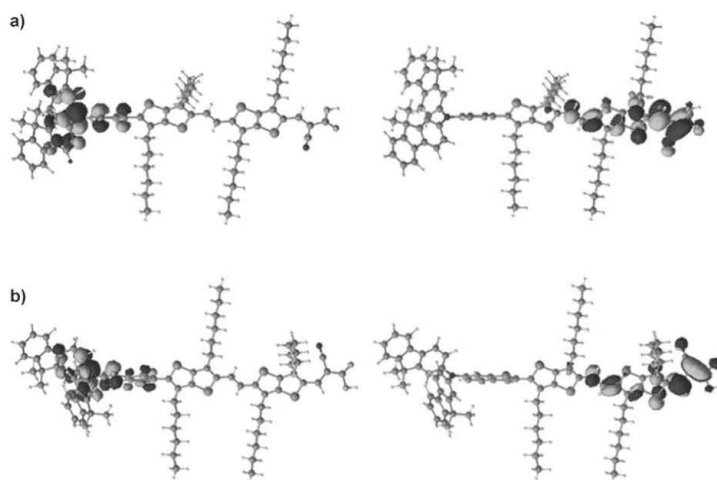


Figure 3. Isodensity surface plots of the HOMO and LUMO of (a) **JK-112** and (b) **JK-113**.

vinylene–thienothiophene linker. Solar-cell devices based on the sensitizer **JK-113** in conjunction with a volatile electrolyte without the tetrabutylammonium salt of deoxycholic acid DCA·TBA, with DCA·TBA, and a solvent-free ionic liquid electrolyte gave high conversion efficiencies of 9.1%, 9.5%, and 7.9%, respectively. A **JK-113**-based solar cell fabricated using a solvent-free ionic liquid electrolyte showed excellent stability under light soaking at 60°C for 1000 h. We believe that the development of highly efficient organic dyes comparable to ruthenium dyes is possible through meticulous molecular engineering of organic dyes, and work directed towards this aim is now in progress.

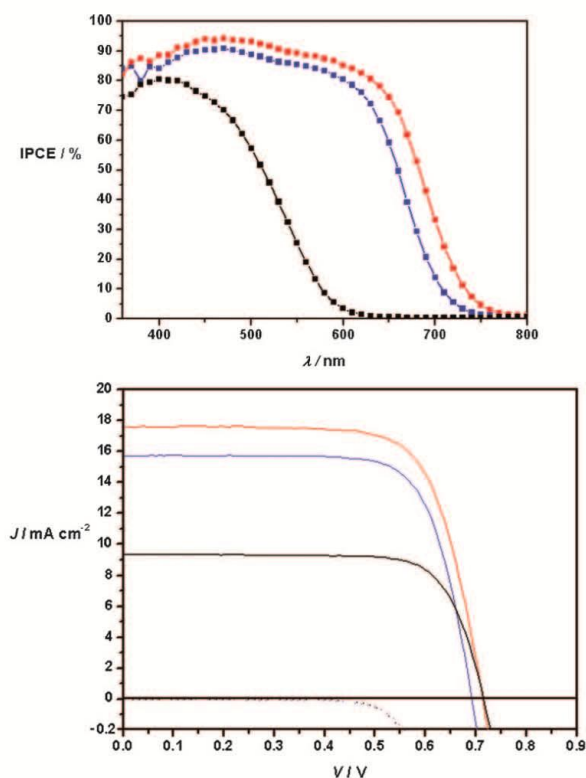


Figure 4. IPCE spectra (top) and J - V curves (bottom) of **JK-81** (black lines), **JK-112** (blue lines), and **JK-113** (red lines). Dark current–bias potential relationships are shown as dotted curves.

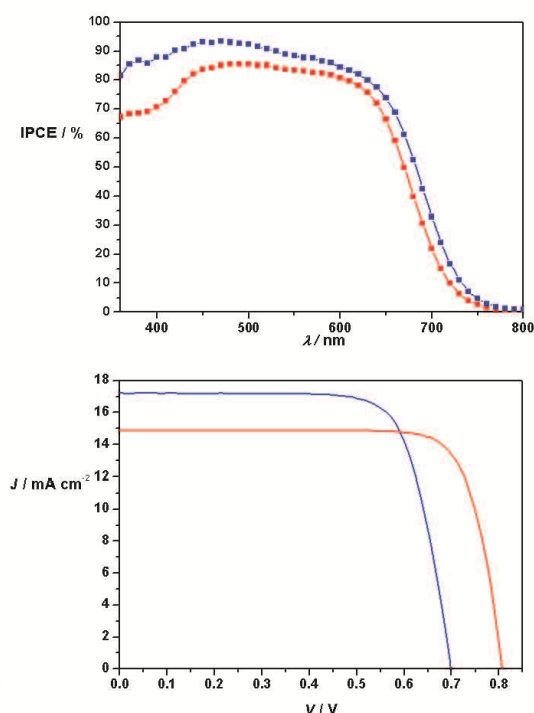


Figure 5. IPCE spectra (top) and J - V curves (bottom) of **JK-113**+DCA·TBA (blue lines) and **JK-113**+DCA·TBA after two days (red lines).

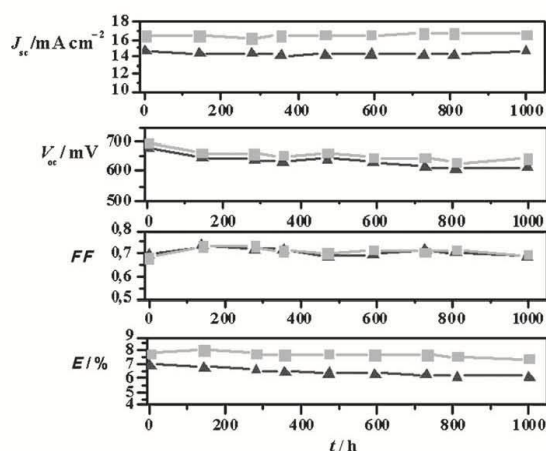


Figure 6. Evolution of solar-cell parameters with JK-112 (▲) and JK-113 (■) during visible-light soaking (AM 1.5 G, 100 mWcm⁻²) at 60°C. A 420 nm cut-off filter was placed on the cell surface during illumination. Ionic liquid electrolyte 2: 0.2M iodine, 0.5M NMBI, 0.1M GuNCS in PMII/EMINCS (13:7).

Table 2. *J-V* characteristics of JK-112- and JK-113-sensitized solar cells with solid-state electrolytes under different light intensities.

Dye	Intensity [% sun]	J_{sc} [mA cm ⁻²]	V_{oc} [mV]	FF [%]	η [%]
JK-112	10	0.8	780	73	4.8
	100	8.0	900	60	4.3
JK-113	10	0.7	810	70	4.2
	100	8.3	920	57	4.3

Experimental Section

General: All reactions were carried out under an argon atmosphere. Solvents were distilled from appropriate reagents. All reagents were purchased from Sigma-Aldrich. *N,N*-Bis(9,9-dimethylfluoren-2-yl)-4-bromoaniline,^[11] 6-[bis(9,9-dimethylfluoren-2-yl)amino]-2-bromobenzo[*b*]thiophene,^[12] and 3,6-dihexylthieno[3,2-*b*]thiophene^[13] were synthesized using modified procedures based on those in the previous references. ¹H and ¹³C NMR spectra were recorded on a Varian Mercury 300 spectrometer. Elemental analyses were performed with a Carlo Erba Instruments CHNS-O EA 1108 analyzer. Mass spectra were recorded on a JEOL JMS-SX102A instrument. Absorption and photoluminescence spectra were recorded on a Perkin-Elmer Lambda 2S UV/visible spectrophotometer and a Perkin LS fluorescence spectrometer, respectively.

3,6-Dihexylthieno[3,2-*b*]thiophene-2-carbaldehyde (1): *n*BuLi (2.85 mL, 2.5 M solution in hexane) was added to a solution of 3,6-dihexylthieno[3,2-*b*]thiophene (2 g, 6.48 mmol) in dry THF (50 mL) at 0°C under argon. After 1 h, DMF (1 g, 6.48 mmol) was added dropwise at 0°C under argon. The solution was washed with 5% HCl and dried with MgSO₄. The solvent was evaporated. The pure product **1** was obtained in 90% yield by silica gel chromatography (eluent CH₂Cl₂/hexane, 1:1, *R*_f = 0.5). M.p. 140°C; ¹H NMR (CDCl₃): δ = 10.09 (s, 1H), 7.26 (s, 1H), 3.09 (t, *J* = 7.8 Hz, 2H), 2.72 (t, *J* = 7.2 Hz, 2H), 1.72 (br, 4H), 1.36 (m, 12H), 0.89 (t, *J* = 6.8 Hz, 3H), 0.86 ppm (t, *J* = 6.8 Hz, 3H); ¹³C{¹H} NMR (CDCl₃): δ = 182.1, 142.1, 141.5, 137.5, 135.6, 131.1, 121.3, 31.7, 31.6, 30.5, 30.0, 29.4, 29.2, 28.9, 28.5, 28.0, 22.7, 14.3, 14.2 ppm; MS: *m/z*: 336 [*M*⁺]; elemental analysis calcd (%) for C₁₉H₂₈O₂: C 67.81, H 8.39; found: C 67.21, H 8.19.

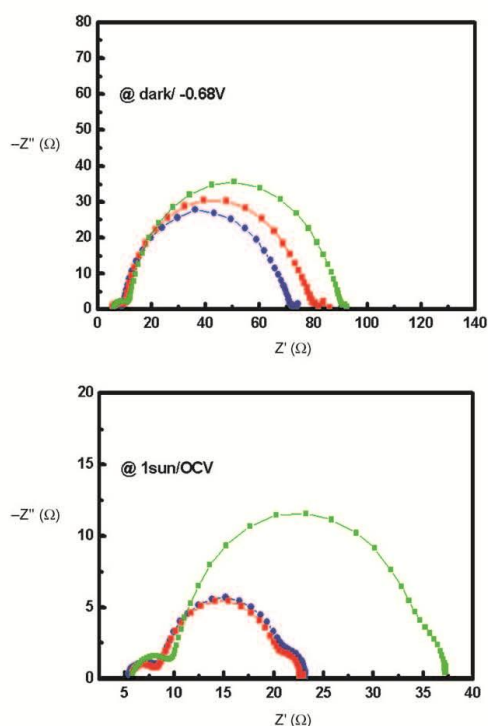


Figure 7. Electrochemical impedance spectra measured in the dark and under illumination (1 sun, bottom) for cells with different adsorbed dyes (i.e. JK-112 (blue line), JK-113 (red line), and JK-81 (green line)).

(*E*)-1,2-Bis(3,6-dihexylthieno[3,2-*b*]thiophen-2-yl)ethene (2): TiCl₄ (1.95 mL, 17.82 mmol) was added to a suspension of Zn powder (1.165 g, 17.82 mmol) in dry THF (50 mL) at 0°C under argon. After 1 h, a solution of compound **1** (2 g, 5.94 mmol) in THF (10 mL) was added dropwise at 0°C under argon. The mixture was stirred at 70°C for 10 h, then cooled to room temperature, quenched with H₂O (30 mL), and extracted with EtOAc (3 × 30 mL). The organic layer was separated and dried over MgSO₄. The solvent was removed in vacuo. The pure product **2** was obtained by chromatographic work-up (eluent CH₂Cl₂/hexane, 1:3, *R*_f = 0.4) as a yellow solid in 60% yield. M.p. 182°C; ¹H NMR (CDCl₃): δ = 7.06 (s, 1H), 6.95 (s, 1H), 2.80 (t, *J* = 7.2 Hz, 4H), 2.70 (t, *J* = 7.2 Hz, 4H), 1.72 (br, 8H), 1.34 (m, 24H), 0.89 ppm (m, 12H); ¹³C{¹H} NMR (CDCl₃): δ = 137.7, 135.6, 134.5, 133.6, 121.5, 119.8, 31.7, 31.6, 30.5, 30.0, 29.9, 29.4, 28.8, 28.5, 28.1, 22.7, 14.3, 14.2 ppm; MS: *m/z*: 640 [*M*⁺]; elemental analysis calcd (%) for C₃₈H₅₆S₂: C 71.19, H 8.80; found: C 70.98, H 8.69.

(*E*)-2-[5-[2-(3,6-Dihexylthieno[3,2-*b*]thiophen-2-yl)vinyl]-3,6-dihexylthieno[3,2-*b*]thiophen-2-yl]-4,4,5,5-tetramethyl-1,3,2-dioxaborolane (3): *n*BuLi (0.24 mL, 2.5 M solution in hexane) was added to a solution of compound **2** (0.35 g, 0.55 mmol) in dry THF (30 mL) at -78°C under argon. After 1 h, 2-isopropoxy-4,4,5,5-tetramethyl-1,3,2-dioxaborolane (0.121 g, 0.655 mmol) was added dropwise at -78°C under argon. The mixture was stirred at 20°C for 1 h, then quenched with H₂O (30 mL) and extracted with EtOAc (3 × 30 mL). The organic layer was separated and dried over MgSO₄. The solvent was removed in vacuo. The pure product **3** was obtained by chromatographic work-up (eluent CH₂Cl₂/hexane, 1:1, *R*_f = 0.4) as a yellow solid in 60% yield. M.p. 162°C; ¹H NMR (CDCl₃): δ = 9.82 (s, 1H), 7.65 (t, *J* = 6.3 Hz, 2H), 7.09 (s, 1H), 7.08 (s, 1H), 6.95 (s, 1H), 2.97 (t, *J* = 7.8 Hz, 2H), 2.81 (m, 4H), 2.70 (t,

$J=7.8$ Hz, 2H), 1.73 (m, 8H), 1.35 (m, 24H), 0.89 ppm (m, 12H); $^{13}\text{C}\{^1\text{H}\}$ NMR (CDCl_3): $\delta=146.2$, 146.0, 140.9, 140.2, 138.4, 138.2, 137.7, 136.4, 135.6, 133.6, 133.2, 125.9, 122.0, 121.3, 83.9, 31.7, 31.6, 30.5, 30.0, 29.9, 29.4, 28.8, 28.5, 28.1, 22.9, 22.7, 14.2, 14.1 ppm; MS: m/z : 766 [M^+]; elemental analysis calcd (%) for $\text{C}_{44}\text{H}_{67}\text{BO}_5\text{S}_4$: C 68.89, H 8.80; found: C 68.12, H 8.32.

(E)-N-(4-[5-[2-(3,6-Dihexylthieno[3,2-b]thiophen-2-yl)vinyl]-3,6-dihexylthieno[3,2-b]thiophen-2-yl]phenyl)-N-(9,9-dimethyl-9H-fluoren-2-yl)-9,9-dimethyl-9H-fluoren-2-amine (4): A stirred mixture of *N,N*-bis(9,9-dimethylfluoren-2-yl)-4-bromoaniline (0.138 g, 0.25 mmol), **3** (0.191 g, 0.25 mmol), K_2CO_3 (0.20 g, 1.5 mmol), and $\text{Pd}(\text{PPh}_3)_4$ (0.029 g, 0.025 mmol) in THF (50 mL) and H_2O (5 mL) was refluxed for 12 h. After cooling the solution, H_2O (10 mL) and brine (10 mL) were added. The organic layer was separated and dried over MgSO_4 . The solvent was removed in vacuo. The pure product **4** was obtained by chromatographic work-up (eluent $\text{CH}_2\text{Cl}_2/\text{hexane}$, 1:3, $R_f=0.4$) as a green solid in 70% yield. M.p. 178 °C; ^1H NMR (CDCl_3): $\delta=7.65$ (t, $J=7.8$ Hz, 2H), 7.63 (d, $J=8.2$ Hz, 2H), 7.40 (d, $J=8.2$ Hz, 2H), 7.35 (t, $J=7.8$ Hz, 2H), 7.33–7.25 (m, 6H), 7.24 (s, 2H), 7.16 (d, $J=7.6$ Hz, 2H), 7.13 (s, 1H), 7.10 (s, 1H), 7.00 (s, 1H), 2.82 (t, $J=7.8$ Hz, 2H), 2.81–2.71 (m, 6H), 1.85–1.71 (m, 8H), 1.43 (s, 12H), 1.34–1.24 (m, 24H), 0.89 (t, $J=6.8$ Hz, 3H), 0.88–0.86 (m, 6H), 0.85 ppm (t, $J=6.8$ Hz, 3H); $^{13}\text{C}\{^1\text{H}\}$ NMR (CDCl_3): $\delta=155.2$, 153.6, 147.6, 147.2, 140.4, 139.3, 139.0, 136.8, 135.5, 135.3, 134.6, 132.3, 132.1, 132.0, 131.3, 130.8, 130.1, 129.7, 128.8, 128.7, 128.5, 127.1, 126.7, 125.6, 123.6, 123.3, 122.6, 120.8, 119.6, 119.0, 47.0, 31.8, 31.7, 31.6, 31.5, 30.5, 30.4, 30.0, 29.8, 29.6, 29.4, 29.3, 29.2, 29.0, 28.9, 28.7, 28.5, 28.3, 28.0, 27.8, 27.6, 27.1, 22.7, 14.3, 14.2, 14.1 ppm; MS: m/z : 1115 [M^+]; elemental analysis calcd (%) for $\text{C}_{78}\text{H}_{108}\text{NS}_4$: C 79.59, H 7.67; found: C 79.18, H 7.43.

(E)-2-[5-[2-(3,6-Dihexylthieno[3,2-b]thiophen-2-yl)vinyl]-3,6-dihexylthieno[3,2-b]thiophen-2-yl]-N,N-bis(9,9-dimethyl-9H-fluoren-2-yl)benzo[b]thiophen-6-amine (5): Compound **5** was synthesized by a similar procedure to that described for **4**, except that 6-[bis(9,9-dimethylfluoren-2-yl)amino]-2-bromoaniline was used in place of *N,N*-bis(9,9-dimethylfluoren-2-yl)-4-bromoaniline. Yield: 51%. M.p. 187 °C; ^1H NMR (CDCl_3): $\delta=7.64$ (d, $J=9.0$ Hz, 1H), 7.59 (d, $J=8.1$ Hz, 2H), 7.58 (t, $J=8.1$ Hz, 2H), 7.56 (s, 1H), 7.39 (t, $J=8.1$ Hz, 2H), 7.36 (d, $J=9.0$ Hz, 1H), 7.32–7.28 (m, 4H), 7.25 (s, 2H), 7.19 (s, 1H), 7.13 (s, 1H), 7.11 (s, 1H), 7.10 (d, $J=8.1$ Hz, 2H), 2.82 (t, $J=7.8$ Hz, 2H), 2.81–2.71 (m, 6H), 1.85–1.71 (m, 8H), 1.43 (s, 12H), 1.34–1.24 (m, 24H), 0.89 (t, $J=6.8$ Hz, 3H), 0.88–0.86 (m, 6H), 0.85 ppm (t, $J=6.8$ Hz, 3H); $^{13}\text{C}\{^1\text{H}\}$ NMR (CDCl_3): $\delta=155.3$, 153.7, 147.5, 146.5, 145.4, 143.7, 142.2, 141.1, 139.0, 138.4, 137.5, 136.5, 135.2, 134.8, 134.4, 134.1, 133.9, 133.8, 132.8, 132.3, 131.2, 130.9, 129.8, 128.7, 127.1, 126.7, 126.5, 126.3, 123.2, 122.7, 120.8, 119.5, 118.6, 116.7, 47.0, 31.8, 31.7, 31.6, 31.5, 30.5, 30.4, 30.0, 29.8, 29.6, 29.4, 29.3, 29.2, 29.0, 28.9, 28.7, 28.5, 28.3, 28.0, 27.8, 27.6, 27.1, 22.7, 14.3, 14.2, 14.1 ppm; MS: m/z : 1117 [M^+]; elemental analysis calcd (%) for $\text{C}_{76}\text{H}_{106}\text{NS}_5$: C 77.83, H 7.31; found: C 77.38, H 7.23.

(E)-5-[2-(5-[4-[Bis(9,9-dimethyl-9H-fluoren-2-yl)amino]phenyl)-3,6-dihexylthieno[3,2-b]thiophen-2-yl)vinyl]-3,6-dihexylthieno[3,2-b]thiophene-2-carbaldehyde (6): The Vilsmeier reagent, which was prepared from POCl_3 (0.06 mL) in DMF (0.1 mL), was added to a cold solution of **4** (0.37 g, 0.33 mmol) in dry DMF (10 mL) at 0 °C. The mixture was stirred at 70 °C for 4 h, then cooled to room temperature, quenched with 10% aqueous NaOAc solution (30 mL), and extracted with EtOAc (3 × 30 mL). The organic layer was separated and dried over MgSO_4 . The solvent was removed in vacuo. The pure product **6** was obtained by chromatographic work-up (eluent $\text{CH}_2\text{Cl}_2/\text{hexane}$, 1:1, $R_f=0.4$) as an orange solid in 85% yield. M.p. 176 °C; ^1H NMR (CDCl_3): $\delta=10.05$ (s, 1H), 7.65 (t, $J=7.2$ Hz, 2H), 7.62 (d, $J=8.2$ Hz, 2H), 7.36 (d, $J=8.2$ Hz, 2H), 7.35 (t, $J=7.2$ Hz, 2H), 7.33–7.25 (m, 5H), 7.24 (s, 2H), 7.19 (d, $J=15.6$ Hz, 1H), 7.13 (d, $J=8.1$ Hz, 2H), 7.06 (d, $J=15.6$ Hz, 1H), 6.98 (s, 1H), 3.08 (t, $J=7.8$ Hz, 2H), 2.82–2.81 (m, 4H), 2.71 (t, $J=7.8$ Hz, 2H), 1.85–1.71 (m, 8H), 1.43 (s, 12H), 1.34–1.24 (m, 24H), 0.89 (t, $J=6.8$ Hz, 3H), 0.88–0.86 (m, 6H), 0.85 ppm (t, $J=6.8$ Hz, 3H); $^{13}\text{C}\{^1\text{H}\}$ NMR (CDCl_3): $\delta=181.2$, 155.4, 153.2, 147.3, 147.1, 140.4, 139.3, 139.0, 136.8, 135.7, 135.3, 134.6, 133.4, 132.3, 132.1, 132.0, 130.8, 130.3, 130.1, 129.7, 128.8, 128.7,

128.5, 128.1, 127.7, 126.6, 124.6, 123.4, 122.6, 120.8, 120.6, 47.0, 31.8, 31.7, 31.6, 31.5, 30.5, 30.4, 30.0, 29.8, 29.6, 29.4, 29.3, 29.2, 29.0, 28.9, 28.7, 28.5, 28.3, 28.0, 27.8, 27.6, 27.1, 22.7, 14.3, 14.2, 14.1 ppm; MS: m/z : 1143 [M^+]; elemental analysis calcd (%) for $\text{C}_{76}\text{H}_{106}\text{NOS}_4$: C 78.69, H 7.48; found: C 78.28, H 7.13.

(E)-5-[2-(5-[6-[Bis(9,9-dimethyl-9H-fluoren-2-yl)amino]benzo[b]thiophen-2-yl]-3,6-dihexylthieno[3,2-b]thiophen-2-yl)vinyl]-3,6-dihexylthieno[3,2-b]thiophene-2-carbaldehyde (7): Compound **7** was synthesized by a procedure similar to that described for **6**, except that **4** (0.3 g, 0.249 mmol) was used in place of **5**. Yield: 51%. M.p. 186 °C; ^1H NMR (CDCl_3): $\delta=10.05$ (s, 1H), 7.64 (d, $J=9.0$ Hz, 1H), 7.59 (d, $J=8.1$ Hz, 2H), 7.58 (t, $J=8.1$ Hz, 2H), 7.61 (s, 1H), 7.39 (t, $J=8.1$ Hz, 2H), 7.36 (d, $J=9.0$ Hz, 1H), 7.32–7.28 (m, 4H), 7.25 (s, 2H), 7.19 (d, $J=15.6$ Hz, 1H), 7.10 (d, $J=8.1$ Hz, 2H), 7.06 (d, $J=15.6$ Hz, 1H), 6.98 (s, 1H), 3.07 (t, $J=7.8$ Hz, 2H), 2.96 (t, $J=7.8$ Hz, 2H), 2.82 (t, $J=7.8$ Hz, 4H), 1.85–1.71 (m, 8H), 1.43 (s, 12H), 1.34–1.24 (m, 24H), 0.89 (t, $J=6.8$ Hz, 3H), 0.88–0.86 (m, 6H), 0.85 ppm (t, $J=6.8$ Hz, 3H); $^{13}\text{C}\{^1\text{H}\}$ NMR (CDCl_3): $\delta=180.8$, 155.6, 154.7, 148.5, 147.5, 145.3, 143.7, 142.2, 141.1, 139.0, 138.4, 137.5, 136.5, 136.2, 134.8, 134.4, 134.1, 133.9, 133.8, 132.8, 132.3, 131.8, 131.2, 130.8, 129.5, 128.5, 127.1, 126.7, 126.5, 126.3, 123.2, 122.7, 120.8, 119.5, 47.0, 31.8, 31.7, 31.6, 31.5, 30.5, 30.4, 30.0, 29.8, 29.6, 29.4, 29.3, 29.2, 29.0, 28.9, 28.7, 28.5, 28.3, 28.0, 27.8, 27.6, 27.1, 22.7, 14.3, 14.2, 14.1 ppm; MS: m/z : 1199 [M^+]; elemental analysis calcd (%) for $\text{C}_{77}\text{H}_{108}\text{NS}_5$: C 77.02, H 7.13; found: C 76.98, H 7.03.

N-[4-(3,6-Dihexylthieno[3,2-b]thiophen-2-yl)phenyl]-N-(9,9-dimethyl-9H-fluoren-2-yl)-9,9-dimethyl-9H-fluoren-2-amine (8): *n*BuLi (1.78 mL, 1.6 M solution in hexane) was added to a solution of 3,6-dihexylthieno[3,2-b]thiophene (0.8 g, 2.59 mmol) in dry THF at -78°C under argon. After 1 h, 2-isopropoxy-4,4,5,5-tetramethyl-1,3,2-dioxaborolane (0.578 g, 3.108 mmol) was added dropwise at -78°C under argon. The mixture was stirred at 20 °C for 1 h, then quenched with H_2O (30 mL) and extracted with EtOAc (3 × 30 mL). The organic layers were combined and dried over MgSO_4 . The solvent was removed in vacuo. The pure product **2-(3,6-dihexylthieno[3,2-b]thiophen-2-yl)-4,4,5,5-tetramethyl-1,3,2-dioxaborolane** was obtained by chromatographic work-up (eluent $\text{CH}_2\text{Cl}_2/\text{hexane}$, 1:3, $R_f=0.4$). A stirred mixture of *N,N*-bis(9,9-dimethylfluoren-2-yl)-4-bromoaniline (0.5 g, 0.89 mmol), 2-(3,6-dihexylthieno[3,2-b]thiophen-2-yl)-4,4,5,5-tetramethyl-1,3,2-dioxaborolane (0.39 g, 0.89 mmol), NaHCO_3 (0.23 g, 2.69 mmol), and $\text{Pd}(\text{PPh}_3)_4$ (0.051 g, 0.045 mmol) in THF (50 mL) and H_2O (5 mL) was refluxed for 12 h. After cooling the solution, H_2O (10 mL) and brine (10 mL) were added. The organic layer was separated and dried over MgSO_4 . The solvent was removed in vacuo. The pure product **8** was obtained by chromatographic work-up (eluent $\text{CH}_2\text{Cl}_2/\text{hexane}$, 1:3, $R_f=0.4$) as a yellow solid in 70% yield. M.p. 178 °C; ^1H NMR (CDCl_3): $\delta=7.65$ (t, $J=7.5$ Hz, 2H), 7.63 (d, $J=8.7$ Hz, 2H), 7.40 (d, $J=8.7$ Hz, 2H), 7.35 (t, $J=7.5$ Hz, 2H), 7.29–7.25 (m, 6H), 7.24 (s, 2H), 7.15 (d, $J=7.2$ Hz, 2H), 6.94 (s, 1H), 2.82 (t, $J=7.8$ Hz, 2H), 2.73 (d, $J=7.8$ Hz, 2H), 1.72 (br, 4H), 1.43 (s, 12H), 1.34–1.24 (m, 24H), 0.89 (t, $J=6.8$ Hz, 3H), 0.86 ppm (t, $J=6.8$ Hz, 3H); $^{13}\text{C}\{^1\text{H}\}$ NMR (CDCl_3): $\delta=155.2$, 153.7, 147.5, 147.2, 140.7, 139.0, 138.9, 136.8, 135.5, 134.5, 130.9, 130.1, 129.1, 127.1, 126.7, 123.5, 123.3, 122.6, 120.8, 120.2, 119.6, 119.0, 47.0, 31.7, 31.6, 30.5, 30.0, 29.4, 29.2, 28.9, 28.5, 28.0, 27.2, 22.7, 14.3, 14.2 ppm; MS: m/z : 783 [M^+]; elemental analysis calcd (%) for $\text{C}_{59}\text{H}_{78}\text{NS}_2$: C 82.71, H 7.33; found: C 82.10, H 7.28.

N-[4-(5-Bromo-3,6-dihexylthieno[3,2-b]thiophen-2-yl)phenyl]-N-(9,9-dimethyl-9H-fluoren-2-yl)-9,9-dimethyl-9H-fluoren-2-amine (9): *n*BuLi (0.50 mL, 1.6 M solution in hexane) was added to a solution of **8** (0.53 g, 0.67 mmol) in dry Et_2O under argon. After 3 h, bromine (0.12 g, 0.74 mmol) was added dropwise at 0 °C under argon. The mixture was washed with 5% aqueous KOH solution and dried with MgSO_4 . The solvent was evaporated. The pure product **9** was obtained in 80% yield by silica gel chromatography (eluent $\text{CH}_2\text{Cl}_2/\text{hexane}$, 1:3, $R_f=0.5$). M.p. 181 °C; ^1H NMR (CDCl_3): $\delta=7.64$ (t, $J=8.1$ Hz, 2H), 7.62 (d, $J=8.7$ Hz, 2H), 7.39 (d, $J=8.7$ Hz, 2H), 7.33 (t, $J=8.1$ Hz, 2H), 7.30–7.23 (m, 6H), 7.20 (s, 2H), 7.14 (d, $J=7.8$ Hz, 2H), 2.92 (t, $J=7.8$ Hz, 2H), 2.72 (d, $J=7.8$ Hz, 2H), 1.72 (br, 4H), 1.42 (s, 12H), 1.34–1.24 (m, 12H), 0.89 (t, $J=6.8$ Hz, 3H), 0.86 ppm (t, $J=6.8$ Hz, 3H); $^{13}\text{C}\{^1\text{H}\}$ NMR (CDCl_3): $\delta=155.2$, 153.6, 147.6, 147.1, 140.5, 139.0, 138.7, 136.8, 135.5, 134.6, 130.9,

130.0, 129.1, 128.4, 127.1, 126.7, 123.6, 123.2, 122.6, 120.8, 119.6, 119.1, 47.0, 31.7, 31.6, 30.5, 30.1, 29.5, 29.2, 28.9, 28.5, 28.0, 27.2, 22.7, 14.3, 14.2 ppm; MS: *m/z*: 863 [*M*⁺]; elemental analysis calcd (%) for C₅₄H₆₆BrNS₂: C 75.15, H 6.54; found: C 74.98, H 6.48.

***N*-(9,9-Dimethyl-9H-fluoren-2-yl)-9,9-dimethyl-*N*-[4-(3,3',6,6'-tetrahexyl-2,2'-bithieno[3,2-*b*]thiophen-5-yl)phenyl]-9H-fluoren-2-amine (10)**: Compound 10 was synthesized by a similar procedure to that described for 8, except that 9 (0.5 g, 0.58 mmol) was used in place of *N,N*-bis(9,9-dimethylfluoren-2-yl)-4-bromoaniline. Yield: 67%. M.p. 182 °C; ¹H NMR (CDCl₃): δ = 7.65 (t, *J* = 7.8 Hz, 2H), 7.63 (d, *J* = 8.2 Hz, 2H), 7.40 (d, *J* = 8.2 Hz, 2H), 7.35 (t, *J* = 7.8 Hz, 2H), 7.33–7.25 (m, 6H), 7.24 (s, 2H), 7.16 (d, *J* = 7.6 Hz, 2H), 7.00 (s, 1H), 2.82 (t, *J* = 7.8 Hz, 2H), 2.81–2.71 (m, 6H), 1.81–1.71 (m, 8H), 1.43 (s, 12H), 1.34–1.24 (m, 24H), 0.89 (t, *J* = 6.8 Hz, 3H), 0.88–0.86 (m, 6H), 0.85 ppm (t, *J* = 6.8 Hz, 3H); ¹³C NMR (CDCl₃): δ = 155.2, 153.6, 147.6, 147.2, 140.4, 139.3, 139.0, 136.8, 135.5, 135.3, 134.6, 132.3, 132.1, 132.0, 130.8, 130.1, 128.8, 128.7, 128.5, 127.1, 126.7, 125.6, 123.6, 123.3, 122.6, 120.8, 119.6, 119.0, 47.0, 31.8, 31.7, 31.6, 31.5, 30.5, 30.4, 30.0, 29.8, 29.6, 29.4, 29.3, 29.2, 29.0, 28.9, 28.7, 28.5, 28.3, 28.0, 27.8, 27.6, 27.1, 22.7, 14.3, 14.2, 14.1 ppm; MS: *m/z*: 1090 [*M*⁺]; elemental analysis calcd (%) for C₇₂H₈₃NS₂: C 79.29, H 7.67; found: C 78.98, H 7.43.

5-[4-(Bis(9,9-dimethyl-9H-fluoren-2-yl)amino)phenyl]-3,3',6,6'-tetrahexyl-2,2'-bithieno[3,2-*b*]thiophene-5'-carbaldehyde (11): Compound 11 was synthesized by a procedure similar to that described for 6, except that 10 (0.5 g, 0.58 mmol) was used in place of 4. Yield: 83%. M.p. 172 °C; ¹H NMR (CDCl₃): δ = 10.1 (s, 1H), 7.65 (t, *J* = 8.1 Hz, 2H), 7.64 (d, *J* = 8.7 Hz, 2H), 7.40 (d, *J* = 8.7 Hz, 2H), 7.33 (t, *J* = 8.1 Hz, 2H), 7.30–7.25 (m, 6H), 7.22 (s, 2H), 7.16 (d, *J* = 8.1 Hz, 2H), 3.11 (t, *J* = 7.8 Hz, 2H), 2.83 (t, *J* = 7.8 Hz, 2H), 2.71–2.68 (m, 4H), 1.81–1.71 (m, 8H), 1.43 (s, 12H), 1.34–1.24 (m, 24H), 0.88 (t, *J* = 6.7 Hz, 3H), 0.88–0.86 (m, 6H), 0.83 ppm (t, *J* = 6.7 Hz, 3H); ¹³C NMR (CDCl₃): δ = 182.6, 155.3, 153.6, 147.7, 147.1, 145.5, 145.3, 140.8, 139.3, 139.0, 138.2, 137.2, 137.0, 135.7, 134.6, 130.7, 130.1, 129.2, 128.5, 127.9, 127.1, 126.7, 123.6, 123.2, 122.6, 120.8, 119.6, 119.1, 47.0, 31.8, 31.7, 31.6, 31.4, 30.5, 30.4, 30.1, 29.9, 29.7, 29.5, 29.3, 29.2, 29.0, 28.8, 28.7, 28.5, 28.3, 28.0, 27.8, 27.6, 27.1, 22.6, 14.3, 14.2, 14.1 ppm; MS: *m/z*: 1118 [*M*⁺]; elemental analysis calcd (%) for C₇₂H₈₃NOS₂: C 78.37, H 7.48; found: C 78.18, H 7.33.

(Z)-3-[5-[(*E*)-2-(5-[4-(Bis(9,9-dimethyl-9H-fluoren-2-yl)amino)phenyl]-3,6-dihexylthieno[3,2-*b*]thiophen-2-yl)vinyl]-3,6-dihexylthieno[3,2-*b*]thiophen-2-yl]-2-cyanoacrylic acid (JK-112): A mixture of 6 (0.16 g, 0.140 mmol) and cyanoacetic acid (0.024 g, 0.28 mmol) was vacuum-dried and then dissolved in MeCN (60 mL) containing piperidine (0.012 g, 0.140 mmol). The solution was refluxed for 6 h. After cooling, the volatiles were removed in vacuo. The pure product JK-112 was obtained in 51% yield by silica gel chromatography (eluent CH₂Cl₂/MeOH, 2:1, *R*_f = 0.6). M.p. 221 °C; ¹H NMR ([D₂O]DMSO): δ = 8.20 (s, 1H), 7.77 (t, *J* = 8.1 Hz, 2H), 7.50 (d, *J* = 8.7 Hz, 2H), 7.42 (d, *J* = 8.7 Hz, 2H), 7.32 (t, *J* = 8.1 Hz, 2H), 7.30–7.25 (m, 6H), 7.24 (s, 2H), 7.21 (d, *J* = 15.6 Hz, 1H), 7.13 (d, *J* = 8.4 Hz, 2H), 7.10 (d, *J* = 15.6 Hz, 1H), 7.08 (d, *J* = 8.4 Hz, 2H), 3.19 (t, *J* = 7.8 Hz, 2H), 2.93 (t, *J* = 7.8 Hz, 2H), 2.71–2.68 (m, 4H), 1.81–1.71 (m, 8H), 1.37 (s, 12H), 1.34–1.24 (m, 24H), 0.82–0.79 ppm (m, 12H); ¹³C NMR (CDCl₃): δ = 166.1, 155.8, 154.9, 153.2, 152.1, 150.1, 147.7, 146.4, 145.5, 145.3, 140.8, 139.8, 139.0, 138.4, 137.2, 137.0, 135.7, 134.6, 133.4, 132.1, 130.7, 130.1, 129.4, 128.5, 127.8, 127.1, 126.8, 123.6, 123.4, 122.6, 120.3, 119.5, 119.1, 46.4, 31.8, 31.7, 31.6, 31.4, 30.5, 30.4, 30.1, 29.9, 29.7, 29.5, 29.3, 29.2, 29.0, 28.8, 28.7, 28.5, 28.3, 28.0, 27.8, 27.6, 27.1, 22.6, 14.3, 14.2, 14.1 ppm; MS: *m/z*: 1210 [*M*⁺]; elemental analysis calcd (%) for C₉₆H₉₈N₂O₂S₄: C 77.31, H 7.15; found: C 77.14, H 7.01.

(Z)-3-[5-[(*E*)-2-(5-[6-(Bis(9,9-dimethyl-9H-fluoren-2-yl)amino)benzo[*b*]thiophen-2-yl]-3,6-dihexylthieno[3,2-*b*]thiophen-2-yl)vinyl]-3,6-dihexylthieno[3,2-*b*]thiophen-2-yl]-2-cyanoacrylic acid (JK-113): Compound JK-113 was synthesized by a procedure similar to that described for JK-112, except that 7 (0.21 g, 0.175 mmol) was used in place of 6. Yield: 53%. M.p. 197 °C; ¹H NMR (CDCl₃): δ = 8.19 (s, 1H), 7.77 (d, *J* = 9.0 Hz, 1H), 7.69 (d, *J* = 8.1 Hz, 2H), 7.61 (t, *J* = 8.1 Hz, 2H), 7.58 (s, 1H), 7.39 (t, *J* = 8.1 Hz, 2H), 7.36 (d, *J* = 9.0 Hz, 1H), 7.32–7.28 (m, 4H), 7.25 (s, 2H), 7.22 (d, *J* = 15.6 Hz, 1H), 7.16 (d, *J* = 15.6 Hz, 1H), 7.13 (d, *J* = 8.1 Hz, 2H), 7.10 (s, 1H), 3.07 (t, *J* = 7.8 Hz, 2H), 2.96 (t, *J* = 7.8 Hz,

2H), 2.82 (t, *J* = 7.8 Hz, 4H), 1.85–1.71 (m, 8H), 1.43 (s, 12H), 1.34–1.24 (m, 24H), 0.89 (t, *J* = 6.8 Hz, 3H), 0.88–0.86 (m, 6H), 0.85 ppm (t, *J* = 6.8 Hz, 3H); ¹³C NMR (CDCl₃): δ = 166.2, 156.2, 155.6, 154.7, 148.5, 147.5, 146.5, 145.3, 143.7, 142.2, 141.1, 139.0, 138.4, 137.5, 136.5, 136.2, 134.8, 134.4, 134.1, 133.9, 133.8, 133.4, 132.8, 132.3, 131.8, 131.2, 130.8, 129.5, 128.5, 127.1, 126.7, 126.5, 126.3, 123.2, 122.7, 120.8, 119.5, 47.0, 31.8, 31.7, 31.6, 31.5, 30.5, 30.4, 30.0, 29.8, 29.6, 29.4, 29.3, 29.2, 29.0, 28.9, 28.7, 28.5, 28.3, 28.0, 27.8, 27.6, 27.1, 22.7, 14.3, 14.2, 14.1 ppm; MS: *m/z*: 1266 [*M*⁺]; elemental analysis calcd (%) for C₉₆H₉₈N₂O₂S₄: C 75.78, H 6.84; found: C 75.34, H 6.67.

(Z)-3-[5-[4-(Bis(9,9-dimethyl-9H-fluoren-2-yl)amino)phenyl]-3,3',6,6'-tetrahexyl-2,2'-bithieno[3,2-*b*]thiophen-5'-yl]-2-cyanoacrylic acid (JK-81): Compound JK-81 was synthesized by a procedure similar to that described for JK-112, except that 11 (0.04 g, 0.036 mmol) was used in place of 6. Yield: 83%. M.p. 172 °C; ¹H NMR ([D₂O]DMSO): δ = 8.20 (s, 1H), 7.77 (t, *J* = 8.1 Hz, 2H), 7.50 (d, *J* = 8.7 Hz, 2H), 7.42 (d, *J* = 8.7 Hz, 2H), 7.32 (t, *J* = 8.1 Hz, 2H), 7.30–7.25 (m, 6H), 7.24 (s, 2H), 7.13 (d, *J* = 8.4 Hz, 2H), 7.08 (d, *J* = 8.4 Hz, 2H), 3.21 (t, *J* = 7.8 Hz, 2H), 2.93 (t, *J* = 7.8 Hz, 2H), 2.71–2.68 (m, 4H), 1.81–1.71 (m, 8H), 1.37 (s, 12H), 1.34–1.24 (m, 24H), 0.82–0.79 ppm (m, 12H); ¹³C NMR (CDCl₃): δ = 166.1, 154.9, 153.2, 147.7, 146.4, 145.5, 145.3, 140.8, 139.8, 139.0, 138.4, 137.2, 137.0, 135.7, 134.6, 130.7, 130.1, 129.4, 128.5, 127.8, 127.1, 126.8, 123.6, 123.4, 122.6, 120.3, 119.5, 119.1, 46.4, 31.8, 31.7, 31.6, 31.4, 30.5, 30.4, 30.1, 29.9, 29.7, 29.5, 29.3, 29.2, 29.0, 28.8, 28.7, 28.5, 28.3, 28.0, 27.8, 27.6, 27.1, 22.6, 14.3, 14.2, 14.1 ppm; MS: *m/z*: 1184 [*M*⁺]; elemental analysis calcd (%) for C₉₆H₉₈N₂O₂S₄: C 76.98, H 7.14; found: C 76.54, H 7.03.

Device preparation (DSSC using liquid electrolyte): Photoanodes composed of nanocrystalline TiO₂ were prepared according to a previously reported procedure.^[4] A paste composed of 20 nm anatase TiO₂ particles for the transparent nanocrystalline layer was coated onto fluorine-doped tin oxide (FTO) glass plates (Nippon Sheet Glass, 4 mm thickness) pretreated with TiCl₄ (40 mm) by repetitive screen printing to obtain a thickness of 8 μm. Then, a paste for the scattering layer containing 400 nm anatase particles (CCIC, HPW-400) was deposited onto the transparent nanocrystalline layer. The resulting layer had a thickness of around 5 μm. The TiO₂ electrodes were gradually sintered according to a programmed sequence: at 325 °C for 5 min, at 375 °C for 5 min, at 450 °C for 15 min, and finally at 500 °C for 15 min. The TiO₂ electrodes were further treated with TiCl₄ at below 70 °C for 30 min and then sintered once more at 500 °C for 30 min. Thereafter, they were immersed in dye solutions (0.3 mM in THF) at room temperature for 16–18 h. The dye-adsorbed TiO₂ electrode and a thermally platinized counter electrode were assembled into a sealed sandwich-type cell with a gap of a hot-melt ionomer film (Surlyn, thickness 25 μm, DuPont). Two different electrolyte solutions were used for the redox couple: electrolyte 1: 0.6 M 1,2-dimethyl-3-propylimidazolium iodide (DMPImI), 0.05 M I₂, 0.1 M LiI, and 0.5 M *tert*-butylpyridine in acetonitrile; electrolyte 2: 0.2 M iodine, 0.5 M NMBI, 0.1 M GuNCs in PMII/EMINCS (13:7). An anti-reflection and UV cut-off film (λ < 380 nm, ARKTOP, Asahi Glass) was attached to the DSSC surface. To reduce scattered light from the edge of the dyed TiO₂ layer of the glass electrodes, a light-shading mask was placed on the DSSCs so that their active area was fixed at 0.159 cm².

Device preparation (ssDSSC): Details of the construction process for the solid-state solar cell have been described previously.^[5] The cell consisted of an FTO glass substrate (15 Ω cm⁻², Pilkington) onto which a compact layer of approximately 100 nm TiO₂ had been deposited by spray pyrolysis. A nanoporous layer (film thickness ~2.1 μm) of 20 nm diameter TiO₂^[6] was coated by screen printing. After the TiO₂ layer had been gradually sintered according to a programmed sequence (at 100 °C for 10 min, at 150 °C for 5 min, at 325 °C for 10 min, at 450 °C for 10 min, and finally at 500 °C for 30 min), the film was treated with 40 mM aqueous TiCl₄ solution for 30 min at 70 °C. The TiO₂ electrodes were immersed in the dye solutions (unless mentioned otherwise, 3 mM in THF) at room temperature in the dark for 3 h. After rinsing the electrodes, a hole-conducting matrix (see below) was applied by spin-coating (72 μL per 2.5 × 3 cm² area, spinning for 30 s at 2000 rpm). Fabrication of the device was

completed by evaporating a 100 nm gold electrode on the top surface. The active area of each ssDSSC was about 0.2 cm².

Preparation of the hole-conducting matrix: 2,2',7,7'-Tetrakis(*N,N*-dimethoxyphenylamine)-9,9'-spiro-bifluorene (spiro-OMeTAD) (72 mg) was dissolved in C₆H₆Cl (420 μL) at 60 °C. Distilled 4-*tert*-butylpyridine (TBP) (7 μL) and 15 μL of a solution of Li[(CF₃SO₂)₂N] (17 mg) in MeCN (100 μL) were then added to the solution.

Device measurements: For photovoltaic measurements of the DSSCs, the irradiation source was a 450 W xenon lamp (Osram XBO 450, USA), the power of which as an AM 1.5 solar simulator was calibrated using a Tempax 113 solar filter (Schott). The output power of an AM 1.5 solar simulator was calibrated using a reference Si photodiode equipped with a colour-matched IR cut-off filter (KG-3, Schott) to reduce the mismatch in the region 350–750 nm between the simulated light and AM 1.5. The measured IPCE values were plotted as a function of excitation wavelength by using the incident light from a 300 W xenon lamp (ILC Technology, USA), which was focused through a Gemini-180 double monochromator (Jobin Yvon Ltd.).

Impedance measurements: AC impedance measurements were made under illumination (1 sun) and in dark conditions using an impedance analyzer (1260A, Solartron, UK).

Cyclic voltammetry: Cyclic voltammetry was carried out with a BAS 100B apparatus (Bioanalytical Systems, Inc.). A three-electrode system was used, which consisted of a gold disk, a working electrode, and a platinum wire electrode. The redox potentials of the dyes on TiO₂ were measured in CH₃CN with 0.1 M (nC₄H₉)₄N-PF₆ as supporting electrolyte at a scan rate of 50 mV s⁻¹ (vs. Fc/Fc⁺).

Acknowledgements

This work was supported by the Korea Science and Engineering Foundation (KOSEF) through the National Research Laboratory Program funded by the Ministry of Science and Technology (No. R0A-2005-000-10034-0), the WCU (Ministry of Education and Science) Program (No. R31-2008-000-10035-0), and the ERC (Korean Government (MEST)) Program (No. R11-2009-088-02001-0).

- [1] N. Robertson, *Angew. Chem.* **2006**, *118*, 2398; *Angew. Chem. Int. Ed.* **2006**, *45*, 2338.
 [2] a) B. O'Regan, M. Grätzel, *Nature* **1991**, *353*, 737; b) M. K. Nazeeruddin, A. Kay, I. Rodicio, R. Humphry-Baker, E. Muller, P. Liska, N. Vlachopoulos, M. Grätzel, *J. Am. Chem. Soc.* **1993**, *115*, 6382; c) A. J. Frank, N. Kopidakis, J. van de Lagemaat, *Coord. Chem. Rev.* **2004**, *248*, 1165.
 [3] a) Y. Chiba, A. Islam, Y. Watanabe, R. Komiya, N. Koide, L. Y. Han, *Jpn. J. Appl. Phys. Part 2* **2006**, *45*, L638; b) M. K. Nazeeruddin, F. De Angelis, S. Fantacci, A. Selloni, G. Viscardi, P. Liska, S. Ito, T. Bessho, M. Grätzel, *J. Am. Chem. Soc.* **2005**, *127*, 16835; c) Y. Cao, Y. Bai, Q. Yu, Y. Cheng, S. Liu, D. Shi, F. Gao, P. Wang, *J. Phys. Chem. C* **2009**, *113*, 6290; d) F. Gao, Y. Wang, D. Shi, J. Zhang, M. Wang, X. Jing, R. Humphry-Baker, P. Wang, S. M. Zakeeruddin, M. Grätzel, *J. Am. Chem. Soc.* **2008**, *130*, 10720.

- [4] a) G. Zhang, H. Bala, Y. Cheng, D. Shi, X. Lv, Q. Yu, P. Wang, *Chem. Commun.* **2009**, 2198; b) S. Ito, H. Miura, S. Uchida, M. Takata, K. Sumioka, P. Liska, P. Comte, P. Péchy, M. Grätzel, *Chem. Commun.* **2008**, 5194; c) H. Choi, C. Baik, S. O. Kang, J. Ko, M. S. Kang, M. K. Nazeeruddin, M. Grätzel, *Angew. Chem.* **2008**, *120*, 333; *Angew. Chem. Int. Ed.* **2008**, *47*, 327; d) M. Xu, S. Wenger, H. Bala, D. Shi, R. Li, T. Zhou, S. M. Zakeeruddin, M. Grätzel, P. Wang, *J. Phys. Chem. C* **2009**, *113*, 2966; e) S. Kim, D. Kim, H. Choi, M. S. Kang, K. Song, S. O. Kang, J. Ko, *Chem. Commun.* **2008**, 4951; f) Z. S. Wang, N. Koumura, Y. Cui, M. Takahashi, H. Sekiguchi, A. Mori, T. Kubo, A. Furube, K. Hara, *Chem. Mater.* **2008**, *20*, 3993; g) T. Horiuchi, H. Miura, K. Sumioka, S. Uchida, *J. Am. Chem. Soc.* **2004**, *126*, 12218; h) S. Kim, J. K. Lee, S. O. Kang, J. Ko, J. H. Yum, S. Fantacci, F. De Angelis, D. Di Censo, M. K. Nazeeruddin, M. Grätzel, *J. Am. Chem. Soc.* **2006**, *128*, 16701.
 [5] D. Liu, R. W. Fessenden, G. L. Hug, P. V. Kamat, *J. Phys. Chem. B* **1997**, *101*, 2583.
 [6] a) K. Hara, Y. Dan-oh, C. Kasada, Y. Ohga, A. Shinpo, S. Suga, K. Sayama, H. Arakawa, *Langmuir* **2004**, *20*, 4205; b) R. Chen, X. Yang, H. Tian, L. Sun, *J. Photochem. Photobiol. A* **2007**, *189*, 295; c) J. H. Yum, D. P. Hagberg, S. J. Moon, K. M. Karlsson, T. Marinado, L. Sun, A. Hagfeldt, M. K. Nazeeruddin, M. Grätzel, *Angew. Chem.* **2009**, *121*, 1604; *Angew. Chem. Int. Ed.* **2009**, *48*, 1576.
 [7] a) M. Wang, M. Xu, D. Shi, R. Li, F. Gao, G. Zhang, Z. Yi, R. Humphry-Baker, P. Wang, S. M. Zakeeruddin, M. Grätzel, *Adv. Mater.* **2008**, *20*, 4460; b) G. Zhang, Y. Bai, R. Li, D. Shi, S. Wenger, S. M. Zakeeruddin, M. Grätzel, P. Wang, *Energy Environ. Sci.* **2009**, *2*, 92.
 [8] a) H. Choi, J. K. Lee, K. H. Song, K. Song, S. O. Kang, J. Ko, *Tetrahedron* **2007**, *63*, 1553; b) S. Kim, H. Choi, C. Baik, K. Song, S. O. Kang, J. Ko, *Tetrahedron* **2007**, *63*, 11436.
 [9] D. Shi, N. Pootrakulshote, R. Li, J. Guo, Y. Wang, S. M. Zakeeruddin, M. Grätzel, P. Wang, *J. Phys. Chem. C* **2008**, *112*, 17046.
 [10] Q. Wang, J. E. Moser, M. Grätzel, *J. Phys. Chem. B* **2005**, *109*, 14945.
 [11] S. Kim, J. K. Lee, S. O. Kang, J. Ko, J. H. Yum, S. Fantacci, F. De Angelis, D. Di Censo, M. K. Nazeeruddin, M. Grätzel, *J. Am. Chem. Soc.* **2006**, *128*, 16701.
 [12] H. Choi, J. K. Lee, K. Song, S. O. Kang, J. Ko, *Tetrahedron* **2007**, *63*, 3115.
 [13] M. He, F. Zhang, *J. Org. Chem.* **2007**, *72*, 442.
 [14] M. K. Nazeeruddin, P. Péchy, T. Renouard, S. M. Zakeeruddin, R. Humphry-Baker, P. Comte, P. Liska, C. Le, E. Costa, V. Shklover, L. Spiccia, G. B. Deacon, C. A. Bignozzi, M. Grätzel, *J. Am. Chem. Soc.* **2001**, *123*, 1613.
 [15] a) L. Schmidt-Mende, U. Bach, R. Humphry-Baker, T. Horiuchi, H. Miura, S. Ito, S. Uchida, M. Grätzel, *Adv. Mater.* **2005**, *17*, 813; b) H. J. Snaith, M. Grätzel, *Appl. Phys. Lett.* **2006**, *89*, 262114/1; c) H. J. Snaith, L. Schmidt-Mende, M. Grätzel, M. Chiesa, *Phys. Rev. B* **2006**, *74*, 045306/1; d) J.-H. Yum, P. Chen, M. Grätzel, M. K. Nazeeruddin, *ChemSusChem* **2008**, *1*, 699.
 [16] S. Ito, T. N. Murakami, P. Comte, P. Liska, C. Grätzel, M. K. Nazeeruddin, M. Grätzel, *Thin Solid Films* **2008**, *516*, 4613.

Received: August 6, 2009

Published online: December 8, 2009

5.2.2 Communications

Teocoli F., Raabe I. , Yum J. , Nazeeruddin M. K. , Ko J. , Grätzel M., Ghedini M.
Oral presentation: "**Solid state dye-sensitized solar cells**". I Meeting of the
"B.Telesio" Doctoral School Encounter with Foreign Partners – Ph.D.'S Research
Activities, Grand Hotel San Michele - Cetraro - CS, **21 – 22 September 2009**.

Raabe I., Yum J., Nazeeruddin M. K., Teocoli F., Ko J., Grätzel M., Poster
Presentation: " **Molecular engineering of organic sensitizers for solar cell
applications**". Fall Meeting of the Swiss Chemical Society, Ecole Polytechnique
Fédérale de Lausanne, Friday, **4 September 2009**.

Internship:

Doctorate's Thesis internship at Laboratory of Photonics and Interfaces(LPI) -
Institute of Chemical Science and Engineering - Faculty of Basic Science - Ecole
Polytechnique Federale de Lausanne, CH-1015 Lausanne Switzerland, about **Solid
State Dye Sensitized Solar Cells** under supervision of Professors Michael Grätzel
and Md. Khaja Nazeeruddin - mdkhaja.nazeeruddin@epfl.ch - 01 March – 31
August 2009.

Chapter 6

Conclusion

Hybrid mesoporous materials have been prepared., Chapter 2.

These investigations were made in order to test a synthesis protocol which can be beneficial for the preparation of new emitting materials for optical applications.

In particular, in order to evaluate the possible effects induced by the different electrostatic interactions that could take place between the templating agent and the neutral [Ir] compound, mesostructured materials containing a cationic or a non-ionic surfactant have been prepared.

The adopted approach allowed for the incorporation of the [Ir] guest into a mesostructured matrix host by a co-organizing process involving the two selected surfactants: the cationic CTAB and the non-ionic P123.

The XRD and nitrogen sorption measurements of the obtained materials evidenced the preferential inclusion of the iridium(III) chromophore into the hydrophobic channels of the mesostructured without any substantial changes to the typical hexagonal symmetry, with respect to both the blank samples and analogous synthesized materials.

Nevertheless, XRD measurements showed that when the cationic CTAB is used as a structure directing agent, the [Ir] complex is preferentially placed in between the hydrophobic tails of the surfactants. In contrast, the non-ionic P123 directs the chromophore mainly into the centre of micelle cores.

Moreover, the resultant hybrid materials exhibit the characteristic emission of the [Ir] complex with a high luminescence quantum yield originating from the effective good dispersion of the chromophore within the mesostructured matrices. Further investigations are currently under way in order to extend the described approach to the mesoporous film as host matrix for the same Iridium chromophore.

In Chapter 3 we investigated a solid state dye-sensitized solar cell realized with two highly efficient organic sensitizers with a planar thienothiophene–vinylene–thienothiophene linker. Solar-cell devices based on the sensitizers JK-113 and JK-

112 in conjunction with a solid electrolyte, Spiro-OMeTAD solution gave high conversion efficiencies, 4.33% and 4.31% respectively, high extinction coefficients and good IPCE, up to 59%.

A JK-113-based solar cell fabricated using the solid electrolyte showed a poor stability under light soaking at 60°C for 1000 h, this parameter will be subject to rigorous investigations. We believe that the development of highly efficient organic dyes comparable to ruthenium dyes is possible through meticulous molecular engineering of organic dyes, and work directed towards this aim is now in progress.

In Chapter 4 we show a Ruthenium-LEEC prototype as *testing ground* for a serial production with more interesting luminescent materials, like the Ir(III) complex showing high quantum efficiency and a characteristic liquid-crystalline phase.

More in general we introduce also the possibility to produce lighting devices with a new concept of electrode, over and above the traditional ITO; in particular the mesoporous Titania matrix production connects our experience in mesoporous electrode fabrication with the potential applications of Titania in electronic devices, and so on.

Just some additional remarks about the lighting devices:

A LEEC is cheaper to produce due to its simpler architecture respect to OLED and is much more robust. LEECs are easy to fabricate, but currently, the main problem similar to OLEDs is the short lifetime of the cells. These range from only a few minutes of luminescence to a few thousand hours. At present, research is focused on increasing the range of colors and improving the lifetimes with the aim of applying LEECs in, for example, computer screens, TVs, room lighting²⁹², etc.

Perspectives

Mesoporous materials with their good surface and structural properties and versatility can be synthesized in different morphologies (thin films, fibers, membranes, etc.) and represent excellent host matrices, highly functional and with great potentials for advanced applications, including separation technology (chromatography), catalysis, nanoelectronics, sensors and optoelectronics.

Suitably functionalized hybrid mesoporous silicates are promising candidates for optical applications, including lasers, light filters, sensors, solar cells, pigments, optical data storage, photocatalysis, and frequency doubling devices²⁹³. Huo *et al.* demonstrated that mesoporous silica fibers can function as optical waveguides²⁹⁴. Modification of the mesoporous fibers by incorporation of appropriate dyes would allow tuning of the optical properties. A number of dyes have been integrated in mesoporous solids.

The interest in mesoporous thin films originates from the appreciation of their technological potential as OLEDs, for example, in fact these applications require the ordered material in the form of thin film.

Mesoporous thin film can be used as emitting layers in which coordination complexes with luminescent properties for OLED preparation are grafted. OLEDs are electro-optics devices based on luminescent organic compounds with significant advantages with respect to the more common and widely used inorganic based devices (LEDs)²⁹⁵: low production cost, easy color modulation obtained through suitable structural modifications, possibility of multicolor emission, high resolution, easy processing, possibility of making wide and flexible panel displays²⁹⁶.

The rapid progress in efficiency and performance demonstrated by lighting technology over the last decade has caused many companies to consider OLEDs, first and then LEECs, as potential solid-state light sources for lighting applications. In terms of application potential, OLEDs nicely complement inorganic LEDs, and LEECs show a simpler architecture.

In particular, LEECs are more bright and intense, in contrast to OLEDs that show a diffuse light and so are naturally suited to large area general-lighting and signage applications²⁹⁷.

Another attractive feature of LEECs technology for the lighting industry is the potential for extremely low cost “newspaper-like” processing, since all the LEEC parts can be produced from liquid solutions.

LEEC devices promise to replace conventional light sources, such as incandescent and fluorescent lamps, and to become an important application in display technology. With the success of flat screen displays at the end of the 20th century,

the demand for even thinner, foldable, more power efficient models, and displays showing a larger colour gamut, has risen. LEEC devices, promise to deliver these demands as they can be “printed” onto substrates in contrast to the inorganic devices like LEDs, and with a theoretically lower cost than LCDs or plasma displays.

In conclusion, we introduce briefly in chapter 4 and in the conclusion the importance of a nanostructured electrode in organic light-emitting devices.

A mesoporous nanocrystalline metal-oxide film, i.e. TiO_2 , as an electron-injecting cathode is a very promising candidate for both light-emitting devices and solid state dye-sensitized solar cells.

In fact, whether for photovoltaic or light-emitting operating mode, critical factors for cell efficiency are:

- Incomplete wetting of the dye covered TiO_2 surface.
- Incomplete filling of the pores with the hole-transport material.

Therefore, in general, the device performance can be enhanced by using a nanostructured charge-injection electrode compared to more conventional planar electrodes.

Acknowledgments

I want begin with *Professor Mauro Ghedini*, because he allowed me to work in his group and I enjoyed the benefit of his advice and experience. It has been a great pleasure for me to work in such an interdisciplinary project.

Thanks to Dr.ssa Anna Maria Talarico for her profound knowledge of the principles of photochemistry. This thesis was improved by her for which I am thankful.

On the engineeristic point of view, I am extremely thankful to Dr.ssa Daniela Aiello for her always optimistic and enthusiastic approach to the work.

I am also grateful to Dr.ssa Iolinda Aiello for her support and suggestions.

I would like to thank the rich female group of the Cemif.Cal laboratory, first of all, Dr.ssa Elisabeta Szerb, for her luminescent materials, Iridium and Ruthenium, without them nothing would be realized, Dr.ssa Paola Liguori, Dr.ssa Alessia Aprea, Dr.ssa Loredana Ricciardi, future-doc Valentina Mannella , Prof Daniela Pucci and Prof. Alessandra Crispini. On the masculine-side I am grateful to Dr. Sante Pirillo, Dr. Yogesh Yadav and Dr. Massimo La Deda.

A particular thanks to Dr. Nicolas Godbert for having proposed me the interesting work on LEECs.

A special thanks to Professor Micheal Graetzel, Professor Md.Khaja Nazeeruddin and Dr.ssa Ines Raabe for the splendid collaboration we shared. It has been a great pleasure to learn further steps in the solid state dye-sensitized solar cells.

I have to name several people from Physics Department, without them I would not be here, Dr.ssa Federica Ciuchi and Dr. Alfredo Mazzulla, Prof. Carlo Versace and Dr.ssa Leticia Jimenez.

For the helping and suggestions during the LEECs work, I want to thanks Dr. Alfredo Pane.

I want also to remember that a lot of my LEECs work was developed in a CLEAN ROOM at Physics Department.

All my work about mesostructured films would be very complicated without the help of Dr. Michele Giocondo and Dr. Massimo Sposato.

I am deeply indebted to *my lovely and beloved family, Alessia, Marisa, Leonardo e Zeno, THANK YOU!*

References

- 1 Cynthia G. Zoski, Handbook of Electrochemistry, *Elsevier Science*, **2007**
- 2 Ogawa, M.; Kuroda, K. *Chem. Rev.* **1995**, 95, 399.
- 3 Fundamentals of Photochemistry, Rohatgi-Mukherjee K.K. - *New Age*, **1978**
- 4 Hybrid Materials. Synthesis, Characterization, and Applications. Edited by Guido Kickelbick, Copyright © **2007** Wiley-VCH Verlag GmbH & Co. KGaA, Weinheim
- 5 Yoshiki Chujo, Organic/Inorganic Nano-Hybrid Materials, KONA No.25 (**2007**)
- 6 B. Arkles, *Mater. Res. Bull.*, 2001, 26, 5, 402.
- 7 Clément Sanchez, Beatriz Julia, Philippe Belleville and Michael Popall, *J. Mater. Chem.*, **2005**, 15, 3559–3592
- 8 “Hybrid Organic-Inorganic Materials. In Search of Synergic Activity.” Pedro Gomez-Romero, *Adv.Mater.* **2001**, 13(3), 163-174.
- 9 Organic/Inorganic Hybrid Materials based on Conducting Organic Polymers as Electrodes for Energy Storage Devices – PhD Thesis - Ana Karina Cuentas Gallegos, Laboratorio de Química del Estado Sólido, Instituto de Ciencia de Materiales, October **2003**
- 10 S. Inagaki, S. Guan; Y. Fukushima, T. Oshuna, O. Terasaki, *J. Chem. Soc. Chem. Commun.*, **1999**, 121, 9611;
- 11 S. Inagaki, S. Guan, T. Oshuna, O. Terasaki, *Nature*, **2002**, 416, 303;
- 12 Daniela Aiello, *Preparation and characterization of mesostructured functional materials with different morphologies*, PhD Thesis- University of Calabria. Feb **2009**
- 13 Fabrication of functional nano-objects via self-assembly of nanostructured hybrid materials. T. Pietsch, N.Gindy, B. Mahltig, A.Fahmi. *Journal of Polymer Science Part B: Polymer Physics* Volume. **2010**, 48, Issue 14.
- 14 J.-P. Boilot, F. Chaput, T. Gacoin, L. Malier, M. Canva, A. Brun, Y. Le´vy and J.-P. Galaup, *C. R. Acad. Sci.*, **1996**, 322, 27. 43
- 15 M. Faloss, M. Canva, P. Georges, A. Brun, F. Chaput and J.-P. Boilot, *Appl. Opt.*, **1997**, 36, 6760.
- 16 B. Schaudel, C. Guermeur, C. Sanchez, K. Nakatani and J. Delaire, *J. Mater. Chem.*, **1997**, 7, 61.
- 17 B. Lebeau, C. Sanchez, S. Brasselet and J. Zyss, *Chem. Mater.*, **1997**, 9, 1012.

-
- 18 C. Rottman, G. Grader, Y. DeHazan, S. Melchior and D. Avnir, *J. Am. Chem. Soc.*, 1999, 121, 8533.
- 19 T. Dantas de Moraes, F. Chaput, J.-P. Boilot, K. Lahlil, B. Darracq and Y. Levy, *Adv. Mater.*, 1999, 11, 107.
- 20 (a) D. Levy, J. M. S. Pena, C. J. Serna, J. M. Oton and L. Esquivias, *J. Non-Cryst. Solids*, **1992**, 147–148, 646;
- (b) J. M. Oton, J. M. S. Pena, A. Serrano and D. Levy, *Appl. Phys. Lett.*, **1995**, 66, 929;
- (c) D. Levy and N. Armenise, in *Materials and devices for photonic circuits*, ed. L. G. Hubert-Pfalzgraf and S. I. Najafi, SPIE, Washington, **1999**, vol. 3803, p. 12;
- (d) D. Levy, *Mol. Cryst. Liq. Cryst.*, **2000**, 354, 747.
- 21 F.L. Carter, R.E. Siatkowski, H. Wohltjen (Eds.), *Molecular Electronic Devices*, North Holland, Amsterdam, **1988**.
- 22 D. Mendenhall, A. Greensberg, J. Liebman (Eds.), *Mesomolecules: from Molecules to Materials*, Chapman and Hall, London, **1995**
- 23 V. Ramamurthy (Ed.), *Photochemistry in Organized and Constrained Media*, VCH, New York, **1991**.
- 24 K. Kalyanasundaram, *Photochemistry in Microheterogeneous Systems*, Academic Press, New York, **1985**.
- 25 (a) T. Matsuura, M. Anpo (Eds.), *Photochemistry on Solid Surfaces (Studies on Surface Science and Catalysis)*, vol. 47, Elsevier, Amsterdam, **1989**.
- (b) K. Honda (Ed.), *Photochemical Processes in Organized Molecular Systems*, Elsevier, Amsterdam, **1991**.
- 26 V. Ramamurthy, R.G. Weiss, G. Hammond, *Adv. Photochem.* 18 (**1993**) 67.
- 27 J.K. Thomas, *Chem. Rev.* 93 (**1993**) 301.
- 28 V. Balzani, F. Scandola, *Supramolecular Photochemistry*, Horwood, Chichester, UK, **1991**.
- 29 V. Balzani, L. De Cola, (Eds.), *Supramolecular Chemistry*, Kluwer, Dordrecht, **1992**.
- 30 J-M. Lehn, *Supramolecular Chemistry*, VCH, Weinheim, **1995**.
- 31 F. Vögtle, *Supramolecular Chemistry*, Wiley, Chichester, UK, **1993**.
- 32 *Photofunctional Transition Metal Complexes*, Editors: Michael P. Mingos and Vivian W.W. Yam With contributions by M. Grätzel and M. K. Nazeeruddin - Springer-Verlag Berlin Heidelberg **2007**

-
- 33 C.J.Brinker,C.W.Scherer,Sol-Gel Science:the Physics and Chemistry of Sol-Gel Processing,Academic Press,San Diego,CA,1990.
- 34 L.C. Klein, Sol-Gel Optics-Processing and Applications, Kluwer, Boston, MA, 1994.
- 35 H.D. Gesser, P.C. Goswami, Chem. Rev. 89 (1989) 765.
- 36 L.C. Klein (Ed.), Sol-Gel Technology for Thin Films, Fibres, Preforms, Electronics and Speciality Shapes, Noyes, New Jersey, **1988**.
- 37 (a) E. Matijevic, Mater. Res. Soc. Bull. 4 (**1989**) 18.
- (b) E. Matijevic, Mater. Res. Soc. Bull. 5 (**1990**) 16.
- 38 (a) E. Matijevic, Chem. Mater. 5 (**1993**) 412.
- (b) E. Matijevic, Chem. Mater. 15 (**1985**) 485.
- 39 a) E. Matijevic, Langmuir 2 (**1986**) 12.
- (b) E. Matijevic, Langmuir 10 (**1994**) 8.
- 40 Applications of functionalized transition metal complexes in photonic and optoelectronic devices, K. Kalyanasundaram, M. Graätzel, Coordination Chemistry Reviews, 77 (**1998**) 347–414
- 41 Recent Developments in Solid-State Dye-Sensitized Solar Cells. Jun-Ho Yum, Peter Chen, Michael Graetzel, and Mohammad K. Nazeeruddin, ChemSusChem **2008**, 1, 699 – 707.
- 42 N. S. Lewis, Science, **2007**, 315, 798.
- 43 Pietruszko, S.M., Opto-Electronics Review, **2004**. 12: p. 7
- 44 Becquerel, E. C.R. Acad.. Sci. Paris **1839**, 9, 561.
- 45 Moser, J. Monatsh. Chemie **1887**, 8, 373.
- 46 O'Regan, B.; Gratzel, M., Nature, **1991**. 353: p. 737.
- 47 G. Zhang, H. Bala, Y. Cheng, D. Shi, X. Lv, Q. Yu, P. Wang, Chem. Commun. **2009**, 2198;
- 48 S. Ito, H. Miura, S. Uchida, M. Takata, K. Sumioka, P. Liska, P. Comte, P. Péchy, M. Grätzel, Chem. Commun. **2008**, 5194;
- 49 H. Choi, C. Baik, S. O. Kang, J. Ko, M. –S. Kang, M. K. Nazeeruddin, M. Grätzel, Angew. Chem. Int. Ed. 2008, 47, 327; Angew, Chem, **2007**, 120, 333;

-
- 50 M. Xu, S. Wenger, H. Bala, D. Shi, R. Li, T. Zhou, S. M. Zakeeruddin, M. Grätzel, P. Wang, *J. Phys. Chem. C* **2009**, 113, 2966;
- 51 S. Kim, D. Kim, H. Choi, M. –S. Kang, K. Song, S. O. Kang, J. Ko, *Chem. Commun.* **2008**, 4951;
- 52 Z. –S. Wang, N. Koumura, Y. Cui, M. Takahashi, H. Sekiguchi, A. Mori, T. Kubo, A. Furube, K. Hara, *Chem. Mater.* **2008**, 20, 3993;
- 53 T. Horiuchi, H. Miura, K. Sumioka, S. Uchida, *J. Am. Chem. Soc.* **2004**, 126, 12218;
- 54 S. Kim, J. K. Lee, S. O. Kang, J. Ko, J. –H. Yum, S. Fantacci, F. De Angelis, D. Di Censo, M. K. Nazeeruddin, M. Grätzel, *J. Am. Chem. Soc.* **2006**, 128, 16701.
- 55 Recent Developments in Solid-State Dye-Sensitized Solar Cells, Jun-Ho Yum, Peter Chen, Michael Graetzel, and Mohammad K. Nazeeruddin, *ChemSusChem* **2008**, 1, 699 – 707
- 56 Principles and Applications of Dye Sensitized Nanocrystalline Solar Cells (DSC), M. Gaetzel and A. J. McEvoy *Asian J. Energy Environ.*, Vol. 5, Issue 3, (2004), pp. 197-210.
- 57 Verner K. Thorsmølle, Bernard Wengera, Joël Teuscher, Christophe Bauer, and Jacques-E. Moser, *CHIMIA* **2007**, 61, No. 10
- 58 Marco-A. De Paoli and Wilson A. Gazotti, *J. Braz. Chem. Soc.*, Vol. 13, No. 4, 410-424, **2002**.
- 59 Smart, L.; Moore, E.; *Solid State Chemistry, An Introduction*, 2nd ed., Chapman & Hall: London, **1995**.
- 60 Li, S. S.; *Semiconductor Physical Electronics*, Plenum Press: New York, **1993**.
- 61 Bube, R. H.; *Electrons in Solids*, 2nd ed., Academic Press: New York, **1988**.
- 62 Gooch, C. H.; *Injection Electroluminescent Devices*, John Wiley & Sons: London, **1973**.
- 63 Hall, R. N.; Fenner, G. E.; Kingsley, J. D.; Soltys, T. J.; Carlson, R. O.; *Phys. Rev. Lett.* **1962**, 9, 366.
- 64 Nathan, M. I.; Dumke, W. P.; Burns, G.; Dill, F. H.; Lasher, G.; *Appl. Phys. Lett.* **1962**, 1, 62.
- 65 Quist, T. M.; Rediker, R. H.; Keyes, R. J.; Krag, W. E.; Lax, B.; McWhorter, A. L.; Zeigler, H. J.; *Appl. Phys. Lett.* **1962**, 1, 91.

-
- 66 Baldo, M. A.; O'Brien, D. F.; You, Y.; Shoustikov, A.; Sibley, S.; Thompson, M. E.; Forrest, S. R. *Nature (London)* **1998**, 395, 151-154.
- 67 Hartmut Rudmann, Satoru Shimada, and Michael F. Rubner, *J. AM. CHEM. SOC.* **2002**, 124, 4918-4921
- 68 J.deMello, *Nature Materials*, 2007, vol.6, 796.
- 69 Q.B.Pei,G-Yui,C.Zhang,Y.Yang,A.J.Heeger, *Science*, **1995**, 269, 1086-1088.
- 70 Q.B.Pei, G-Yui, C.Zhang, Y.Yang, A.J.Heeger, *J.Am.Chem.Soc.*,**1996**, 118, 3922-3929.
- 71 G. Yu, A. J. Heeger, *Synth. Met.* **1997**, 85, 1183.
- 72 Y. Yang, Q. Pei, *J. Appl. Phys.* **1997**, 81, 3294.
- 73 A. J. Heeger, M. Pauchard-Strebel, M. Vehse, L. Edman, D. Moses, *US Patent* 6 828 583, **2004**.
- 74 For reviews on LECs, see: a) Q. Pei, Y. Yang, G. Yu, Y. Cao, A. J. Heeger, *Synth. Met.* **1997**, 85, 1229.
- b) D. Neher, J. Grüner, V. Cimrova, W. Schmidt, R. Rulkens, U. Lauter, *Polym. Adv. Technol.* **1998**, 9, 461.
- c) U. Mitscheke, P. Bäuerle, *J. Mater. Chem.* **2000**, 10, 1471.
- d) N. R. Armstrong, R. M. Wightman, E. M. Gross, *Annu. Rev. Phys.Chem.* **2001**, 52, 391.
- e) M. Buda, in *Electrogenerated Chemiluminescence* (Ed: A. J. Bard), Marcel Dekker, New York **2004**, Ch. 10.
- f) L. Edman, *Electrochim. Acta* **2005**, 50, 3878.
- g) D. Dini, *Chem. Mater.* **2005**, 17, 1933.
- 75 Henk J. Bolink, Eugenio Coronado, Rubén D. Costa, Enrique Ortí , Michele Sessolo, Stefan Graber, Kevin Doyle, Markus Neuburger, Catherine E. Housecroft, Edwin C. Constable, *Adv. Mater.* **2008**, 20, 3910–3913
- 76 Hai-Ching Su, et al., *J. AM. CHEM. SOC.* **2008**, 130, 3413-3419
- 77 Cao, Y.; Yu, G.; Heeger, A. J.; Yang, C. Y.; *Appl. Phys. Lett.* **1996**, 68, 3218.
- 78 Zhao, M. Lu, and G. J. Millar, *Industrial & Engineering Chemistry Research*, 35, 2075-2090, **1996**

-
- 79 Beck, J. S., and J. C. Vartuli, *Current Opinion in Solid State & Materials Science*, 1, 76-87, **1996**.
- 80 Attard, G. S., J. C. Glyde, and C. G. Goltner, *Nature*, 378, 366-368, **1995**.
- 81 Robert Mokaya and William Jon, *Chem. Commun.*, **1997** 2185
- 82 Brinker, C. J.; Lu, Y.; Sellinger, A.; Fan, H. *Adv. Mater.* **1999**, 11, 579.
- 83 E.L. Crepaldi, G.J.deA.A. Soler-Illia, D. Grosso, et al, *J. Am. Chem. Soc.* 2003, 125, 9770-9786,
- 84 Schüth, F., *Angewandte Chemie-International Edition*, 42, 3604-3622, **2003**.
- 85 Sing, K. S. W., et al., *Pure and Applied Chemistry*, 57, 603-619, **1985**.
- 86 C. Wang, et al., *J. Mater. Chem.*, 2008, **18**, 683 - 690
- 8777 Brinker-Scherer, *Sol-gel science: The physics and chemistry of sol-gel processing*. Academic Press: San Diego, **1990**.
- 88 J. S. Beck; J. C. Vartuli; et al, 1992, *American Chemical Society* **114**, 10834–10843. [doi:10.1021/ja00053a020](https://doi.org/10.1021/ja00053a020).
- 89 Brian Trewyn, et al. (**2007**). *Accounts of Chemical Research* (40): 846–853.
- 90 C.T. Kresge, M.E. Leonowicz, W.J. Roth, J.C. Vartuli, J.S. Beck, *Nature* 359 (1992) 710.
- 91 Dongyuan Zhao, et al. (**1998**). *Science* (279): 548.
- 92 S.H. Tolbert, T.E. Schaffer, J. Feng, P.K. Hansma, G.D. Stucky, *Chem. Mater.* 9 (1997) 1962.
- 93 Hua Dong, PhD Thesis: “Organic-Inorganic Hybrid Mesoporous Silica Materials and Their Application as Host Matrix for Protein Molecules”, Drexel University, March **2002**
- 94 (a) Klein, L. C. Ed. *Sol-Gel Technology*, Noyes Publications: Park Ridge, NJ, **1988**.
- (b) Hench, L. L.; West, J. K. *Chem. Rev.* (Washington D.C.) **1990**, 90, 33.
- (c) Livage, J.; Henry, M.; Sanchez, C. *Prog. Solid State. Chem.* **1988**, 18, 259.
- 95 Trewyn, B G; Nieweg, J A; Zhao, Y; Lin, V S.-Y. (**2007**). *Chemical Engineering Journal* (137)
- 96 P. Selvam, S.K. Bhatia, C.G. Sonwane, *Ind. Eng. Chem. Res.* 40 (**2001**) 3237.
- 97 K. Cassiers et al., *Chem. Mater.* 14 (**2002**) 2317.

-
- 98 Y. Bennadja, P. Beaunier, D. Margolese, A. Davidson, *Micropor. Mesopor. Mater.* 44–45 (2001) 147.
- 99 M. Kruk, M. Jaroniec, C.H. Ko, R. Ryoo, *Chem. Mater.* 12 (2000) 1961.
- 100 C. J. Brinker, Y. Lu, A. Sellinger and H. Fan, *Adv. Mater.*, 1999, 11, 579.
- 101 H. Y. Fan, Y. F. Lu, A. Stump, S. T. Reed, T. Baer, R. Schunk, L. V. Perez, G. P. Lopez and C. J. Brinker, *Nature*, 2000, 405, 56.
- 102 D. Y. Zhao, P. D. Yang, N. Melosh, Y. L. Feng, B. F. Chmelka and G. Stucky, *Adv. Mater.*, 1998, 10, 1380.
- 103 Y. Lu, R. Ganguli, C. A. Drewien, M. T. Anderson, C. J. Brinker, W. Gong, Y. Guo, H. Soyez, B. Dunn, M. H. Huang and J. I. Zink, *Nature*, 1997, 389, 364.
- 104 D. A. Doshi, N. K. Huesing, M. C. Lu, H. Y. Fan, Y. F. Lu, P. K. Simmons, B. G. Potter, A. J. Hurd and C. J. Brinker, *Science*, 2000, 290, 107.
- 105 D. Grosso, A. R. Balkenende, P.-A. Albouy, M. Lavergne, L. Mazerolles and F. Babonneau, *J. Mater. Chem.*, 2000, 10, 2085.
- 106 A. Sellinger, P. M. Weiss, N. Anh, Y. Lu, R. A. Assink, W. Gong and C. J. Brinker, *Nature*, 1998, 394, 256.
- 107 VanSlyke SA, Tang CW (1987) *Appl Phys Lett* 51:913
- 108 Kim JS, Ho PKH, Greenham NC, Friend RH (2000) *J Appl Phys* 88:1073
- 109 Baldo MA, Adachi C, Forrest SR (2000) *Phys Rev B* 62:10967
- 110 Photofunctional Transition Metal Complexes, Editors: Michael P.Mingos and Vivian W.W. Yam With contributions by M. Grätzel and M. K. Nazeeruddin - Springer-Verlag Berlin Heidelberg 2007
- 111 Adachi C, Baldo MA, Thompson ME, Forrest SR (2001) *J Appl Phys* 90:5048
- 112 Baldo MA, Lamansky S, Burrows PE, Thompson ME, Forrest SR (1999) *Appl Phys Lett* 75:4
- 113 Ikai M, Tokito S, Sakamoto Y, Suzuki T, Taga Y (2001) *Appl Phys Lett* 79:156
- 114 Nazeeruddin MK, Humphry-Baker R (2003) *J Am Chem Soc* 125:8790
- 115 Slinker JD, Gorodetsky AA, Lowry MS, Wang J, Parker S, Rohl R, Bernhard S, Malliaras GG (2004) *J Am Chem Soc* 126:2763
- 116 Slinker J, Bernards D, Houston PL, Abruna HD, Bernhard S, Malliaras GG (2003) *Chem Commun*, p 2392
- 117 Rudmann H, Shimida S, Rubner MF (2002) *J Am Chem Soc* 124:4918

-
- 118 Bernhard S, Barron JA, Houston PL, Abruna HD, Ruglovksy JL, Gao X, Malliaras GG (2002) *J Am Chem Soc* 124:13624
- 119 Wegh RT, Meijer EJ, Plummer EA, De Cola L, Brunner K, van Dijken A, Hofstraat JW (2004) *Proc SPIE* 5519:48
- 120 Handy ES, Pal AJ, Rubner MF (1999) *J Am Chem Soc* 121:3525
- 121 Gao FG, Bard AJ (2000) *J Am Chem Soc* 122:7426
- 122 Tmayo AB, Garon S, Sajoto T, Djurovich PI, Tsyba IM, Bau R, Thompson ME (2005) *Inorg Chem* 44:8723
- 123 Strickler SJ, Berg RA (1962) *J Chem Phys* 37:814
- 124 Kober EM, Caspar JV, Lumpkin RS, Meyer TJ (1986) *J Phys Chem* 90:3722
- 125 93. Juris A, Balzani V, Barigelletti F, Campagna S, Belser P, von Zelewsky A (1988) *Coord Chem Rev* 84:85
- 126 Nonoyama M (1975) *Bull Chem Soc Jpn* 47:767
- 127 Hay PJ (2002) *J Phys Chem B* 106:1634
- 128 King KA, Watts RJ (1987) *J Am Chem Soc* 109:1589
- 129 Dedeian K, Djurovich PI, Garces FO, Carlson C, Watts RJ (1991) *Inorg Chem* 30:1685
- 130 Sprouse S, King KA, Spellane PJ, Watts RJ (1984) *J Am Chem Soc* 6647
- 131 Ohsawa Y, Sprouse S, King KA, DeArmond MK, Hanck KW, Watts RJ (1987) *J Phys Chem* 91:1047
- 132 Garces FO, King KA, Watts RJ (1988) *Inorg Chem* 27:3464
- 133 Yang C-H, Li S-W, Chi Y, Cheng Y-M, Yeh Y-S, Chou P-T, Lee G-H (2005) *Inorg Chem* 44:7770
- 134 Lowry MS, Goldsmith JI, Slinker JD, Rohl R, Pascal RA, Malliaras GG, Bernhard S (2005) *Chem Mater* 17:5712
- 135 Baldo MA, Adachi C, Forrest SR (2000) *Phys Rev B* 62:10967
- 136 Y. Kawamura, J. Brooks, J. J. Brown, H. Sasabe and C. Adachi, *Phys. Rev. Lett.*, **2006**, 96, 017404.
- 137 C. Rothe, et al., *Adv. Funct. Mater.* **2009**, 19, 2038 and references therein.
- 138 C.-H. Chang, C.-C. Chen, C.-C. Wua, C.-H. Yang and Y. Chi, *Org. Electron.*, **2009**, 10, 1364.

-
- 139 C.-H. Yang, S.-H. Yang and C.-S. Hsu, *Nanotechnology*, **2009**, 20, 315601 and reference therein.
- 140 F. Hoffmann, M. Cornelius, J. Morell, M. Fröba, [*J. Nanosci. Nanotechn.*, **2006**, 6, 265-288](#)
- 141 H.S. Zhou and I. Honma, *Adv. Mat.*, **1999**, 11, 683.
- 142 P. Yang, et al., *Science*, **2000**, 287, 465.
- 143 B. J. Scott, G. Wirnsberger and G. D. Stucky, *Chem. Mater.*, **2001**, 13, 3140.
- 144 E. Dovgolevsky, S. Kirmayer, E. Lakin, Y. Yang, C.J. Brinker and G.L. Frey, *J. Mater. Chem.*, **2008**, 18, 423.
- 145 N. Mizoshita, Y. Goto, T. Tani and S. Inagaki, **2009**, *Adv. Mater.*, 21, 4798.
- 146 A.B. Tamayo et al., *J. Am. Chem. Soc.*, **2003**, 125, 7377.
- 147 R.I. Nooney, D. Thirunavukkarasu, Y. Chen, R. Josephs and A.E. Ostafin, *Chem. Mater.*, **2002**, **14**, 4721.
- 148 D. Zhao, Q. Huo, J. Feng, B.F. Chmelka and G.D. Stucky, *J. Am. Chem. Soc.*, **1998**, 120, 6024.
- 149 D. Grosso, F. Babonneau, P.A. Albouy, H. Amenitsch, A.R. Balkenende, A. Brunet-Bruneau, J. Rivory, *Chem. Mater.*, **2002**, 2, 931
- 150 D.A. Doshi, A. Gibaud, V. Goletto, M. Lu, H. Gerung, B. Ocko, S.M. Han, C.J. Brinker, *J. Am. Chem. Soc.*, **2003**, 125, 11646
- 151 D. Grosso, P.A. Albouy, H. Amenitsch, A.R. Balkenende, F. Babonneau, *Mater. Res. Soc. Symp. Proc.*, **2000**, 628, CC6.17.1
- 152 D. Grosso, A.R. Balkenende, P.A. Albouy, A. Ayril, H. Amenitsch, F. Babonneau, *Chem. Mater.*, **2001**, 13, 1848
- 153 J.L. Ruggles, S.A. Holt, P.A. Reynolds, J.M. White, *Langmuir*, **2000**, 16, 4613
- 154 N. Yao, A.Y. Ku, N. Nakagawa, T. Lee, D.A. Saville, I.A. Aksay, *Chem. Mater.*, **2000**, 12, 1536
- 155 G.J. de A.A. Soler-Illia, E.L. Crepaldi, D. Grosso, C. Sanchez, *Curr. Opin. Colloid Interface Sci.*, **2003**, 8, 109
- 156 F. Siperstein, K.E. Gubbins, *Mol. Simul.*, **2001**, 27, 339
- 157 D. Grosso, F. Cagnol, G.J.A.A. Soler-Illia, E.L. Crepaldi, H. Amenitsch, A. Brunet-Bruneau, A. Burgeois, C. Sanchez, *Adv. Funct. Mater.*, **2004**, 14, 309
- 158 A. Brunet-Bruneau, S. Besson, T. Gacoin, J.P. Boilot, J. Rivory, *Thin Solid Films*, **2004**, 447/448

-
- 159 Brinker CJ, Lu Y, Sellinger A, Fan H (1999) *Adv Mater* 11:579
- 160 Soler-Illia JAA, Sanchez C, Lebeau B, Patarin J (2002) *Chem Rev* 102:4093
- 161 Doshi DA, Brinker CJ et al. (2003) *J Am Chem Soc* 125(38):11646
- 162 Soler-Illia G, Innocenzi P (2006) *Chem: Europ J* 12(17):4478
- 163 S. Brunauer, P. H. Emmett and E. Teller, *J. Amer. Chem. Soc.*, **1938**, 60, 309
- 164 E.P. Barrett, L.G. Joyner and P.P. Halenda, *J. Am. Chem. Soc.*, **1951**, 73, 373.
- 165 S.J. Gregg, K.S.W. Sing, Adsorption, surface area and porosity, 2nd ed., Academic Press; New York, 1982;
- 166 F. Rouquerol, J. Rouquerol, K. Sing, *Adsorption by Powders and Porous Solids*; Academic Press; New York, **1999**
- 167 E.P. Barrett, L.G. Joyner, P.P. Halenda, *J. Am. Chem. Soc.*, **1951**, 73, 373
- 168 Daniela Aiello, *Preparation and characterization of mesostructured functional materials with different morphologies*, PhD Course in Chemical and Materials Engineering, UNICAL, **2009**
- 169 M. S. Lowry and S. Bernhard, *Chem. Eur. J.*, **2006**, 12, 7970.
- 170 L. Flamigni, A. Barbieri, C. Sabatini, B. Ventura and F. Barigelletti, *Top. Curr. Chem.*, **2007**, 281, 143.
- 171 M. K. Nazeeruddin and M. Grätzel, *Struct. Bonding*, 2007, 123, 113.
- 172 Y. You and S. Young Park, *Dalton Trans.*, **2009**, 1267.
- 173 C. Ulbricht, B. Beyer, C. Friebe, A. Winter, and U. S. Schubert, *Adv. Mater.*, **2009**, 21, 4418.
- 174 Y. Kawamura, J. Brooks, J.J. Brown, H. Sasabe and C. Adachi, *Phys. Rev. Lett.*, **2006**, 96, 017404.
- 175 Y. You and S. Y. Park, *Dalton Trans.*, **2009**, 1267.
- 176 W. Holzer, A. Penzkofer and T. Tsuboi, *Chem. Phys.*, 2005, **308**, 93.
- 177 E. B. Namdas, A. Ruseckas, I. D. W. Samuel, S. C. Lo and P. L. Burn, *J. Phys. Chem. B*, **2004**, 108, 1570.
- 178 H. Wang, Q. Liao, H. Fu, Y. Zeng, Z. Jiang, J. Maa and J. Yao, *J. Mater. Chem.*, **2009**, 19, 89.
- 179 H.S.Zhou, H.Sasabe and I. Honma, *J. Mater. Chem.*, **1998**, 8, 515 and references therein.

-
- 180 Barrett, E. P. , Joyner, L. G. and Halenda, P. P. (1951). *J. Am. Chem. Soc.* 73 , pp. 373-380.
- 181 Scott BJ, Bartl MH, Wirnsberger G, Stucky GD (2003) *J Phys Chem A* 107, 5499
- 182 Tennakone, K.; Hewaparakkrama, K. P.; Dewasurendra, M.; Jayatissa, A. H.; Weerasena, L. K. *Semicond. Sci. Technol.* 1988, 3, 382-387
- 183 Hagen, J.; Schaffrath, W.; Otschik, P.; Fink, R.; Bacher, A.; Schmidt, H.-W.; Haarer, D. *Synth. Met.* 1997, 89, 215-220.
- 184 Murakoshi, K.; Kogure, R.; Yanagida, S. *Chemistry letters* 1997, 5, 471-472.
- 185 Murakoshi, K.; Kogure, R.; Wada, Y.; Yanagida, S. *Solar Energy Materials and solar cells* 1998, 55, 113-125.
- 186 *Photofunctional Transition Metal Complexes*, Editors: Michael P.Mingos and Vivian W.W. Yam With contributions by M. Grätzel and M. K. Nazeeruddin - Springer-Verlag Berlin Heidelberg 2007
- 187 Ito S, Zakeeruddin SM, Humphry-Baker R, Liska P, Charvet R, Comte P, Nazeeruddin MK, Pechy P, Takata M, Miura H, Uchida S, Grätzel M (2006) *Adv Mater* 18:1202
- 188 Savenije, T. J.; Warman, J. M.; Goossens, A. *Chem. Phys. Lett.* 1998, 287, 148-153.
- 189 Kajihara, K.; Tanaka, K.; Hirao, K.; Soga, N. *Jpn. J. Appl. Phys.* 1997, 36, 5537-5542
- 190 Gamboa, S. A.; Nguyen-Cong, H.; Chartier, P.; Sebastian, P. J.; Calixto, M. E.; Rivera, M. A. *Sol. Energy Mater. Sol. Cells* 1998, 55, 95-104.
- 191 D Nghong D, Serpone N, Graetzel M (1984) *Helv Chim Acta* 67:1012
- 192 Gerischer H, Tributsch H (1968) *Phys Chem* 72:437
- 193 Desilvestro J, Graetzel M, Kavan L, Moser J, Augustynski J (1985) *J Am Chem Soc* 107:2988
- 194 Hagfeldt A, Grätzel M (2000) *Acc Chem Res* 33:269
- 195 O'Regan B, Grätzel M (1991) *Nature* 353:737
- 196 NazeeruddinMK, WangQ, Cevey L, AranyosV, LiskaP, FiggemeierE, KleinC, Hirata N, Koops S, Haque SA, Durrant JR, Hagfeldt A, Lever ABP, Grätzel M (2006) *Inorg Chem* 45:787
- 197 Haught AF (1984) *J Solar Energ Eng* 106:3

-
- 198 De Vos A (1992) Endoreversible thermodynamics of solar energy conversion. Oxford Science, Oxford, chap 6
- 199 Nazeeruddin MK, Zakeeruddin SM, Humphry-Baker R, Jirousek M, Liska P, Vlachopoulos N, Shklover V, Fischer CH, Grätzel M (1999) *Inorg Chem* 38:6298
- 200 Anderson S, Constable EC, Dare-Edwards MP, Goodenough JB, Hamnett A, Seddon KR, Wright RD (1979) *Nature* 280:571
- 201 Grätzel M (2001) *Nature* 414:338
- 202 Nazeeruddin MK, Grätzel M (2003) In: Ramamurthy V, Schanze KS (eds) *Molecular and supramolecular photochemistry*, vol 10. Dekker, New York, p 301
- 203 Nazeeruddin MK (2004) In: Nazeeruddin MK (ed) *Special issue: Michael Graetzel Festschrift, A tribute for his 60th birthday: Dye sensitized solar cells*. *Coord Chem Rev* 248:1161
- 204 Grätzel M (2000) In: Nalwa HS (ed) *Handbook of nanostructured materials and nanotechnology*, vol 3. Academic, New York, p 527
- 205 a) G. Zhang, H. Bala, Y. Cheng, D. Shi, X. Lv, Q. Yu, P. Wang, *Chem. Commun.* 2009, 2198;
- b) S. Ito, H. Miura, S. Uchida, M. Takata, K. Sumioka, P. Liska, P. Comte, P. P_chy, M. Graetzel, *Chem. Commun.* 2008, 5194;
- c) H. Choi, C. Baik, S. O. Kang, J. Ko, M. S. Kang, M. K. Nazeeruddin, M. Graetzel, *Angew. Chem.* 2008, 120, 333; *Angew. Chem. Int. Ed.* 2008, 47, 327;
- d) M. Xu, S. Wenger, H. Bala, D. Shi, R. Li, T. Zhou, S. M. Zakeeruddin, M. Graetzel, P. Wang, *J. Phys. Chem. C* 2009, 113, 2966;
- e) S. Kim, D. Kim, H. Choi, M. S. Kang, K. Song, S. O. Kang, J. Ko, *Chem. Commun.* 2008, 4951;
- f) Z. S. Wang, N. Koumura, Y. Cui, M. Takahashi, H. Sekiguchi, A. Mori, T. Kubo, A. Furube, K. Hara, *Chem. Mater.* 2008, 20, 3993;
- g) T. Horiuchi, H. Miura, K. Sumioka, S. Uchida, *J. Am. Chem. Soc.* 2004, 126, 12218;
- h) S. Kim, J. K. Lee, S. O. Kang, J. Ko, J. H. Yum, S. Fantacci, F. De Angelis, D. Di Censo, M. K. Nazeeruddin, M. Graetzel, *J. Am. Chem. Soc.* 2006, 128, 16701.
- 206 D. Liu, R. W. Fessenden, G. L. Hug, P. V. Kamat, *J. Phys. Chem. B* 1997, 101, 2583.
- 207 a) K. Hara, Y. Dan-oh, C. Kasada, Y. Ohga, A. Shinpo, S. Suga, K. Sayama, H. Arakawa, *Langmuir* 2004, 20, 4205;
- b) R. Chen, X. Yang, H. Tian, L. Sun, *J. Photochem. Photobiol. A* 2007, 189, 295;

c) J. H. Yum, D. P. Hagberg, S. J. Moon, K. M. Karlsson, T. Marinado, L. Sun, A. Hagfeldt, M. K. Nazeeruddin, M. Grätzel, *Angew. Chem.* 2009, 121, 1604; *Angew. Chem. Int. Ed.* 2009, 48, 1576.

208 a) M. Wang, M. Xu, D. Shi, R. Li, F. Gao, G. Zhang, Z. Yi, R. Humphry-Baker, P. Wang, S. M. Zakeeruddin, M. Grätzel, *Adv. Mater.* 2008, 20, 4460;

b) G. Zhang, Y. Bai, R. Li, D. Shi, S. Wenger, S. M. Zakeeruddin, M. Grätzel, P. Wang, *Energy Environ. Sci.* 2009, 2, 92.

209 Nazeeruddin, M.K., et al., *J. Am. Chem. Soc.*, **1993**. 115: p. 6382.

210 Nazeeruddin, M.K., et al., *Inorg. Chem.*, **1999**. 38: p. 6298.

211 Zakeeruddin, S.M., et al., *Design, synthesis, and application of amphiphilic ruthenium polypyridyl photosensitizers in solar cells based on nanocrystalline TiO₂ films*. *Langmuir*, **2002**. 18(3): p. 952-954.

212 Hyunbong Choi, Ines Raabe, Duckhyun Kim, Francesca Teocoli, Chulwoo Kim, Kihyung Song, Jun-Ho Yum, Jaeyung Ko, Md. K. Nazeeruddin, and Michael Graetzel *Chem. Eur. J.* **2010**, 16, 1193 – 1201

213 L. Schmidt-Mende, U. Bach, R. Humphry-Baker, S. Ito, S. Uchida, M. Graetzel, *Adv. Mater.* 17 (**2005**) 813.

214 Bach, U.; Lupo, D.; Comte, P.; Moser, J. E.; Weissoertel, F.; Salbeck, J.; Spreitzer, H.; Graetzel, M. *Nature* **1998**, 395, 583.

215 Krueger, J.; Plass, R.; Cevey, L.; Piccirelli, M.; Graetzel, M.; Bach, U. *Appl. Phys. Lett.* **2001**, 79, 2085.

216 U. Bach, D. Lupo, P. Comte, J. Moser, S. Haque, D. Klug, M. Graetzel, J. Durrant, *J. Am. Chem. Soc.* 121 (1999) 7445.

217 J. Krueger, U. Bach, M. Graetzel, *Adv. Mater.* 12 (2000) 447.

218 Yum, J.; Chen, P.; Graetzel, M.; Nazeeruddin, M. K. *ChemSusChem* **2008**, 1, 699.

219 U. Bach, K. de Cloedt and M. Grätzel. *Adv Mat* 2000, 12, 1060-1063.

220 Krueger, J.; Plass, R.; Graetzel, M.; Cameron, P. J.; Peter, L. M. *J. Phys. Chem. B* **2003**, 107, 7536.

221 Schmidt-Mende, L.; Grätzel, M. *Thin Solid Films* **2006**, 500, 296.

222 W.H. Howie et al. / *Solar Energy Materials & Solar Cells* 91 (**2007**) 424–426

223 Cappel et al., *J. Phys. Chem. C*, Vol. 113, No. 15, **2009**

-
- 224 Kavan, L. and M. Gratzel, *Highly Efficient Semiconducting TiO₂ Photoelectrodes Prepared by Aerosol Pyrolysis*. *Electrochimica Acta*, **1995**, 40(5): p. 643-652.
- 225 Udo Bach, **Solid-state dye-sensitized mesoporous tio₂ solar cells**, *PhD thesis n° 2187 (2000)*, Laboratory of Photonic and Interfaces (LPI) – Swiss Federal Institute of Technology (EPFL)
- 226 Nathalie ROSSIER-ITEN, **Solid state dye-sensitized solar cells new organic materials charge recombination and stability**, *PhD thesis n°3457 (2006)*, Laboratory of Photonic and Interfaces (LPI) – Swiss Federal Institute of Technology (EPFL)
- 227 C. Barbé, F. Arendse, P. Comte, et al. *J Am Ceram Soc* **1997**, 80, 31557-71.
- 228 Kay, A., *Solar cells based on dye-sensitized nanocrystalline TiO₂ electrodes*. **1994**, EPFL: Lausanne
- 229 Papageorgiou, N.;Barbe, C. and Graetzel, M., *J. Am. Ceram. Soc.*, **1997**. 80: p. 31557.
- 230 Jessica Krueger, **Interface engineering in solid-state dye-sensitised solar cells**. *PhD thesis n° 2793 (2003)*, Laboratory of Photonic and Interfaces (LPI) – Swiss Federal Institute of Technology (EPFL)
- 231 Ricaud, A., *Photopiles solaires*, ed. P.P.e.U. romandes. **1997**, Lausanne.
- 232 Nusbaumer, H., **Alternative redox systems for the dye-sensitized solar cell.**, *PhD thesis n° 2955 (2004)*, Laboratory of Photonic and Interfaces (LPI) – Swiss Federal Institute of Technology (EPFL)
- 233 Plass, R., **Nanoparticle sensitised solid-state nanocrystalline solar cell**. *PhD thesis n° 3017 (2004)*, Laboratory of Photonic and Interfaces (LPI) – Swiss Federal Institute of Technology (EPFL)
- 234 G. Zhang, Y. Bai, R. Li, D. Shi, S. Wenger, S. M. Zakeeruddin, M. Gratzel, P. Wang, *Energy Environ. Sci.* **2009**, 2, 92.
- 235 a) H. Choi, J. K. Lee, K. H. Song, K. Song, S. O. Kang, J. Ko, *Tetrahedron* **2007**, 63, 1553;
- b) S. Kim, H. Choi, C. Baik, K. Song, S. O. Kang, J. Ko, *Tetrahedron* **2007**, 63, 11436.
- 236 N. Holonyak, S. F. Bevacqua, *Appl. Phys. Lett.*, **1962**, 1, 82-83.
- 237 A. A. Bergh, P. J. Dean, *Light Emitting Diodes*, Clarendon Press, Oxford, **1976**.
- 238 A. A. Bergh, G. Craford, A. Duggal, R. Haitz, *Phys. Today*, **2001**, 54, 42-47.
- 239 C. W. Tang, S. A. VanSlyke, *Appl. Phys. Lett.*, **1987**, 51, 913-915.

-
- 240 J. H. Burroughes, D. D. C. Bradley, A. R. Brown, R. N. Marks, K. Mackay, R. H. Friend, P. L. Burns, A. B. Holmes, *Nature*, **1990**, *347*, 539-541.
- 241 Q. B. Pei, G. Yu, C. Zhang, Y. Yang, A. J. Heeger, *Science*, **1995**, *269*, 1086-1088.
- 242 J. Gao, J. Dane, *Appl. Phys. Lett.*, **2003**, *83*, 3027-3029.
- 243 J. H. Shin, A. Dzwilewski, A. Iwasiewicz, S. Xiao, A. Fransson, G. N. Anka, L. Edman, *Appl. Phys. Lett.*, **2006**, *89*, 3.
- 244 S. Graber, K. Doyle, M. Neuburger, C. E. Housecroft, E. C. Constable, R. D. Costa, E. Ortí, D. Repetto, H. J. Bolink, *J. Am. Chem. Soc.*, **2008**, *130*, 14944-14945.
- 245 J. K. Lee, D. S. Yoo, E. S. Handy, M. F. Rubner, *Appl. Phys. Lett.*, **1996**, *69*, 1686-1688.
- 246 F. G. Gao, A. J. Bard, *J. Am. Chem. Soc.*, **2000**, *122*, 7426-7427.
- 247 J. D. Slinker, J. A. DeFranco, M. J. Jaquith, W. R. Silveira, Y. W. Zhong, J. M. Moran-Mirabal, H. G. Craighead, H. D. Abruna, J. A. Marohn, G. G. Malliaras, *Nat. Mater.*, **2007**, *6*, 894-899.
- 248 Q. Pei, A. J. Heeger, *Nat. Mater.*, **2008**, *7*, 167-167.
- 249 J. Gao, J. Dane, *Appl. Phys. Lett.*, **2004**, *84*, 2778-2780.
- 250 J. D. Slinker, A. A. Gorodetsky, M. S. Lowry, J. J. Wang, S. Parker, R. Rohl, S. Bernhard, G. G. Malliaras, *J. Am. Chem. Soc.*, **2004**, *126*, 2763-2767.
- 251 R. T. Wegh, E. J. Meijer, E. A. Plummer, L. De Cola, K. Brunner, A. van Dijken, J. W. Hofstraat, in *8th Conference on Organic Light-Emitting Materials and Devices* (Eds.: Z. H. Kafafi, P. A. Lane), Spie-Int Soc Optical Engineering, Denver, CO, **2004**, pp. 48-58.
- 252 A. B. Tamayo, S. Garon, T. Sajoto, P. I. Djurovich, I. M. Tsyba, R. Bau, M. E. Thompson, *Inorg. Chem.*, **2005**, *44*, 8723-8732.
- 253 H. C. Su, C. C. Wu, F. C. Fang, K. T. Wong, *Appl. Phys. Lett.*, **2006**, *89*, 3.
- 254 G. Kalyuzhny, M. Buda, J. McNeill, P. Barbara, A. J. Bard, *J. Am. Chem. Soc.*, **2003**, *125*, 6272-6283.
- 255 L. J. Soltzberg, J. D. Slinker, S. Flores-Torres, D. A. Bernards, G. G. Malliaras, H. D. Abruna, J. S. Kim, R. H. Friend, M. D. Kaplan, V. Goldberg, *J. Am. Chem. Soc.*, **2006**, *128*, 7761-7764.
- 256 Stefan Graber, *From STM to LEECs: Syntheses and Applications of Multifunctional Bipyridine Ligands and their Iridium(III) Complexes*, PhD Thesis, Naturwissenschaftlichen Fakultät der Universität Basel, **2009**

-
- 257 N. Miura, *Electronic Engineering*, (2002), p.17
- 258 G.S. Saini and D.G.Hopper, *SPIE*, 3363, 288 (1998)
- 259 X.Duan and J.S.Yuan, *Solid State Electronics*, 44 1537 (2000)
- 260 Q.B.Pei, G.Yu, C.Zhang, Y.Yang and A.J.Heeger, *Science*,269, 1086 (1995)
- 261 G.Yu, Y.Cao, C.Zhang, Y.F.Li, J.Gao and A.J. Heeder, *Appl.Phys.Lett.*, 73, 111, 1998
- 262 H.Rudmann, S.Shimada and M.F, Rubner, *J.Am.Chem.Soc*, 124, 4918, 2002
- 263 M.A. Baldo, D.F.O'Brien, Y.You, A.Shoustikov, S.Sibley, M.E.Thompson and S.R.Forrest, *Nature*, 395, 151, 1998
- 264 A.R.Brown, D.D.C.Bradley, J.H.Burroughes, R.H.Friend, N.C.Greenham, P.L.Burn, A.B.Holmes and A.Kraft, *Appl.Phys.Lett*, 61, 2793, 1992
- 265 M.A.Baldo, d.F.O'Brien, M.E.Thompson and S.R.Forrest, *Phys.Rev.B-CondensMatter*, 60, 14422(1999)
- 266 N.E. Tokel Takvoryan, R.E. Hemingway and A.J.Bard, *J.Am.Chem.Soc*,95,6582, 1973
- 267 N.ETokel and A.J Bard, *J.Am.Chem.Soc.*, 94,2862, 1972
- 268 N.ETokel and A.J Bard, *.Chem.Phys.Lett.*,25,235, 1974
- 269 N.C.Greenham, I.D.W. Samuel, G.R.Hayes, R.T. Philips, Y.A.R.R. Kessener, S.C.Moratti,A.B.Holmes,R.H.Frield, *Chem.PhysLett*. 241, 89, 1995
- 270 K.Kalyanasundaram, *Coor.Chem.Rev*, 46, 159, 1982
- 271 J.P.Frackelr, *Modern inorganic Chemistry*, Plenum Press, New York, p165, 1994
- 272 A.W. Knight and G.M. Greenway, *Analyst*, 119, 879, 1994
- 273 W.Y.Lee, *Mikrochim Acta*, 127, 19, 1997
- 274 J.R.Sheats, H.Antoniadis, M.Hueschen, W.Leonard, J.Miller, R.Moon, D.Roitman and A.Stocking, *Science*, 273, 884, 1996
- 275 Tsai Jang-Shiang, *Evaluation of solid-state light-emitting devices based on the tris-chelated Ruthenium (II) complex*, Master Thesis in Engineering in materials science, MIT, 2003
- 276 Mihai Buda, Gregory Kalyuzhny, and Allen J. Bard *J. AM. CHEM. SOC.* 2002, 124, 6090-6098
- 277 S. A. Haque, S. Koops, N. Tokmoldin, J. R. Durrant, J. Huang, D. D. C. Bradley, E. Palomares, *Advanced Materials*, 2007 (19), 683-687

278 Elisabeta I. Szerb, Anna M. Talarico, Iolinda Aiello, Alessandra Crispini, Nicolas Godbert, Daniela Pucci, Teresa Pugliese, Mauro Ghedini, European Journal of Inorganic Chemistry, Volume 2010, Issue 21, pages 3270–3277, July 2010

279 W. Fahlman and W. R. Salaneck, Surface Science, 500, 904 (2002).

280 C. J. Barbe, F. Arendse, P. Comte, M. Jirousek, F. Lenzmann, V. Shklover, M. Gratzel, J. Am. Ceram. Soc. 1997, 80, 3157.

281 A. A. Gorodetsky, S. Parker, J. D. Slinker, D. A. Bernards, M. H. Wong, G. G. Malliaras, S. Flores-Torres and H. D. Abrun˜a,

Appl. Phys. Lett., 2004, 84, 807–809.

282(a) Lee, J.-K.; Yoo, D. S.; Handy, E. S.; Rubner, M. F. *Appl. Phys. Lett.* **1996**, 69, 1686.

(b) Maness, K. M.; Terrill, R. H.; Meyer, T. J.; Murray, R. W.; Wightman, R. M. *J. Am. Chem. Soc.* **1996**, 118, 10609.

(c) Lee, J.-K.; Yoo, D.; Rubner, M. F. *Chem. Mater.* **1997**, 9, 1710.

(d) Yoo, D.; Wu, A.; Lee, J.; Rubner, M. F. *Synth. Met.* **1997**, 85, 1425.

(e) Maness, K. M.; Masui, H.; Wightman, R. M.; Murray, R. W. *J. Am. Chem. Soc.* **1997**, 119, 3987.

(f) Handy, E. S.; Abbas, E. D.; Pal, A. J.; Rubner, M. F. *Proc. SPIE-Int. Soc. Opt. Eng.* **1998**, 3476, 62.

(g) Elliot, C. M.; Pichot, F.; Bloom, C. J.; Rider, L. S. *J. Am. Chem. Soc.* **1998**, 120, 6781.

(h) Wu, A.; Lee, J.; Rubner, M. F. *Thin Solid Films* **1998**, 327-329, 663

(i) Lyons, H.; Abbas, E. D.; Lee, J.-K.; Rubner, M. F. *J. Am. Chem. Soc.* **1998**, 120, 12100.

(j) Handy, E. S.; Pal, A. J.; Rubner, M. F. *J. Am. Chem. Soc.* **1999**, 121, 3525.

(k) Wu, A.; Yoo, D.; Lee, J.-K.; Rubner, M. F. *J. Am. Chem. Soc.* **1999**, 121, 4883.

(l) Collinson, M. M.; Taussig, J.; Martin, S. A. *Chem. Mater.* **1999**, 11, 2594.

(m) Collinson, M. M.; Martin, S. A. *Chem. Commun.* **1999**, 899-900, 899.

(n) Ng, W. Y.; Gong, X.; Chan, W. K. *Chem. Mater.* **1999**, 11, 1165.

(o) Chan, W. K.; Ng, P. K.; Gong, X.; Hou, S. *J. Mater. Chem.* **1999**, 9, 2103.

(p) Rudmann, H.; Kaplan, L.; Sevian, H.; Rubner, M. F. *Polym. Mater. Sci. Eng.* **2000**, 83, 235.

-
- (q) Gao, F. G.; Bard, A. J. *J. Am. Chem. Soc.* **2000**, *122*, 7426.
- (r) Rudmann, H.; Rubner, M. F. *J. Appl. Phys.* **2001**, *90*, 4338.
- (s) Rudmann, H.; Shimada, S.; Rubner, M. F. *J. Am. Chem. Soc.* **2002**, *124*, 4918.
- (t) Buda, M.; Kalyuzhny, G.; Bard, A. J. *J. Am. Chem. Soc.* **2002**, *124*, 6090.
- (u) Bernhard, S.; Gao, X.; Abrunã, H. D.; Malliaras, G. G. *Adv. Mater.* **2002**, *14*, 433
- 283 McCord, P.; Bard, A. J. *J. Electroanal. Chem.* **1991**, *318*, 91.
- 284 Stefan Bernhard, Jason A. Barron, Paul L. Houston, Hector D. Abruna, Jennifer L. Ruglovksy, Xicun Gao, and George G. Malliaras, *J. AM. CHEM. SOC.* **2002**, *124*, 13624-13628
- 285 S. T. Parker, J. D. Slinker, M. S. Lowry, M. P. Cox, S. Bernhard, G. G. Malliaras, *Chem. Mat.*, **2005**, *17*, 3187-3190.
- 286 E. S. Handy, A. J. Pal, M. F. Rubner, *J. Am. Chem. Soc.*, **1999**, *121*, 3525-3528.
- 287 F. G. Gao and A. J. Bard, *J. Am. Chem. Soc.*, 2000, *122*, 7426–7427.
- 288 H. Rudmann, S. Shimada and M. F. Rubner, *J. Am. Chem. Soc.*, **2002**, *124*, 4918–4921.
- 289 Gregory Kalyuzhny, Mihai Buda, Jason McNeill, Paul Barbara, and Allen J. Bard, *J. AM. CHEM. SOC.* **2003**, *125*, 6272-6283
- 290 Jason D. Slinker, Jonathan Rivnay, Joshua S. Moskowitz, Jeffrey B. Parker, Stefan Bernhard, Hector D. Abrun and George G. Malliaras, *J. Mater. Chem.*, **2007**, *17*, 2976–298
- 291 Costa et al., *Chem. Mater.*, Vol. 22, No. 4, **2010**
- 292 *High efficiency and low-cost lighting devices*, Z. Palmieri, L. Bevilacqua, C. Grillo and C. Palermo, Edited by LaGrange, Copyright ©, Austin, Texas 78758 (**2006**)
- 293 C. M. Bambrough, R. C. T. Slade, R. T. Williams, *J. Mater. Chem.*, **1998**, *8*, 569;
- 294 Q. Huo, D. Zhao, J. Feng, K. Weston, S. K. Buratto, G. D. Stucky, S. Schacht, F. Schüth, *Adv. Mater.*, **1997**, *9*, 974;
- 295 P.E. Burrows, Z. Shen, V. Bulovic, D.M. McCarty, S.R. Forrest, J.A. Cronin, M.E.Thompson, *J.Appl.Phys.*, **1996**, *79*, 7991;
- 296 W. Stampor, J. Kalinowski, G. Marconi, P. Di Marco, V. Fattori and G. Giro, *Chem.Phys.Lett.*, **1998**, *183*, 373;